INFORMATION TO USERS

This manuscript has been reproduced from the microfilm master. UMI films the text directly from the original or copy submitted. Thus, some thesis and dissertation copies are in typewriter face, while others may be from any type of computer printer.

The quality of this reproduction is dependent upon the quality of the copy submitted. Broken or indistinct print, colored or poor quality illustrations and photographs, print bleedthrough, substandard margins, and improper alignment can adversely affect reproduction.

In the unlikely event that the author did not send UMI a complete manuscript and there are missing pages, these will be noted. Also, if unauthorized copyright material had to be removed, a note will indicate the deletion.

Oversize materials (e.g., maps, drawings, charts) are reproduced by sectioning the original, beginning at the upper left-hand corner and continuing from left to right in equal sections with small overlaps. Each original is also photographed in one exposure and is included in reduced form at the back of the book.

Photographs included in the original manuscript have been reproduced xerographically in this copy. Higher quality 6" x 9" black and white photographic prints are available for any photographs or illustrations appearing in this copy for an additional charge. Contact UMI directly to order.

UMI

A Bell & Howell Information Company
300 North Zeeb Road, Ann Arbor MI 48106-1346 USA
313/761-4700 800/521-0600

ORGAN VOLUME ESTIMATION FROM MAGNETIC SENSOR BASED 3D ULTRASOUND DATA: APPLICATION IN GASTRIC EMPTYING

by

Jing-Ming Jong

A dissertation submitted in partial fulfillment of the requirements for the degree of

Doctor of Philosophy

University of Washington

1997

Approved by Chi-Hou Chan
Chairperson of Supervisory Committee

Program Authorized
to Offer Degree Department of Electrical Engineering

Date Mar 19, 1997

Doctoral Dissertation

In presenting this dissertation in partial fulfillment of the requirements for the Doctoral degree at the University of Washington, I agree that the Library shall make its copies freely available for inspection. I further agree that extensive copying of this dissertation is allowable only for scholarly purposes, consistent with "fair use" as prescribed in the U.S. Copyright Law. Requests for copying or reproduction of this dissertation may be referred to University Microfilms, 1490 Eisenhower Place, P.O. Box 975, Ann Arbor, MI 48106, to whom the author has granted "the right to reproduce and sell (a) copies of the manuscript in microform and/or (b) printed copies of the manuscript made from microform."

Signature 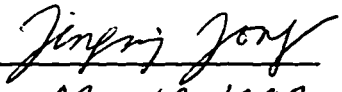

Date Mar 19, 1997

University of Washington

Abstract

ORGAN VOLUME ESTIMATION FROM MAGNETIC SENSOR BASED 3D ULTRASOUND DATA: APPLICATION IN GASTRIC EMPTYING

by Jing-Ming Jong

Chairperson of the Supervisory Committee: Professor Chi H. Chan
Department of Electrical Engineering

The study of gastric emptying requires measuring the change of stomach volume with time after a meal. A series of cross-sectional images of the stomach were acquired with conventional ultrasound imaging. The position and orientation of each image in 3D space was registered by using a magnetic sensor which was attached on the ultrasound scanhead. The borders of the stomach on the images were outlined to identify a set of contours representing the surface of the stomach. The contours often intersect one another because of the curvature of the abdomen surface, the deep position of the stomach inside the abdomen, and the tilting of ultrasound scanhead.

Two algorithms were developed for computing the volume of stomach from intersected contours. The first algorithm built a wireframe by sorting the connections between contours with vector dot-product of the connections and the central long axis of the stomach. The second algorithm deformed a pre-built wireframe to approximate the stomach of interest based on least square criterion. Both algorithms used Green and Gauss's theorem to compute the stomach volume, which is equivalent to dividing the whole volume into tetrahedra with respect to a spatial point and summing their signed volumes.

The accuracy of the methods was evaluated by scanning an *in vitro* porcine stomach filled with different volumes. Thereafter, fourteen male volunteers were studied at various time point before and after ingestion of a 500-ml broth. The mean absolute difference between

the estimated volumes of the porcine stomach and the true volumes in water displacement was 0.7% ± 0.4% (SD) with the dot-product sorting algorithm. Both methods were applied to the gastric emptying data. The average stomach volume after ingestion was expressed as (462.23ml) - (11.97ml) x (minutes after ingestion), r=0.986, SEE=22.65 ml, with half emptying time of 21.9 ± 4.5 minutes. The mean absolute difference between the two algorithms is 4.1% ± 2.8% (SD) . The deformation algorithm performs slower and less accurately than the dot-product sorting algorithm, however, it has the potential of handling more irregular shaped organs. Both algorithms are also applicable to compute the volumes of other organs scanned with freehand 3D ultrasound.

TABLE OF CONTENTS

LIST OF FIGURES

ACKNOWLEDGMENTS

I would like to express my sincerest appreciation to Dr. Paul Detmer for introducing me into the world of 3D ultrasound and being an excellent mentor. I am grateful for his help, guidance, and support throughout the course of this research. My deep gratitude also goes to my advisor, Professor Chi H. Chan, for his guidance in numerical analysis, and his interest and support in this research.

I would also like to thank Professors Kirk Beach and Roy Martin for sharing their ideas with me in many discussions. Their comments and suggestions regarding this dissertation greatly improved its readability. Special thanks also go to Professor D. Eugene Strandness, Jr. for his direction and encouragement. I also wish to thank Professor Mani Soma for serving on my supervisory committee and many constructive comments.

This research was a collaboration with Dr. Odd H. Gilja from Norway. I appreciate his leadership in medical application. Also, all the ultrasound scanning and manual outlining were performed by him. I would like to thank Xian-Ning Li and Daniel Leotta for all of their timely help in data acquisition and magnetic sensor calibration.

I also wish to thank both current and former colleagues in the University of Washington: Hyung-Sik Choi, Xian-Ning Li, Jihong Kim, Xinyu Wang, Tom Alexander, and Kil-Su Eo. My discussions with these colleagues were extremely beneficial toward the pursuit of this degree.

This work was supported by NIH grants HL41464 and R43RR07741, NSF grant ECS-9158040, and a grant from the University of Washington Royalty Research Fund. I would like to thank these institutions for their assistance and support in conducting this research.

Finally, I would like to dedicate this dissertation to my wife Miin-Herng, my children Peter and Emily, and to my parents in recognition of their love, faith, and inspiration which have given me the strength to persevere throughout this endeavor.

Chapter 1
Introduction

1.1 Significance of Stomach Volume Computation

The measurement of the change of stomach volume with time after a meal (gastric emptying) has many research and clinical applications. It has been used to investigate the physiology of the stomach in normal subjects [1, 2]. Many drugs in clinical practice delay gastric emptying, thus induce symptoms of bloating, belching, nausea, and even vomiting. Gastric emptying measurements can provide an index to these side effects. Stomach surgery usually produces side effects associated with abnormalities of gastric emptying, such as dumping, diarrhea, and gastric retention. Emptying measurements have been used to compare newer, more selective procedures with older, established operations. Furthermore, sequential emptying measurements during the first year after gastric surgery have been useful to evaluate the progress of an individual patient [3]. Various kinds of dyspepsia (indigestion) have uncertain pathogenesis, yet strong correlation with delayed gastric emptying. Emptying measurements may help the diagnosis of these symptoms [4, 5]. In addition to studying gastric emptying, ultrasound imaging of the fetal stomach has been used for the diagnosis of congenital duodenal obstruction in utero [6]. It was found that the fetal stomach with duodenal obstruction becomes extremely enlarged with advancing gestation, although the general shape is about the same as normal fetal stomach.

1.2 Anatomy of Stomach

The stomach is a pouchlike organ which hangs under the diaphragm in the upper left portion of the abdominal cavity. It is partially surrounded by the ribs and lies to the left of the liver. The length of the stomach is about 25-30 cm, and the capacity is typically about one liter but can be more. The stomach is an approximately J-shaped organ, but some individuals may have a more enlongated stomach, like a fishhook, and some may have a shorter stomach, like a steer horn. Also, depending on the position of the body and the degree of filling, the form and size of the stomach may vary considerably [7, 8].

Beginning with the innermost tissues, the stomach wall consists of four distinct layers: mucous membrane (mucosa), submucosa, muscular layer, and serous layer. The mucosa is characterized by many broad folds and numerous tubular gastric glands. The

glands secret gastric juice to digest food. Alkaline mucus is also secreted to form a protective coating to prevent the stomach from digesting itself. The mucosa of the stomach is not well adapted to absorb digestive products. Only small quantities of water, glucose, and alcohol may be absorbed. The submucosa contains loose connective tissue as well as blood vessels, lymphatic vessels, and nerves. The vessels nourish the surrounding tissues and carry away absorbed materials. The muscular layer is responsible for the movements of the stomach. There are two major layers of muscle: an inner circular layer and an outer longitudinal layer. When the fiber of the circular layer contracts, the diameter of the local stomach decreases; when the fiber of the longitudinal layer contracts, the stomach is shortened. Some parts of the stomach have another inner layer of oblique fibers. By coordinating the contraction of these layers of muscle, the stomach produces mixing action and emptying action (peristaltic waves). The mixing action disperses food with gastric juice and helps to break food down into small particles; the emptying action pushes the mixed content toward the duodenum, the first part of small intestine. The serous layer secrets fluid to keep the stomach outer surface moist, so that the stomach can slide freely against the other organs [7].

The upper part of the stomach is usually called the proximal stomach or fundus, and the lower part is called the distal stomach or antrum. The stomach, especially the proximal part, can dilate to accommodate the incoming food from the esophagus with little increase in intragastric pressure. The secretion of gastric juice actually starts on sight or smell of food prior to food ingestion, and the incoming food further stimulates secretion. Following a meal, mixing and emptying actions are produced by the aforementioned gastric contractions which occur about three times per minute [7, 9].

The rate at which the stomach empties can depend on many factors [8]:
1. Tonus of the stomach. Classified by motor and secretory activities of every individual, there are four principal functional types of stomach: hypertonic, orthotonic, hypotonic, and atonic (from the fastest to the slowest emptying).
2. Character of the food. Starch empties rapidly, protein empties at intermediate rate, and fat empties slowly.
3. Consistency of the food. Liquids empty rapidly, semisolids empty at intermediate rate, and solids empty slowly.
4. Hunger. Hunger accelerates emptying.

5. Exercise. Mild exercise accelerates emptying, and extreme exercise retards emptying.
6. Body position. The emptying is slower in the supine position than in the standing or sitting position.
7. Emotion. Aggressive emotions (hostility, resentment) accelerate emptying, and depressive emotions (sorrow, fear) retard emptying.
8. Pain. Severe or sustained pain in any part of the body retards emptying.

1.3 Previous Work on Gastric Emptying

The earliest methods of measuring gastric emptying required nasogastric intubation. Hunt, et al. pioneered a serial meal test in 1951 [1], in which normal volunteers ingested an identical liquid meal every day for several consecutive days, and all the gastric contents were aspirated via a nasogastric tube after a different time period on each day, so that the emptying rate could be determined. George invented a dye dilution and sampling method in 1968 [10] which adds, mixes, and samples colored dye in the stomach at 10-minute intervals, and the gastric volume was computed from the dye concentration in the samples. Without entirely pumping out the gastric contents at each sampling, this technique needs only one intubation for each study. However, both methods require nasogastric intubation which is considered as a stressful procedure that influences the normal gastric activity [11, 12].

In clinical practice, barium X-ray is routinely used to examine the digestive tract, including the stomach, for the presence of ulcers, tumors, strictures, and other abnormalities [13]. The barium mixture (chalky liquid) coats and fills in the hollows of the digestive tract after being drunk. Because X-rays do not pass through the barium mixture, an X-ray picture reveals the silhouette of the shape of these organs. Although the image quality is superior to other imaging modalities, such as nuclear imaging and ultrasound, barium X-ray was found to be unsuitable for measuring gastric emptying, because barium may separate from the test meal and leave the stomach at a different rate [14].

In current practice, nuclear imaging is considered the gold standard for measuring gastric emptying. Radioisotopes are added in the test meal, so the silhouette of the stomach can be recorded by a gamma camera. Both solid and liquid food can be studied, so the test meal simulates normal daily meals better and there is little

interference with normal gastric activity. However, this technique subjects the patient to ionizing radiation. Furthermore, subtlety is required in handling the error introduced by the scattering of radiation. Because the recorded image is a three-dimensional (3D) to two-dimensional (2D) projection, the small intestine occasionally overlaps with the stomach in the image and the emptying will appear delayed [3].

Ultrasound imaging utilizes high frequency sound waves to observe internal organs. Usually, both the transmitter and receiver transducers are built in the same scanning probe, and the echo of the sound waves are detected to form a 2D image in real time. It is a very popular imaging modality because it offers cost-effective cross-sectional images in real time, and it is non-invasive and free from ionizing radiation. However, because bone and air interfere with the penetration of high frequency sound waves, the proximal stomach usually has been considered inappropriate for ultrasound imaging due to its location behind the ribs and the possible presence of an air pocket in the top portion of the stomach. Thus, most gastric emptying research using ultrasound had been limited to the distal stomach portion [4, 15-18], which is valid only if the volume of the meal is less than 200 - 300 ml (Volumes exceeding the antral capacity will extend into the proximal stomach) [19]. Recently, Dr. Odd Gilja, et al. developed a new sonographic method (test meal, scanning protocol, etc.) which makes it possible to consistently monitor the area of a standard sagittal section in the proximal stomach [20]. This dissertation has evolved from a joint research with Dr. Gilja, and the sonographic method was adapted to acquire multiple sagittal sections of both the proximal and distal stomach for computing the total stomach volume.

1.4 Why 3D Ultrasound?

Anatomic structures are spatially three dimensional; therefore, volume computation performed using conventional 2D ultrasound imaging has been based on sampling the length, width, and depth of the structure, and assuming a regular geometric model, such as ellipsoid [21, 22]. While this approach is attractive because of its simplicity, it may introduce significant errors or large variations in computing the volume, especially with more irregular shaped organs. Previous studies on bladder volume measurements have demonstrated errors from 15% to 95% using 2D ultrasound [23]. The stomach's shape is more elongated and irregular, which makes it more difficult to estimate the volume based on geometric assumptions. In previous gastric emptying studies based on 2D

ultrasound, the area of a standard cross-section in the antrum was used to represent the volume [4, 16, 19]. This expedient method is not only subject to large errors and variations, but it is also valid only if the volume of the meal is less than 200 - 300 ml, as mentioned in the previous section.

Three-dimensional ultrasound does not rely on any particular standard cross-sectional image and geometric assumptions. Usually, the whole anatomic structure of interest is sampled, and the surface or solid of the structure is reconstructed. Several research groups independently reported that the volumes or ejection fractions of cardiac ventricles based on 3D surface reconstruction had approximately half the variability of 2D ultrasound [24-26]. Another recent report demonstrated that the bladder volumes based on 3D solid reconstruction had a mean absolute error of $4.3\% \pm 3.7\%$ versus $27.5\% \pm 17.8\%$ for the 2D ultrasound [27]. Gilja, et al. also reported high accuracy on measuring the stomach volume *in vitro* [28], however, they only measured the volume of gastric antrum *in vivo* [29]. The proximal stomach was not scanned because of the limited acoustic window in their motor driven 3D scanhead. The method employed in this doctoral study is based on a magnetic position and orientation sensor. This magnetic sensor based 3D ultrasound system allows freehand scanning, thus there is less limitation on the acoustic windows, and the whole stomach can be scanned. (Different 3D ultrasound systems are reviewed in Section 2.2.)

Besides quantitative measurement, 3D ultrasound may also improve data acquisition and visualization. Two-dimensional ultrasound imaging is a real-time modality, and the images are usually interpreted while the patient is on the examination bed. The images become very difficult to interpret afterwards, because the spatial relationship among images is no longer available. In contrast, 3D ultrasound imaging preserves the spatial relationship, so the data sets can be explored and analyzed after completed the examination. The display and manipulation of 3D data in geometric viewing eliminates the mental effort of synthesizing the anatomy based on memorized 2D images. Various types of 3D data visualization methods, such as wireframe, surface rendering, volume rendering, and slicing [30-33] can be utilized.

1.5 Overview of Problems and Solutions

In our magnetic sensor based 3D ultrasound system, a small sensor (6 mm x 6 mm x 9 mm) is attached on the scanhead for detecting the position and orientation of each acquired image. Because of the receiver's small size, the scanhead can be held as usual and operated with high flexibility. However, as with other freehand 3D ultrasound systems [34], the acquired images may intersect one another, and the anatomic structure becomes difficult to reconstruct. Figure 1.1 depicts a freehand scan of the proximal and distal stomach from an anterior view. The distal stomach was scanned stepwise from left to the right to acquire short-axis cross-sections. Because ultrasound waves cannot penetrate bone, the proximal stomach was scanned by positioning the scanhead under the ribs, tilting cranially to image the most superior part of the stomach, and moving stepwise from left to the right to acquire longitudinal cross-sections. Despite our attempt to acquire parallel cross-sections, the sections often intersected one another, especially in the distal stomach. Figure 1.2 depicts this phenomenon with a transverse section of the abdomen. The scanhead was moved stepwise from left to the right along the abdomen surface, and total 10 images were acquired sequentially. Images 4 and 5 intersected each other, and images 6, 7, and 8 were out of sequence. Apparently, the curvature of the abdomen surface, the deep position of the stomach inside the abdomen, and the tilting of scanhead all contributed to the intersection of images.

The intersection of each image plane with the stomach can be viewed as a contour. An example of a 3D view of the stomach in contours is shown in Figure 1.3(a). The main topic of this dissertation is to investigate the methods of computing the total volume of the stomach outlined by these types of contours. Because the contours may intersect one another or be acquired out of sequence, a volume computation method must take this into account and not simply calculate the total volume by summing the volumes between consecutive contours in acquisition order.

Two new approaches for computing the stomach volume are reported in this dissertation. The first method is to construct a wireframe from the contours as shown in Figure 1.3(b) with the volume enclosed by the wireframe computed as the total stomach volume. The second method is to deform a pre-built wireframe to match the stomach of interest with the volume of the stomach being that enclosed by the deformed wireframe. The details of these two methods are described in Chapter 4 and 5, respectively.

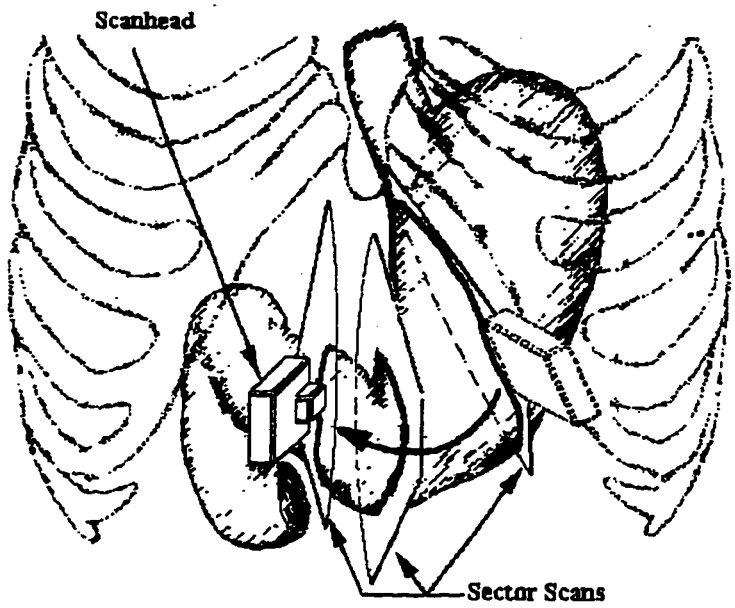

(a)

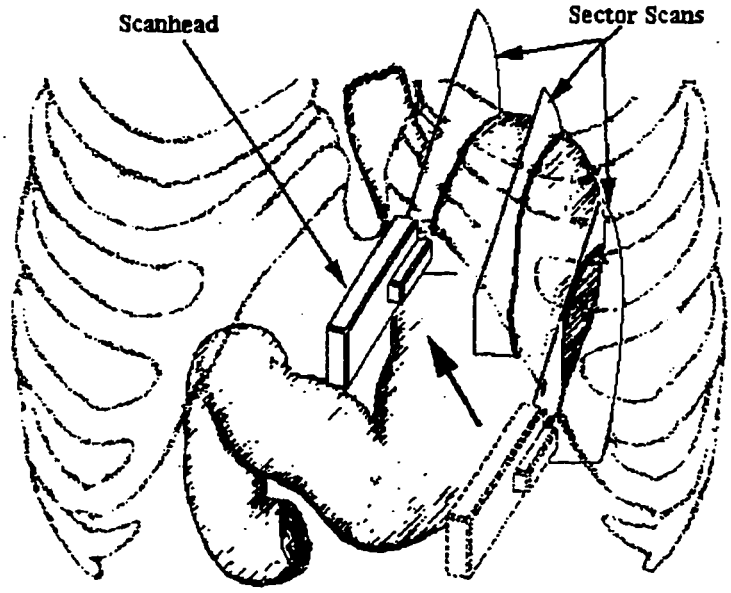

(b)

Figure 1.1 Freehand 3D ultrasound scan of (a) distal part of the stomach, and (b) proximal part of the stomach (anterior view).

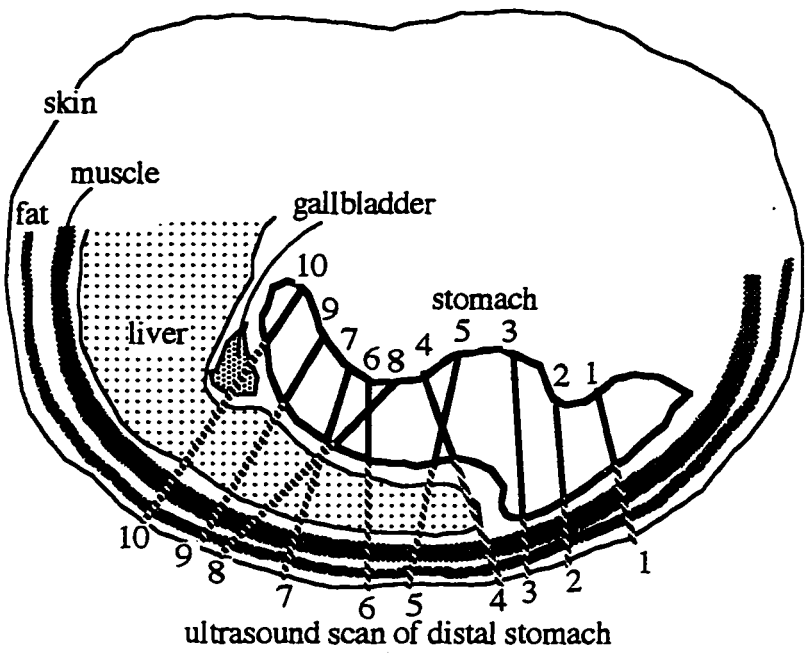

Figure 1.2 A transverse section of the abdomen showing the possible cross contours in ultrasound scan.

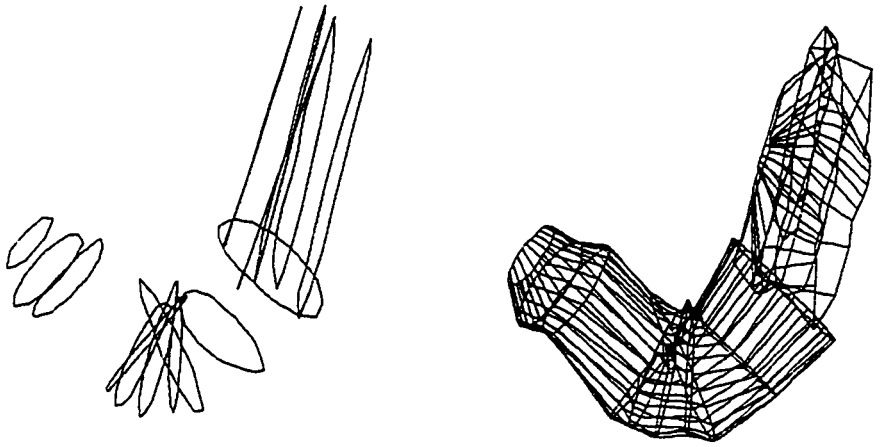

(a) (b)

Figure 1.3 3D view of the stomach in (a) contours, and (b) wireframe.

Chapter 2
Ultrasound Systems

2.1 Basic Ultrasound Physics and Image Formation

The basic concept of ultrasound physics and image formation pertinent to this research is briefly reviewed in this section. More detailed descriptions can be found in many sources, for example [35-38].

Ultrasound waves are high frequency acoustic waves (5 MHz in this research) generated by exciting a piezoelectric transducer with a spike of high voltage applied across the transducer. The voltage causes the transducer to vibrate and emit a burst of acoustic waves. The transducer is sealed in a hand-held scanhead, and the acoustic waves are coupled to the internal tissues of the patient by placing the scanhead in contact with the skin. The ultrasound waves observe the laws of mechanics and can undergo refraction, diffraction, and absorption as well as scattering reflection. When the waves encounter tissue interfaces with changes in characteristic acoustic impedance, echoes are reflected back to the transducer. After the transmit pulse is applied, the role of the transducer switches to a detector for a period of time to continuously detect the echoes coming from different depths. The detected echoes are converted to electric signals, then amplified, processed, and displayed.

Assuming the ultrasound waves propagate through tissue at a constant velocity, the distance between the transducer and the echo producing tissue interface is given by

$$d = \frac{c \cdot t}{2}$$

where d is the distance, c is the speed of sound in the tissue, and t is the time between the transmit pulse production and echo reception. The speed of sound varies with tissue type and temperature, e.g. fat = 1450 m/sec, muscle = 1585 m/sec, and blood = 1570 m/sec for human tissue at 37°C [35, 39]. The generally accepted value for the average speed of sound in human tissue is 1540 m/sec.

As the ultrasound waves travel through the tissue, much of the energy is dissipated by attenuation due to tissue absorption, scattering, and beam divergence. The attenuation is

generally around 1 dB per centimeter per megahertz for soft tissues. Since about 70 dB of round-trip attenuation in tissue can be tolerated, the maximum depth into the body that can be imaged by ultrasound is about 230 wavelengths [40]. In ultrasound instruments, the attenuation is usually compensated by increasing the gain of the echo-receiving amplifiers according to the time when the echo is received (the length of time is approximately proportional to the depth).

Specular (angle dependent) reflection will occur if the surface interface between two media, e.g. two different tissues, are large and smooth compared to the wavelength. The reflectivity depends on the difference in characteristic acoustic impedance between two media. The higher the reflectivity, the stronger the echo is and the less acoustic energy is transmitted through the interface. The characteristic impedance of a material is equal to the product of its density and the speed at which ultrasound propagates within it. The intensity reflectivity R of an interface is given by

$$R = \left(\frac{Z_2 - Z_1}{Z_2 + Z_1} \right)^2$$

where Z_1 and Z_2 are the characteristic impedances of the two media [37]. Because of the large mismatch in impedance, the soft tissue and bone interface has a high reflectivity coefficient which accounts for ultrasound's inability to penetrate bones [35].

Any acoustic energy that is not reflected is transmitted through the interface according to Snell's Law:

$$\frac{\sin\theta_1}{c_1} = \frac{\sin\theta_2}{c_2}$$

where θ_1 is the angle of incidence in medium 1, θ_2 is the angle of refraction in medium 2, and c is the speed of sound in the respective media [37]. In contrast to specular reflection and refraction, diffuse reflection (scattering) occurs, when the reflective surfaces are rough or small (on the order of the wavelength or smaller). Diffuse reflection from red blood cells is especially important for measuring the blood flow velocity with ultrasound [35].

One ultrasound beam represents the received echoes from all depths of interest associated with one transmitted pulse. One way of achieving a 2D scan is by electronically steering the beam with a phased array transducer which consists of a series of small and closely spaced piezoelectric transducer elements aligned linearly. Every element is pulsed at carefully scheduled timing (nanoseconds before/after the others), so the phases of the transmitted spherical wavefronts reinforce along a specific direction according to Huygen's principle [36], as illustrated in Figure 2.1. The echo signal received from every element is delayed by the same schedule before being summed together, so the echoes effectively return from the same angle as the transmitted pulse. Thus, a fan-shaped area can be scanned by electronically sweeping the beam without moving the scanhead.

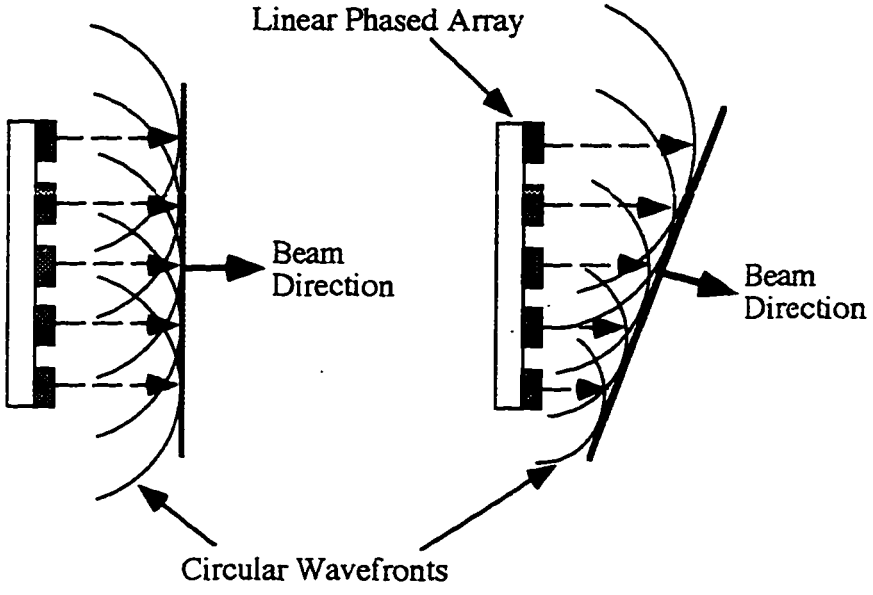

Figure 2.1 The Huygen's principle.

The positions of the scanlines are converted from polar coordinates (θ, r) to Cartesian coordinates (x, y) or (row, column), and the intensities of the scanlines are interpolated to display the image on the video screen. The image must be reconstructed every 33 msec if new information is to be updated at NTSC video frame rates. Because of the limitation of the speed of sound, this 33 msec limit causes a trade-off between the maximum number of scanlines and the maximum depth that can be scanned. For example, it is limited to about 128 scanlines for the depth of 19.9 cm.

Spatial resolution, the ability to resolve two closely spaced reflecting points, varies between ultrasound instruments and scanheads. Figure 2.2 shows the convention for directions (range, lateral, and elevation) related to beam propagation from a transducer. The range resolution depends on the transmitted frequency and the duration of the transmitted pulse. The higher the frequency and the shorter the pulse, the better the range resolution. However, because the attenuation of ultrasound by human tissue increases with increasing frequency, the maximum frequency is limited by the depth to which the ultrasound must penetrate to image the desired tissue.

The lateral and elevation resolutions are related to the ultrasound's beam profile (acoustic intensity field), as shown in Figure 2.2, and are subject to diffraction effects. In the near field region, the beam width is about the same as the width of the transducer. This region is characterized by rapid fluctuations of acoustic intensity due to the complex interaction of the phases and amplitudes of the transmitted pressures arriving from the different regions of the transducer's face. In the far field region, the intensity changes gradually and the beam spreads out beyond the width of the transducer. The lateral and elevation resolutions deteriorate as the beam travels further away from the transducer. The transition zone between the near field and far field has the best resolution because of the focus of acoustic intensity (narrow beam profile). The beam width of this focal zone is usually further narrowed and brought closer to the transducer by applying an acoustic lens on the surface of the scanhead. The beam profile in lateral direction can also be dynamically adjusted by tuning the pulsing schedule of the transducer elements [35, 36]. In contrast, the beam profile in the elevation direction is fixed for a linear phased array, and the thickness of the image plane is usually ignored in 2D imaging. The lateral and elevation resolutions are almost always worse than the range resolution, so they are likely to contribute more to the spatial location uncertainty in 3D ultrasound.

2.2 3D Ultrasound

A true 3D ultrasound scanhead would allow the acquisition of 3D data without moving the scanhead. There are two types of true 3D scanheads. The first type has a 2D phased array transducer which allows steering the ultrasound beam in both lateral and elevation directions [41, 42]. The second type usually has a built-in motor to rotate the transducer within the scanhead, and multiple 2D images can be acquired at fixed increments of the rotation angle [29, 43].

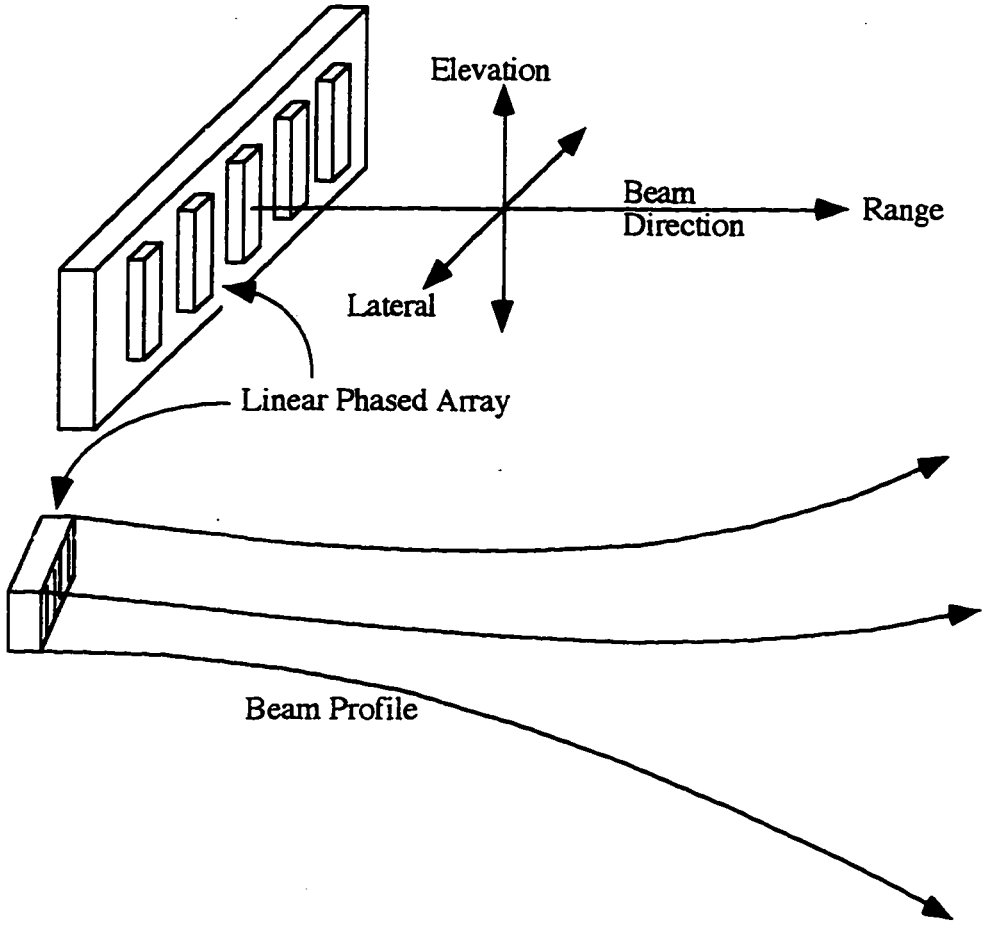

Figure 2.2 The convention for directions related to beam propagation and the beam profile. The range direction is the same as the ultrasound beam direction, the lateral direction is perpendicular to the beam direction and parallel to the transducer array, and the elevation direction is the third orthogonal direction.

Because the beam steering and motor motion automatically follow a preset regular pattern, true 3D scanheads allow rapid data acquisition, especially with the 2D phased array transducer which can have multiple receiving beamforming systems (Huygen's principle) to "listen" to multiple slightly different directions with each transmitting pulse. Note that the speed of sound still poses a limit as in conventional 2D ultrasound, because there can only be one transmitting pulse at a time, one must wait to send the next pulse until all the echoes from the previous pulse have arrived at the transducer. Another advantage of a true 3D scanhead is the reconstruction of the volume is simple, because the 3D relationship of the data is known *a-priori*. It is also easy to keep the acoustic contact with the patient, because a true 3D scanhead maintains a fixed position during data acquisition. Consequently, the disadvantage for a true 3D scanhead is the limitation of the field of view to a single acoustic window, which is not suitable for scanning large organs such as the stomach [29]. Also, as the complexity of the scanhead increases, it may become bulky and heavy. Thus, it is difficult and expensive to manufacture a light and small true 3D scanhead.

A volume of ultrasonically interrogated tissue can be reconstructed from multiple 2D images, as long as the position and orientation of the scanhead is known for each image. Thus, a 2D ultrasound system can be economically extended to a 3D ultrasound system by adding either mechanical constraints to the scanhead's motion or a position and orientation measurement (POM) device to track the scanhead's motion. The mechanical constraints usually only allow tilting or linear translation of the scanhead in one degree of freedom. It can be motor or manually driven [44-46]. A scanhead equipped with a POM device permits up to six DOF in scanning the patient, so it is called freehand scan. Mechanical arms[47-49], acoustic [34, 50-52], or electromagnetic [53, 54] POM devices have been used.

A mechanically constrained scanhead follows a rigid scan path, so the spatial relationship between images is simple, and the 3D volume is straightforward to reconstruct. Potentially, it has superior alignment accuracy, because the position error results along only one DOF. However, an acoustic window of the scanhead with a tilting constraint is usually too narrow, and the scanhead of a linear translation constraint may loose acoustic contact with the body surface due to the lack of flexibility along the scan path.

As described in Section 1.5, a major disadvantage with freehand 3D ultrasound is the complex spatial relationship between images, which can make the reconstruction and volume computation of the anatomic structures difficult. However, only freehand scanning provides full exploration of acoustic windows which are crucial for scanning the whole stomach. Furthermore, freehand scanning permits image acquisition of optimum quality, because the position and orientation of the scanhead can be adjusted for each acquired image. Thus, a freehand scanning system is the best choice for obtaining stomach volumes.

The accuracy among mechanical arm, acoustic, and electromagnetic POM devices are comparable, about 1 - 2 mm of uncertainty in locating a single point in 3D space [34, 48, 49, 55-57]. However, they operate on different principles, and are quite different in terms of physical size and environmental requirements.

A mechanical arm is an assembly of shafts and gears with potentiometers for measuring the angle or translation of every moving joint. The scanhead is mounted at the end of the mechanical arm, so the position and orientation of the scanhead can be computed from the readings of the potentiometers. The accuracy of a mechanical arm is immune to any environmental interference. However, the operation of the scanhead is still constrained mechanically. Typical mechanical arms offer only 3 - 5 DOF [47-49], so they barely qualify as freehand scan systems. Further increasing the DOF not only complicates the system design, but also potentially increases the measurement variability.

In an acoustic POM device [34, 51, 52], a trio of spark gaps are attached to the scanhead to sequentially emit shock waves with various frequency components. A microphone array over the examination bed is tuned to receive the signals of approximately 100 KHz. The position and orientation of the scanhead are derived from measuring the time of flight of the shock waves in the air from each spark gap to the microphones. Although the fixture (a 9 cm diameter plastic disk in [34]) for the spark gaps is not small, there is no mechanical constraint, and the scanhead can move freely with 6 DOF (3 DOF for translation, and 3 DOF for rotation). The drawback of acoustic POM devices is the need of maintaining unobstructed line of sight between the spark gaps and the microphones, which severely limits the scanhead's orientation. Additionally, the velocity of sound in air is not constant; random air current and the variation of room

temperature and humidity all affect the accuracy. Some patients can not tolerate the crackle and flash of the spark gaps [55, 56].

The magnetic POM system used in this study is based on a pulse-flux magnetometer and consists of an electronic system control unit, a transmitter, and a receiver. The receiver picks up the strength of the magnetic field emitted from the transmitter, permitting the control unit to track of the position and orientation of the receiver relative to the transmitter. The receiver is attached to the ultrasound scanhead, and the transmitter is usually attached under the examination bed or behind the examination chair (if the patient is scanned in a sitting position). Because of the small size of the receiver (6 mm x 6 mm x 9 mm) and because there is no need to maintain a line of sight between the transmitter and the receiver, magnetic POM devices offer the highest flexibility in image acquisition. However, any magnetic or electrically conductive objects, stray magnetic fields, and electromagnetic noise in the measurement area may distort the magnetic field generated by the POM transmitter and affect the accuracy of measurement. The examination bed/chair used in our laboratory is constructed from wood/plastic using brass hardware. The receiver is attached to the scanhead with brass/plastic screws and glue. It was verified that the induced fields from the signals in the scanhead or the metal parts within the scanhead does not affect the accuracy [56].

There are three orthogonal coils in the transmitter and receiver, respectively. The transmitter emits three orthogonal pulses of magnetic fields in sequence, and the receiver senses the strength of the magnetic fields in its own three orthogonal directions with respect to each emitted pulse of magnetic field. The relationship between the transmitter's axis system (x, y, z) and the receiver's axis system (a, b, c) is depicted in Figure 2.3. After subtracting the ambient field strength, which is measured by an additional receiver sensing cycle with no fields generated by the transmitter, the distance and orientation of the receiver's axis system with respect to the transmitter's can be determined. The distance is reported as the x, y, and z location of the receiver's axis origin with respect to the transmitter's origin:

$$\begin{bmatrix} R_x \\ R_y \\ R_z \end{bmatrix}.$$

The orientation is reported as a matrix of angle cosines; each angle cosine value gives the unit vector projection of a receiver's axis onto the transmitter axis:

$$\begin{bmatrix} R_{ax} & R_{bx} & R_{cx} \\ R_{ay} & R_{by} & R_{cy} \\ R_{az} & R_{bz} & R_{cz} \end{bmatrix}.$$

These twelve parameters are updated in real time by the control unit (100 times per second in our system).

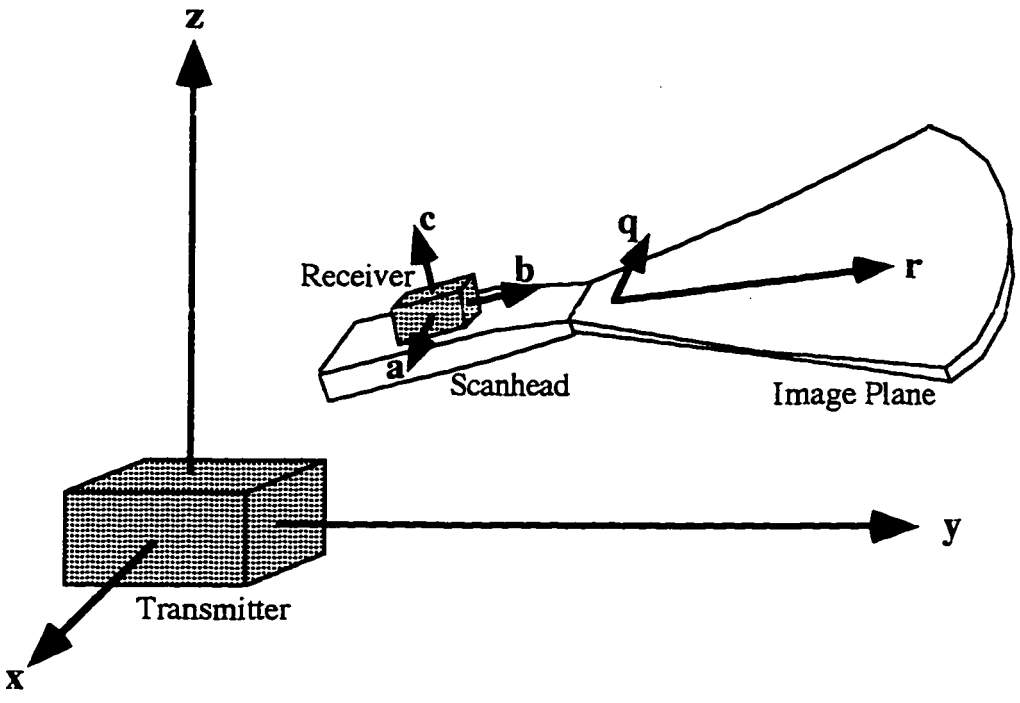

Figure 2.3 Axis systems for the POM transmitter, receiver, and the image plane.

Figure 2.3 also depicts the relationship between the receiver's axis system (a, b, c) and the image plane's axis system (r, q), where r and q represent the row and column of the image plane, respectively. In a similar manner, the distance and orientation of the image plane's axis system with respect to the receiver's can be represented as

$$\begin{bmatrix} S_a \\ S_b \\ S_c \end{bmatrix} \quad \text{and} \quad \begin{bmatrix} S_{ra} & S_{qa} \\ S_{rb} & S_{qb} \\ S_{rc} & S_{qc} \end{bmatrix}.$$

Because the receiver is firmly attached on the scanhead, these nine parameters are fixed for the images with the same range and lateral resolutions which are controlled by the depth setting in an ultrasound instrument.

The physical 3D location of each pixel on the image plane can be computed through a two-step process of mapping the image plane's axis system (r, q) into the receiver's axis system (a, b, c), then mapping this result into the transmitter's axis system (x, y, z). The cascade of the two mappings is:

$$\begin{bmatrix} p_x \\ p_y \\ p_z \end{bmatrix} = \begin{bmatrix} R_x \\ R_y \\ R_z \end{bmatrix} + \begin{bmatrix} R_{ax} & R_{bx} & R_{cx} \\ R_{ay} & R_{by} & R_{cy} \\ R_{az} & R_{bz} & R_{cz} \end{bmatrix} \begin{bmatrix} S_a & S_{ra} & S_{qa} \\ S_b & S_{rb} & S_{qb} \\ S_c & S_{rc} & S_{qc} \end{bmatrix} \begin{bmatrix} 1 \\ p_r \\ p_q \end{bmatrix} \qquad (2.1)$$

where (p_r, p_q) is the coordinates of pixel p in (r, q) axis system, and (p_x, p_y, p_z) is the corresponding coordinates in (x, y, z) axis system [56].

Chapter 3
Review of Volume Computation

3.1 Fundamentals of Volume Computation

The volume of an irregularly shaped object is generally computed based on the principle of divide-and-conquer: divide the object into multiple simple geometric elements, and compute the volume of each element. The object's volume is equal to the sum of all the elemental volumes. Depending on how the object is sampled and what type of algorithm is used, different shapes of simple geometric elements in different hierarchical levels are used.

Riccabona, et al. [27] densely sampled the urinary bladder to generate volume data which filled the sampled space with small cubic elements called voxels. (A voxel in 3D volume data is analogous to a pixel in a 2D image.) The volume data was manually masked to exclude all voxels which were outside of the bladder. The volume of the bladder was then equal to the product of the number of remaining voxels and the unit voxel volume. Significant computer storage was required for the volume data because of the dense sampling of the anatomic structure.

The trapezoidal or Simpson's rule [58] is often used to approximate the volume outlined by parallel cross-sectional contours based on outlines of borders in the images. Assuming A_1, A_2, and A_3 are the areas of three parallel contours, and the distance between adjacent contours is D. The outlined volume by the trapezoidal rule is

$$\frac{D}{2}(A_1 + A_2) + \frac{D}{2}(A_2 + A_3).$$

The outlined volume by the Simpson's rule is

$$\frac{D}{3}(A_1 + 4A_2 + A_3).$$

The Simpson's rule is usually more accurate than the trapezoidal rule, because the former is based on parabolic interpolation, and the latter is based on linear interpolation. Bolondi, et al. [4, 16] sampled the gastric antrum at both ends and the middle to obtain

three contours using conventional 2D ultrasound. The contours were assumed to be parallel, and the volume was computed based on the trapezoidal rule. Fisher, et al. used Simpson's rule to compute the volume of cardiac left ventricles using parallel and equal-distance cross-sectional images obtained using intracardiac ultrasound [59].

The total volume of a region is the sum of the individual volumes between every two consecutive contours, if the cross-sectional contours do not intersect each other (either using parallel or non-parallel contours). Gilja, et al. [28, 29] and King's research group in Columbia University [52] resampled each contour into the same number of points (N), found the centroid of the N points, and generated N wedges or sectors around the centroid line between every two adjacent contours. Each wedge was then decomposed into three tetrahedra as shown in Figure 3.1(a). Thus, the volume between two slices was decomposed into $3N$ tetrahedra. The volume of a tetrahedron is equal to

$$\tfrac{1}{3}\beta \cdot h$$

where β is the base area, and h is height of the tetrahedron, as shown in Figure 3.1(b). The volumes of all tetrahedron were summed to yield the total volume.

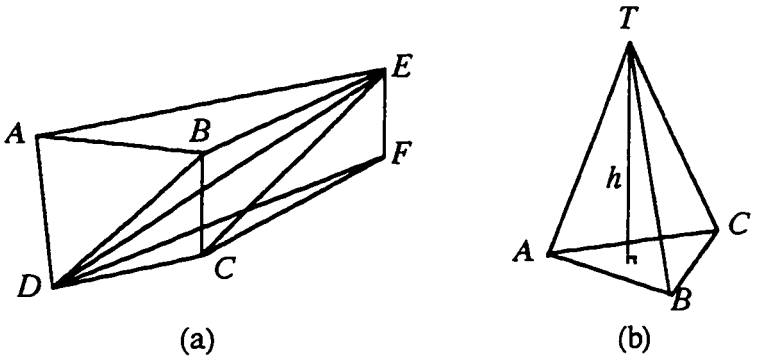

Figure 3.1 (a) A wedge or sector *ABCDEF*. *A* and *B* are two adjacent points in a contour, and *C* and *D* are the corresponding points in the next contour. *E* and *F* are the centroids of the respective contours. The wedge can be divided into three tetrahedra *ABDE*, *BCDE*, and *CDFE*. (b) The volume of a tetrahedron *ABCT* is equal to $\frac{1}{3}\beta \cdot h$, where β is the area of base *ABC*, and h is the height from point *T* to the base.

Handschumacher, Jiang, et al. [24, 51] also divided a cardiac ventricle into multiple tetrahedra for computing its volume using a slightly different approach. The entire ventricle surface was treated as contiguous triangular patches, each forming a tetrahedron with the centroid of the ventricle. The limitations of these tetrahedron based methods are that the centroid must be inside the object, and the tetrahedra may overlap one another in regions of concavity. These limitations can be overcome by properly assigning a plus or minus sign to each tetrahedron volume, so that the sum of the signed volumes gives the correct total volume of the object. The detailed scheme of using signed volume is given later in this section (based on Green's and Gauss's theorem).

Instead of dividing the object along latitudes, Moritz, McCabe, and Martin, et al. [34, 60, 61] divided the object (cardiac left ventricle) longitudinally into sections similar to a citrus fruit. First, the central long axis of the object was derived from linear least square fitting of all the sampled points on the cross-sectional contours. Then, each contour was resampled at every fixed angle around the axis, and the area between the central axis and the resampled points at the same angle was computed for every angle. As illustrated in Figure 3.2, the shaded region is the area corresponding to an angle, and the volume computation problem is simplified from 3D to 2D. The total volume is the sum of all the sectors' area in Figure 3.2 (b):

$$\frac{\pi}{N}\sum_{i=1}^{N}\left[r(\tfrac{2\pi}{N}i)\right]^2$$

where N is the number of sectors, $r(\theta)$ is the longitudinal plane area at angle θ in Figure 3.2 (a). This algorithm has been shown to be very accurate in estimating the volume of the cardiac left ventricle *in vitro* (average error is 5%) [34, 60]. It can handle intersecting cross-sectional contours and partially missing border in the contours. However, a major limitation of this algorithm is that the central long axis must be inside all the contours in order to resample the contours correctly. Due to the curvature of the stomach, it is often impossible to find such an axis which is completely within the gastric cavity.

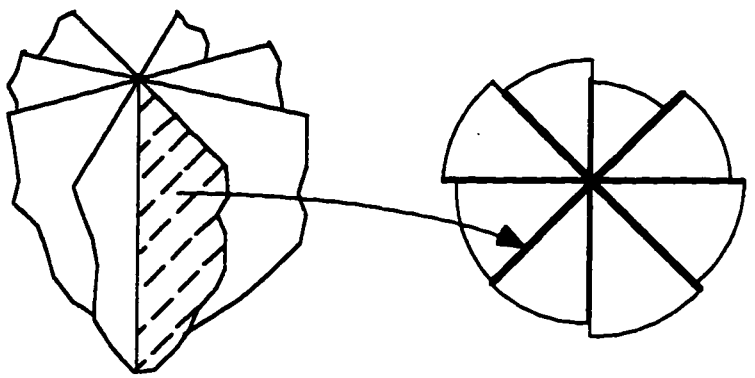

(a) (b)

Figure 3.2 The object is resampled at longitudinal planes at every fixed angle around the central long axis. (a) The area of each plane is computed. (b) The volume can be computed by summing all the sectors' area.

The relationship between the volume and surface of an object can be established by Gauss's theorem. It is easier to demonstrate a similar relationship in 2D space between the length of a contour (or polygon) and the area enclosed by the contour [62]. Green's theorem states that given continuous functions $M(x, y)$ and $N(x, y)$ having continuous partial derivatives over a region R which is enclosed by a contour C,

$$\iint_R \left(\frac{\partial N}{\partial x} - \frac{\partial M}{\partial y} \right) dx\, dy = \int_C M\, dx + N\, dy .$$

If we set $M = -y$ and $N = x$, we obtain the formula for the area of the region:

$$\begin{aligned} A = \left| \iint_R dx\, dy \right| &= \tfrac{1}{2} \left| \int_C x\, dy - y\, dx \right| \\ &= \tfrac{1}{2} \left| \sum_{i=1}^{n} \left[(x_i y_{i+1} - x_i y_i) - (y_i x_{i+1} - y_i x_i) \right] \right| \\ &= \tfrac{1}{2} \left| \sum_{i=1}^{n} \left[x_i y_{i+1} - x_{i+1} y_i \right] \right| \\ &= \tfrac{1}{2} \left| \sum_{i=1}^{n} \overline{op_i} \times \overline{op_{i+1}} \right| = \left| \sum_{i=1}^{n} A_{\Delta op_i p_{i+1}} \right| \end{aligned}$$

where we assume the contour C is resampled into n sequential points, $p_i(x_i, y_i)$, $i = 1, \cdots, n$, and $p_{n+1} \equiv p_1$; $\overline{op_i}$ is the vector from the origin of the coordinates to point p_i. Because translating the contour does not change its area, the origin of the coordinates can be arbitrarily defined somewhere close to the contour to increase the accuracy (the origin does not have to be inside the contour). The area enclosed by the contour is algebraically equivalent to summing the signed areas of all the component triangles formed between the origin and every two adjacent points on the contour. This method is valid even for nonconvex contours. Figure 3.3 illustrates how the signed areas of the component triangles are summed to give the total area of a nonconvex contour.

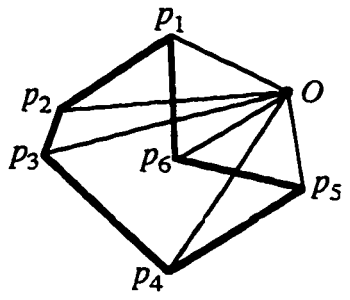

Figure 3.3 Seven points lie in the plane of the paper; the area enclosed by the contour $p_1p_2p_3p_4p_5p_6$ is equal to the sum of the signed areas of the six triangles: $|\Delta Op_1p_2| + |\Delta Op_2p_3| + |\Delta Op_3p_4| + |\Delta Op_4p_5| - |\Delta Op_5p_6| - |\Delta Op_6p_1|$, where Δ is used to indicate a triangle composed of the following three points, e.g. ΔOp_1p_2 is the triangle formed by points O, p_1, and p_2.

In 3D space, if the contour lies on some arbitrary plane perpendicular to a unit vector $\mathbf{N}$, the area can be computed by

$$A = \frac{1}{2}\left|\mathbf{N} \cdot \left(\sum_{i=1}^{n} \overline{op_i} \times \overline{op_{i+1}}\right)\right|. \qquad (3.1)$$

Goldman [63] extended the same principle to compute the volume of a polyhedron which is equal to sum the signed volumes of all the component polyhedra formed between the origin and every surface patch (polygon) on the polyhedron:

$$V = \tfrac{1}{3}\left|\sum_{j=1}^{m} h_j \beta_j\right| \tag{3.2}$$

where β_j is the j'th surface patch area (the base area of a polyhedron), and h_j is the signed distance from the origin to the j'th surface patch (the height of a polyhedron), and $j = 1, \cdots, m$. Let

$p_{ij} \equiv$ the i' th contour point on the j' th surface patch

$\mathbf{N}_j \equiv$ a unit outward vector normal to j' th surface patch

$$= \left[(p_{1j} - p_{0j}) \times (p_{2j} - p_{0j})\right] / \left|(p_{1j} - p_{0j}) \times (p_{2j} - p_{0j})\right|.$$

From the previous result for contours, equation (3.1):

$$\beta_j = \tfrac{1}{2}\left|\mathbf{N}_j \cdot \left(\sum_{i=1}^{n} \overline{op_{ij}} \times \overline{op_{i+1,j}}\right)\right|. \tag{3.3}$$

The signed distance h_j is equal to the projection to the normal vector $\mathbf{N}_j$ of any vector starting from the origin to any arbitrary point on the surface patch, so

$$h_j = \overline{op_{0j}} \cdot \mathbf{N}_j. \tag{3.4}$$

Putting equations (3.2), (3.3), and (3.4) together, the final formula for computing the volume of a polyhedron is

$$V = \tfrac{1}{6}\left|\left\{\sum_{j=1}^{m} (\overline{op_{0j}} \cdot \mathbf{N}_j)\left|\mathbf{N}_j \cdot \left(\sum_{i=1}^{n} \overline{op_{ij}} \times \overline{op_{i+1,j}}\right)\right|\right\}\right| \tag{3.5}$$

Note that the unit normal vectors of all surface patches need to consistently point outward or inward. This formula is valid even for nonconvex polyhedra. The algorithms for computing the stomach volume in this research are based on equation (3.5).

3.2 Surface Reconstruction

Before applying the divide-and-conquer principle, such as equation (3.5), to compute the volume of an irregular shaped object, the sampled points usually need to be resampled (interpolated) and organized (sorted) into a certain sequence. Based on this sequence, multiple simple geometric elements can be created without overlapping one another or leaving gaps excluded from the object's volume. The process of resampling and organizing sampled points is equivalent to surface reconstruction which is a very active research topic in computer vision and computer graphics. Many algorithms have been proposed, yet there is no perfect method. Because there is no unique solution, the surface reconstruction problem is ill-defined in nature. There are always some pathologic shapes which can fail the most sophisticated method. Which algorithm to use depends on the source of the data, the shape of the object, and how the surface of the object is sampled (parallel contours, non-parallel contours, scattered points, etc.).

The organ is scanned in parallel slices in many medical imaging modalities, such as X-ray CT, MRI, and mechanical constrained linear translation 3D ultrasound. After outlining the boundary of the organ on every slice, multiple parallel contours in 3D space are obtained. The surface of the organ can be reconstructed by building surface patches between contours on adjacent slices, such as triangle patches [30] or curvature patches based on 2D splines [64]. Usually, a least distance criterion is used to find the corresponding points between successive slices for building surface patches. However, the process of finding the corresponding points can be complicated and often requires manual interventions if the contours on two successive slices are very different [65-67]. For example, the contour line of brain cortex may have different deep narrow concavities and a different number of contours on two successive slices. Fortunately, many organs, such as cardiac ventricles, kidney, and stomach, are fairly smooth and well integrated, so their cross-sectional contours are quite elliptic, and there is only one contour per slice. It is usually possible to resample the contours at fixed angles to obtain equal number of points on each contour for building surface patches [28, 61]. Because the cross-sectional contours in this stomach research are not parallel and may intersect one another, the surface cannot be reconstructed simply by building surface patches between consecutive contours.

The aforementioned longitudinal sectioning method by Moritz, McCabe, and Martin, et al. [34, 60, 61] (Section 3.1) can handle intersected cross-sectional contours. There was also a similar algorithm developed by Brinkley, et al. [50]. The resampled points at the same angle from all the contours are sorted and connected before computing the area of the longitudinal plane as shown in Figure 3.2 (a). The sorting is based on a nearest distance criterion. First, the point closest to the central long axis is selected as the starting point in a sorted list. Next, the nearest point to the starting point is found and appended as the second point in the sorted list. Then, the nearest point to the second point is found and appended in the sorted list. This process iterates until all remaining points have been sorted and linked in the list. In the sorting process, if the distance from the first point to the new point is less than the distance from the last point to the new point, then this indicates that the first point is not an end point. The new point becomes the first point, and all the previous sorted points descend one position in the sorted list.

Besides being able to handle intersecting contours, the longitudinal sectioning method is also capable of handling partially missing border in the contour, because the number of points does not have to be the same for every sorted list. However, there are two drawbacks which limit this method in stomach volume applications. The first is that it is difficult to find a central long axis completely within the gastric cavity because of the curvature of the stomach, as mentioned in Section 3.1. The second is that the nearest distance based sorting method is prone to error [60]. Figure 3.4 (a) illustrates a list link sorted by using the nearest distance criterion. Point A is the first point in the link, point B follows, etc. Because point E is somewhat far away from the neighboring points, point E will be incorrectly linked as an end point in the list. The desired list link is shown in Figure 3.4 (b).

Handschumacher, et al. [51] reconstructs the surface of a cardiac left ventricle by deforming a spherical template to fit multiple intersecting cross-sectional contours in both the short and long axes of the cavity. The spherical template consists of evenly spaced lines of latitude and longitude to provide about 500 grid points. It is initially positioned at the geometric center of the cavity. Imaginary rays are extended from the center of the sphere through the grid points toward the contours to calculate the corresponding points on the ventricular surface by best fitting to all contour segments

within a conical sector (10.6°) around each ray. Rays without adjacent contour segments are interpolated from nearest neighbors. This method is suitable for reconstructing an object which does not differ greatly from a sphere. Because the shape of the stomach is elongated and curved, the rays could intercept the stomach surface more than once, which limits its applicability.

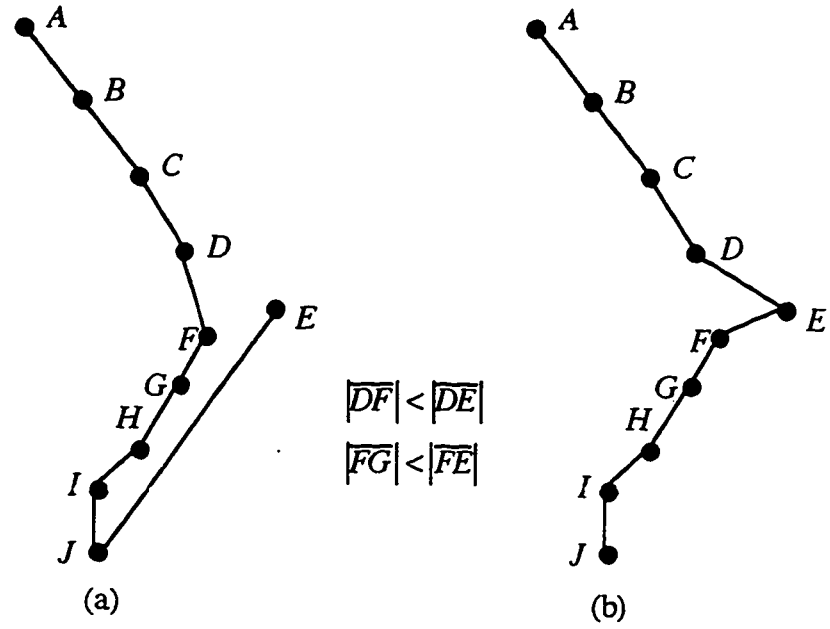

Figure 3.4 An error in the sorting based on nearest distance criterion. (a) incorrect sorting, point *E* becomes an end point; (b) correct sorting.

Some smooth surface fitting algorithms are developed for Z values given at points irregularly distributed in the X-Y plane, also called $2\frac{1}{2}$D range data [68, 69]. Because only a single Z value is allowed for each (X,Y) coordinates, a closed surface needs to be divided into multiple regions. It is possible to build multiple surface patches one by one using this approach, however, it is not easy to seam all the patches together. Also, the surface will be very sensitive to the choice of the points for each patch.

Recently, a volume spline based on Green's function was used to reconstruct geometric models and surfaces from scattered points [70]. It results in the representation of a solid by an inequality $f(x,y,z) \geq 0$, and the surface defined by the implicit equation $f(x,y,z) = 0$. This algorithm can generate highly concave and branching objects

automatically with the major drawback of its high computation complexity. This algorithm shows promise, since it can be efficiently paralleled.

Spherical harmonics or other surface harmonics are commonly used in modeling the surface of the heart [71]. The surface is represented in the form of a linear combination of orthogonal basis functions, which is conceptually similar to Fourier series. Spherical harmonics permit the decomposition of the object's shape into simple forms that can be ordered according to their increasing spatial complexity. Because the shape of the stomach is more irregular than that of the heart, it may require more than one harmonic fit.

Various active contour or active surface models have proliferated in computational vision and computer graphics in the past decade. Kass, et al are the first who elegantly described an active contour model, called the snake, for edge detection [72]. A snake is a spline which approaches features such as edges during an iterative energy-minimization process. Energy is defined as external energy and internal energy, where external energy is defined as minus one times local gradient, and internal energy is defined as the weighted sum of spline length and curvature. Thus, the snake approaches spots with higher gradients, yet a shorter and lower curvature snake is preferred. Depending on applications and preference, the active model is also called a deformable model, and the internal energy is dubbed as a constraint, regularization, stablizer, or spring force. The external energy usually directly corresponds to the objective of the algorithm, in this case, an edge.

The idea of active contour model has been extended to active surface models [73-78] and volume deformation models [79, 80] by many researchers for surface reconstruction and image registration. In active surface models, surface patches or meshes are first built according to the *a-priori* knowledge of the general shape of the object. The patches or meshes are attached to the data points by imaginary springs. The patches or meshes will move to approximate the shape of the data points, because they are pulled by the spring forces (external energy). There are also imaginary springs (internal energy) between patches or mesh points to maintain the continuity and smoothness of the surface. The surface reconstruction process is equivalent to the time evolution of a physical system which settles into a stable configuration of minimum potential energy. The volume

deformation model is based on the same principle to deform an *a-priori* knowledged volume to match the shape of the data points in 3D space.

In general, deformable models are very powerful and flexible tools for surface reconstruction. However, most of the surface reconstruction methods using deformable models were demonstrated with densely sampled range data or in 3D voxel space; their accuracy on sparsely sampled data is unknown due to the ill-defined nature of surface reconstruction.

As stated in Section 1.5, two approaches for computing the stomach volume are reported in this dissertation. In the first method (detailed in Chapter 4), the concept of surface reconstruction from cross-sectional contours to a wireframe is inspired by the aforementioned method of Moritz, McCabe, and Martin, et al. [34, 60, 61]. In the second method (detailed in Chapter 5), a volume deformation model based on Szeliski's method [79] is used to approximate the stomach surface.

Chapter 4
Computing Stomach Volume with Dot-Product Sorting Method

4.1 Overview

As described in Section 1.5, the proximal and distal parts of the stomach were scanned from different orientations. The proximal stomach was sampled lengthwise into three to eight approximately parallel contours, while the distal stomach was sampled in short cross sections into eight to twelve nonparallel contours. The proximal and distal volumes could be computed independently, and the sum of these two volumes was the total stomach volume.

Conceptually, the volume computation method presented in this chapter consists of three major processes: resampling the contours, rearranging the links between contours, and computing the volume. It is necessary to resample each contour into the same number of border points, so that all the contours can be linked together to form a wireframe. A *link* is defined as the line segment which connects a point on one contour to a corresponding point on another contour. A *wire* is defined as the union of all the joined links. Figure 4.1 illustrates the definition of contour, link, and wire.

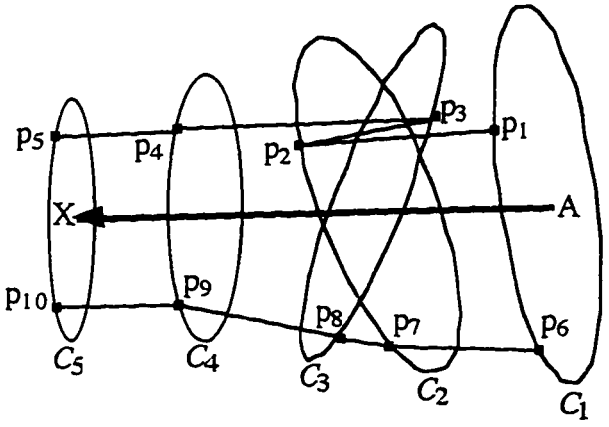

5 contours: C_1, C_2, C_3, C_4, C_5.
8 links: p_1p_2, p_2p_3, p_3p_4, p_4p_5, p_6p_7, p_7p_8, p_8p_9, p_9p_{10}.
2 wires: $p_1p_2p_3p_4p_5$, $p_6p_7p_8p_9p_{10}$.

Fig. 4.1 Contour, Link, and Wire.

The wires in Figure 4.1 are generated by linking the corresponding point in each contour in the order of the ultrasound scan. Because contours C_2 and C_3 intersect each other, the upper wire has an incorrect zigzag shape. The order of link-points p_2 and p_3 must be exchanged to obtain the correct wire $p_1p_3p_2p_4p_5$. Our method for rearranging links

is based on the vector dot-product, or inner-product: $\mathbf{a} \cdot \mathbf{b} = |\mathbf{a}||\mathbf{b}|\cos\theta$, where θ is the angle between vectors **a** and **b**. The value of the dot product is positive, if $|\theta| < 90°$; otherwise, it is non-positive. Suppose Figure 4.1 is a part of the distal stomach, and $\overline{AX}$ is the central long axis of this part of the stomach. $\overline{AX} \cdot \overline{P_1P_2}$, $\overline{AX} \cdot \overline{P_3P_4}$, and $\overline{AX} \cdot \overline{P_4P_5}$ are all positive; only $\overline{AX} \cdot \overline{P_2P_3}$ is negative. Thus, we know that the order of link-points p_2 and p_3 should be exchanged. After the exchange, all the links $\overline{P_1P_3}$, $\overline{P_3P_2}$, $\overline{P_2P_4}$, and $\overline{P_4P_5}$ have positive dot-product value with $\overline{AX}$.

It is necessary to consider two facts for the dot-product method to work in the real world. First, the stomach is a J-shaped organ, so the central long axis $\overline{AX}$ needs to be bent accordingly for it to better represent the trend of the wires on the wireframe. Second, it is possible to have more than two contours which intersect one another, which makes the sorting of link-points difficult. The centroids of all the contours are sorted and linked to form a central wire to simulate the bent central long axis. A bubble sort algorithm [81] has been used to sort link-points. The terms "Sorting link-points" and "rearranging links" are actually identical, so they are used interchangeably through this chapter.

4.2 Procedure for Volume Computation

The algorithm of the volume computation consists of the following six steps. Each step will be explained in each subsection, from Section 4.2.1 to 4.2.6.

Step 1: manually outline the border of the stomach to form a contour from each image.
Step 2: compute the centroids for all the contours.
Step 3: resample the contours to get the same number of samples along each contour.
Step 4: rearrange the centroid-links.
Step 5: rearrange the wireframe-links.
Step 6: Computing the volume using the Gauss theorem based method.

The whole algorithm was programmed using the C language *, and integrated with the Application Visualization System software package, version 5.01 (Advanced Visual Systems Inc., Waltham, Massachusetts, USA) running on a DEC Alpha 3000 - 300 workstation. The Application Visualization System was used mainly to provide the user interface, such as file browsers, slide bars, dials, buttons, and the displays of both 2D images and 3D geometry.

4.2.1 Manual Outlining

Computerized volume estimation starts with interactive manual outlining with a mouse on the computer display. The inner echo interface of the gastric mucosa was chosen for manual outlining in all samples. In cases of the presence of an air pocket in the top portion of the stomach, the outer border of the air pocket was traced. Example images of the proximal and distal stomach with manual outlines are shown in Figure 4.2. The outlined points are in sequential order, i.e. in either clockwise or counterclockwise order. All the neighboring points are connected with straight line to form a closed contour (also called polygon).

The two compartments of the stomach were scanned in two separate transducer movements in this study, so the border region between the proximal and distal stomach was captured in both scans. To avoid including this overlapping region in the volume computation twice, this region was excluded in the outlines of the proximal stomach. The operator was provided with a 3D view of the outlined contours, as shown in Figure 1.3 (a) of Section 1.5, which was updated in real time as the operator traced the sonongraphic images. (See equation 2.1 in Section 2.2 for the 2D to 3D geometric transformation.) The distal stomach was outlined first, then the proximal stomach was outlined based on both the sonongraphic images and the feedback from the 3D view of the outlined distal stomach contours. The top portion of the proximal stomach image in

---

* The source code can be obtained by contacting the author through email: jong@u.washington.edu.

Figure 4.2(a) was not included in the outline, because it overlapped with the distal stomach. The process can be viewed as sewing the proximal stomach outlines onto the distal stomach, as in Figure 1.3 (a).

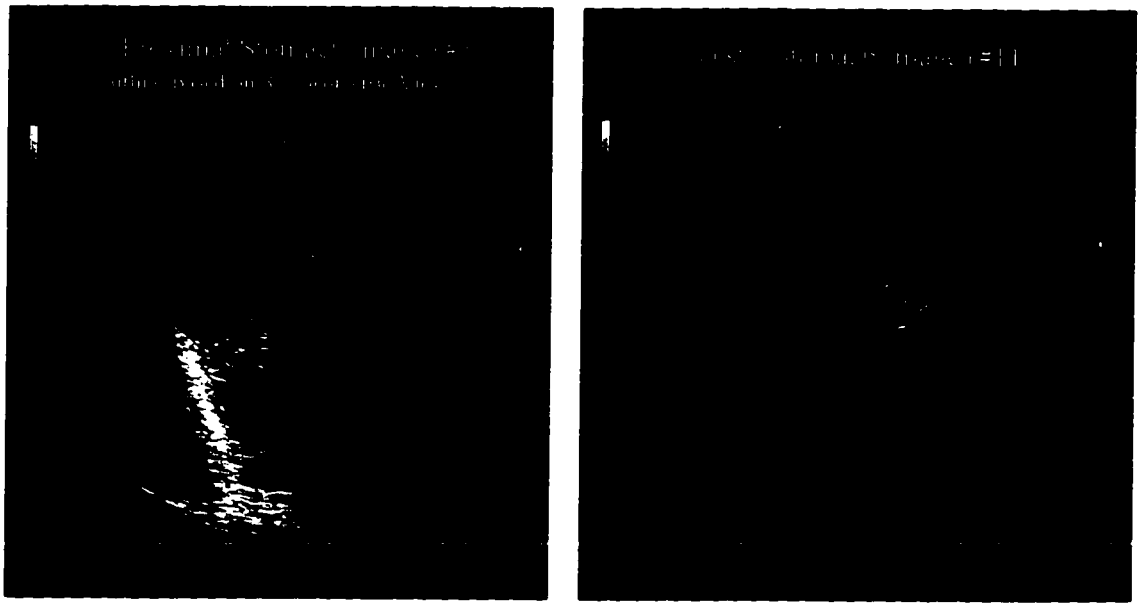

(a) (b)

Figure 4.2 A cross section image and outlining of (a) proximal stomach, and (b) distal stomach.

4.2.2 Computing Centroids

Regarding a contour as a planar 2D polygonal object with uniform density, the centroid of the contour is defined as the center of mass. The centroids of the contour are computed for the purpose of resampling the contour. Also, the central wire of the stomach is constructed by properly linking the centroids of all the contours.

Assume there are n outlined points $(x_i, y_i), i = 1, \cdots, n+1$, with $x_1 = x_{n+1}$ and $y_1 = y_{n+1}$. A naive method of computing the centroid $(\bar{x}, \bar{y})$ of the polygon enclosed by these n points is

$$\bar{x} = \frac{\sum_{i=1}^{n} x_i}{n}$$

$$\bar{y} = \frac{\sum_{i=1}^{n} y_i}{n}$$

which actually finds the center of mass of a massless polygon with equal point masses at its vertices. The centroid computed by this method is biased toward any side which is more densely sampled in the manual outlining. Instead, we applied a rapid and accurate moment-based method reported in [82], which is reviewed as follows.

Basic physics texts show that the centroid $(\bar{x}, \bar{y})$ of a closed planar region R is given by

$$\bar{x} = \frac{\iint_R x\,dx\,dy}{A} = \frac{\mu_x}{A}$$

$$\bar{y} = \frac{\iint_R y\,dx\,dy}{A} = \frac{\mu_y}{A}$$

where A is the area of R, and μ_x and μ_y are the first moments of R along the x- and y-coordinates, respectively. As described in Section 3.1, the area A can be calculated by equation (3.1):

$$A = \frac{1}{2}\sum_{i=1}^{n} a_i, \quad \text{where } a_i = x_i y_{i+1} - x_{i+1} y_i$$

Thus, the task is to compute μ_x and μ_y in order to compute $\bar{x}$ and $\bar{y}$.

Green's theorem states that

$$\int_C (M\,dx + N\,dy) = \iint_R \left(\frac{\partial N}{\partial x} - \frac{\partial M}{\partial y} \right) dx\,dy$$

where $M(x,y)$ and $N(x,y)$ are continuous functions, and have continuous partial derivatives over the region R, which is enclosed by a contour C. Letting $M = 0$ and

$N = \frac{1}{2}x^2$, the right side of the above equation equals μ_x, and the first moment can be computed as

$$\mu_x = \frac{1}{2}\int_C x^2\, dy.$$

To compute the right side of the above equation, we can represent the line segments between each vertex parametrically (with the parameter t) and summing the integrals over each line segment.

$$\begin{aligned} x_i(t) &= x_i + (x_{i+1} - x_i)t, \\ y_i(t) &= y_i + (y_{i+1} - y_i)t, \end{aligned} \qquad 0 \le t \le 1,\ i = 1, \cdots, n$$

then,

$$\begin{aligned} \mu_x &= \frac{1}{2}\sum_{i=1}^{n}\left[\int_0^1 x_i^2(t)\, dy_i(t)\right] \\ &= \frac{1}{2}\sum_{i=1}^{n}\left[\int_0^1 (x_i + (x_{i+1} - x_i)t)^2 (y_{i+1} - y_i)\, dt\right] \\ &= \frac{1}{6}\sum_{i=1}^{n}(y_{i+1} + y_i)\cdot a_i. \end{aligned}$$

The moment μ_y can be obtained similarly. The centroid $(\bar{x}, \bar{y})$ is then transformed to 3D coordinates as by equation (2.1) in Section 2.2.

4.2.3 Resampling Contours

The outlined points are first transformed from Cartesian coordinates to polar coordinates with the centroid of the contour as the origin of the 2D polar coordinate system.

$$\begin{aligned} r_i &= \sqrt{(x_i - \bar{x})^2 + (y_i - \bar{y})^2}, \\ \theta_i &= \tan^{-1}\left(\frac{y_i - \bar{y}}{x_i - \bar{x}}\right), \end{aligned} \qquad i = 1, \cdots, n$$

Then, the contour is resampled at every Θ (= 15°) into N (= 24) points by interpolating r_i as linear function of θ_i. The sampled points $(\tilde{r}_i, \tilde{\theta}_i)$ are given by

$$\tilde{r}_i = \frac{r_{j+1} - r_j}{\theta_{j+1} - \theta_j}\left(\tilde{\theta}_i - \theta_j\right) + r_j, \quad \tilde{\theta}_i = i\Theta \in \left[\theta_j, \theta_{j+1}\right] \text{ and } i = 1, \cdots, N$$

The sampled points are then transformed back to Cartesian coordinates $(\tilde{x}_i, \tilde{y}_i)$ by

$$\begin{aligned} \tilde{x}_i &= \tilde{r}_i \cos\tilde{\theta}_i + \bar{x}, \\ \tilde{y}_i &= \tilde{r}_i \sin\tilde{\theta}_i + \bar{y}, \end{aligned} \qquad i = 1, \cdots, N$$

Finally, $(\tilde{x}_i, \tilde{y}_i)$ are transformed to 3D coordinates as described in Section 2.2.

4.2.4 Rearranging Centroid-links

Assume there are a total of M contours in the stomach compartment being processed, thus there are M corresponding centroids c_i, $i = 1, \cdots, M$. We would like to properly link all the centroids to construct a central wire which represents the trend of the wires on the surface wireframe. Since the contours may intersect one another, as described in Section 1.5, the centroids may be also out of order and need to be sorted first. The proximal stomach consists of approximately parallel contours, and it usually does not require sorting. Thus, we mainly focus on the sorting of the distal stomach in this section.

Sorting involves the comparison among elements, and the goal is to arrange the elements in a desired sequence. We compare points based on the vector dot-product method described in Section 4.1, and negative dot-product value means that the two points under comparison are not in a desired sequence. Thus, regular sorting methods can be modified by replacing the comparison part of the algorithms with the dot-product criterion. There are many methods for sorting numbers [81]. The bubble sort was chosen, because it is easy to implement. Also, because the number of points to be sorted is small, other more complicated sorting methods may be less efficient.

The bubble sort is briefly reviewed as follows. Assume there is an array of M elements a_i, $i = 1, \cdots, M$. The elements of the array are initially in haphazard order, and we would like to sort them in ascending order, i.e. $a_{i-1} < a_i$, $i = 2, \cdots, M$. The pseudocode for the bubble sort method is:

```
for j = M to 2 do begin
    for i = 2 to j do begin
        if a_{i-1} > a_i then exchange a_{i-1} and a_i;
    end;
end;
```

The outer loop (index j) controls the range of the comparisons for the inner loop (index i), and the range decreases by one in each successive pass. The inner loop sequentially compares pairs of adjacent elements within the range, and exchanges the elements if necessary. The last element a_M is guaranteed to be the maximum element after the first pass, and a_{M-1} is the second largest element after the second pass, and so on. The array is sorted when no exchange is required during a pass.

Initially, the centroid points are either already sorted or almost sorted as illustrated in Figure 4.3(a). Because the stomach images were always acquired sequentially from left to right along the abdomen surface, the middle contour was always somewhere near the middle portion of the compartment. Based on these observations, two reference axes (dashed lines in Figure 4.3) are derived to serve as an initial rough estimation of the central wire. (Due to the curvature of the distal stomach, it is sometimes inadequate to use only one reference axis.) Empirically, the first axis starts from the first centroid c_1, and ends at $\lceil \frac{M}{2} \rceil$'th centroid which is designated by c_c. The second axis starts from the c_c, and ends at the last centroid c_M. The first half of the links are sorted by applying the dot-product with the first reference axis $\overline{c_1 c_c}$; the second half of the links use the second reference axis $\overline{c_c c_M}$. Note that the purpose of reference axes is to provide a rough initial approximation of orientation, so it is tolerable to have intersecting contours or out-of-sequence centroids around either end or the middle portion of the stomach.

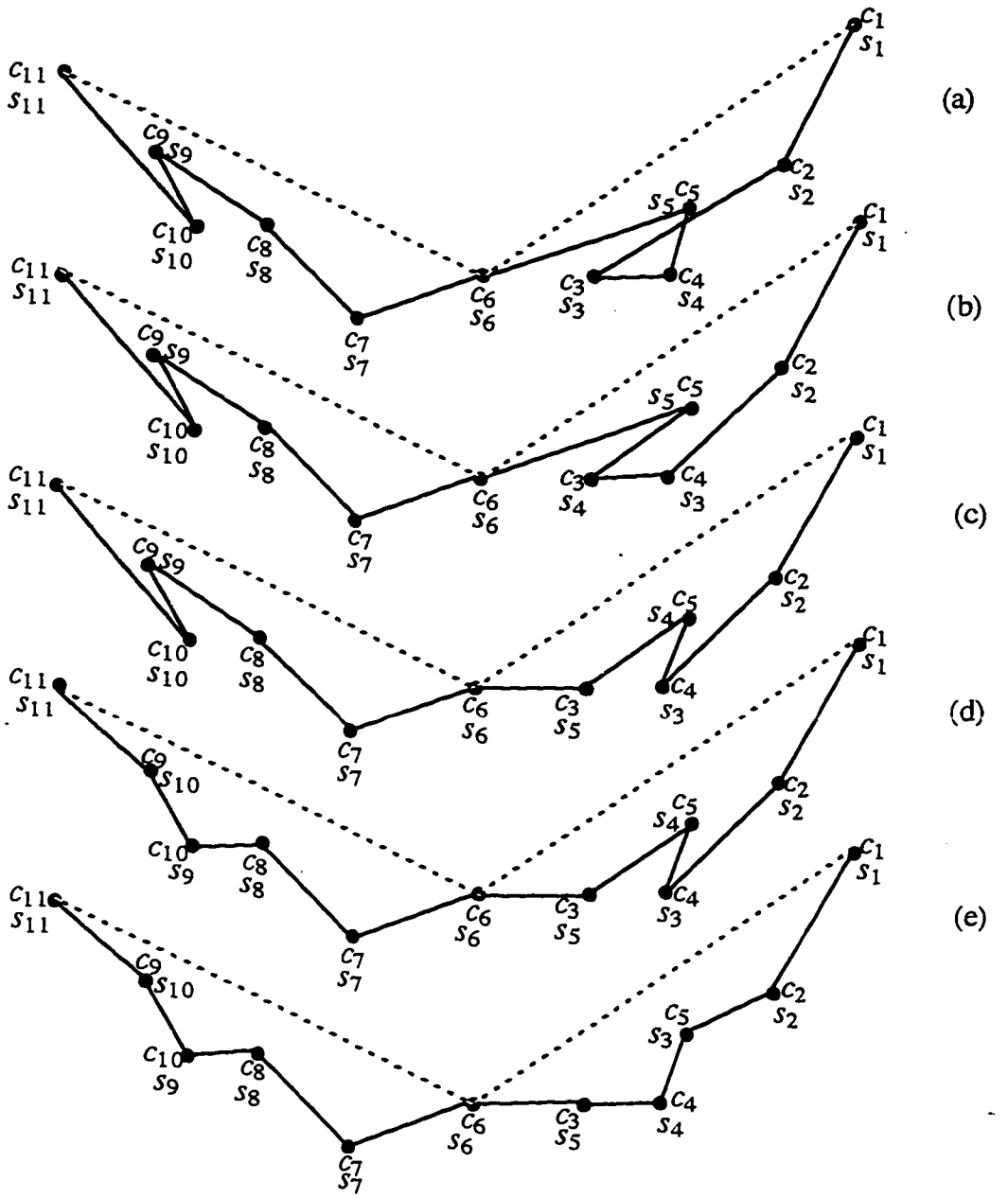

Figure 4.3 Sorting centroid links using the dot-product based bubble sort. Solid lines: centroid links; dashed lines: reference axes. Links before c_6 use axis $\overline{c_1 c_6}$; links after c_6 use axis $\overline{c_6 c_{11}}$. (a) initial links; (b) after pass 1, step 3, swap s_3 and s_4; (c) after pass 1, step 4, swap s_4 and s_5; (d) after pass 1, step 9, swap s_9 and s_{10}; (e) after pass 2, step 3, swap s_3 and s_4.

An array of M points, $s_i, i = 1, \cdots, M$, is used to keep the order of the centroid points during sorting. The central wire is the union of all the links formed by connecting adjacent centroids in that array, i.e. central wire $\triangleq \bigcup_{i=1}^{M-1} \overline{s_i s_{i+1}}$, which is depicted in solid lines in Figure 4.3. The array is initialized with the original ultrasound scan order, i.e. $s_i = c_i$, for all i, and unsorted adjacent points are subject to be exchanged during each pass of the sorting. The pseudocode for the dot-product based bubble sort is as follows.

for $i = 1$ **to** M **do begin**
    $s_i = c_i$;
end;
for $j = M$ **to** 2 **do begin**
    for $i = 2$ **to** j **do begin**
        if $(i - 1) < \lceil \frac{M}{2} \rceil$ **then**
            if $\overline{c_1 c_c} \cdot \overline{s_{i-1} s_i} < 0$ **then** exchange s_{i-1} and s_i;
        else
            if $\overline{c_c c_M} \cdot \overline{s_{i-1} s_i} < 0$ **then** exchange s_{i-1} and s_i;
    end;
end;

The first three lines of code is initialization, and the rest of code is similar to the bubble sort reviewed earlier. The direct comparison between two values in the regular bubble sort is replaced with the vector dot-product here. We also check whether to use either reference axis $\overline{c_1 c_c}$ or $\overline{c_c c_M}$. Figure 4.3 illustrates an example case of the sorting of centroid points; $\{c_3, c_4, c_5\}$ and $\{c_9, c_{10}\}$ are initially out of sequence. The pair $\{c_9, c_{10}\}$ are sorted after the first pass of the outer loop, and centroid $\{c_3, c_4, c_5\}$ are sorted after the second pass.

To facilitate later presentation, sorted centroid links are also denoted as link vectors $\mathbf{l}_i$,

$$\mathbf{l}_i \triangleq \overline{s_i s_{i+1}}, \quad i = 1, \cdots, M-1$$

as shown in Figure 4.4(a). When processing data from *in-vivo* scans, it is not unusual for the adjacent link vectors to have somewhat large differences in orientation, which makes the central wire look jagged. Thus, the link vectors are combined within each 3-neighborhood to generate a set of smoother vectors called trend vectors $\mathbf{t}_i$:

$$\mathbf{t}_i = \mathbf{l}_{i-1} + \mathbf{l}_i + \mathbf{l}_{i+1}, \quad i = 1, \cdots, M-1, \quad (\mathbf{l}_0 \triangleq \mathbf{l}_M \triangleq \mathbf{0})$$

$$\mathbf{t}_M \triangleq \mathbf{t}_{M-1}$$

as shown in Figure 4.4 (b). The last trend vector is equal to the second last one by definition, so that there is one trend vector associated with each centroid. The trend vectors will be the reference vectors used for rearranging wireframe links in the next section. Figure 4.4 (c) and (d) are the normalized link vectors and trend vectors in Figure 4.4 (a) and (b), respectively. The normalized vectors are presented only to demonstrate the smoothing effect, e.g. compare $\mathbf{l}_3$ with $\mathbf{t}_3$ and $\mathbf{l}_8$ with $\mathbf{t}_8$. Vectors do not have to be normalized in the process of the dot-product based sorting, because vectors of different lengths generate the same positive/negative sign in the dot-product operation.

Many factors may contribute to the jaggedness of the central wire: (1) oblique contours between adjacent contours (Note that stomach is not a perfect cylindrical shape.), (2) stomach contraction, (3) patient respiration and body movement, (4) 3D position and orientation measurement error from the POM device, (5) the error of stomach border identification during manual outlining.

Smoothing the jaggedness of the vectors within each K-neighborhood is equivalent to filter out the high frequency noise by convolving the sampled signal with a uniform K-width window (or kernel) in the terminology of digital signal processing [83]. Assume $\mathbf{v}_i, i = 1, \cdots, K$ are the vectors within a K-neighborhood, and $\mathbf{n}_i = \frac{\mathbf{v}_i}{|\mathbf{v}_i|}$ are their normalized vectors which also describes the orientation of the vectors. The question arises: is the summation of orientation $\sum_{i=1}^{K} \mathbf{n}_i$ better than the summation of vectors $\sum_{i=1}^{K} \mathbf{v}_i$ for representing the trend of the vectors within the K-neighborhood?

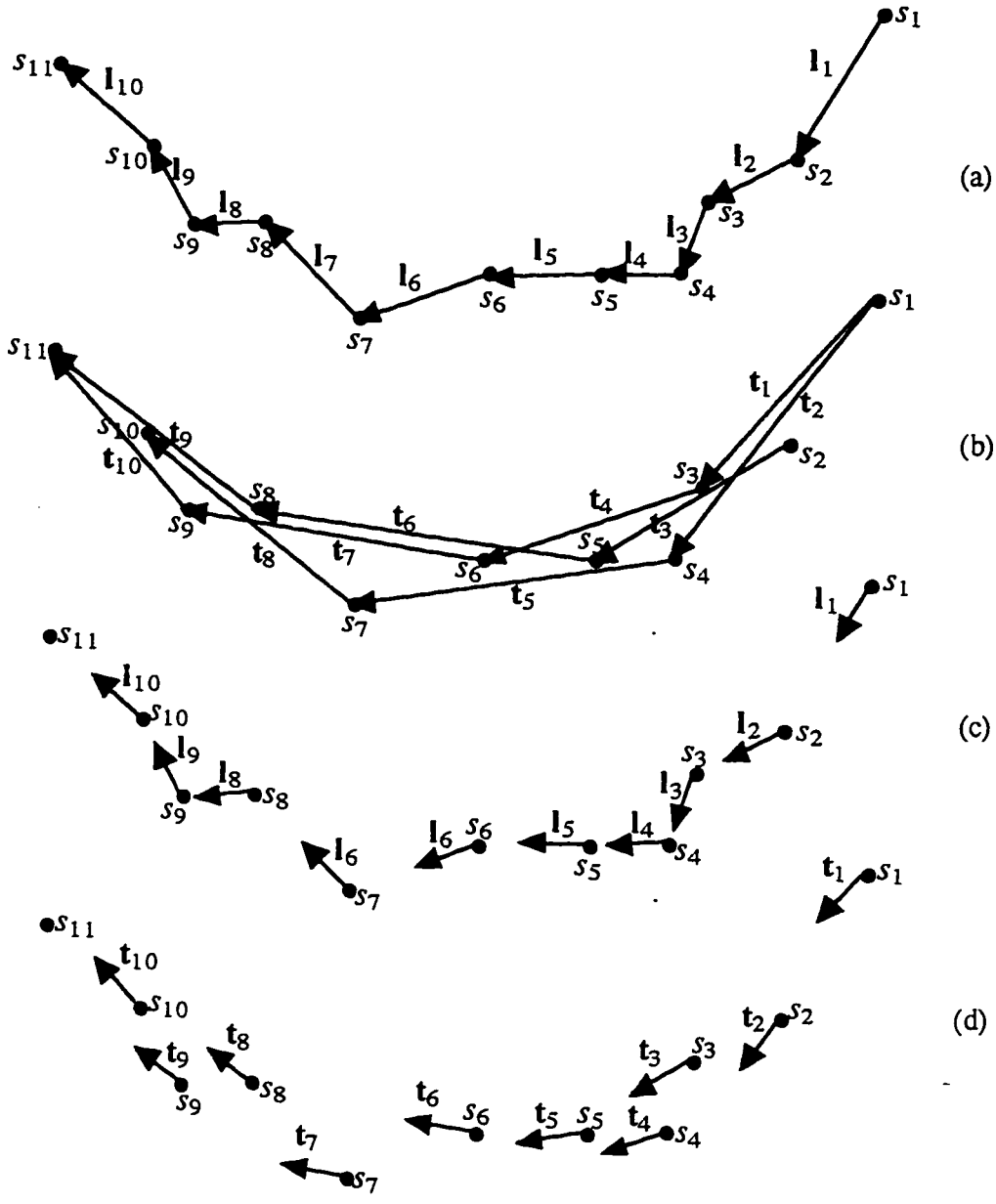

Figure 4.4 Centroid-link and trend vectors. (a) link vectors, (b) trend vectors, e.g. $\mathbf{t}_3 = \mathbf{l}_2 + \mathbf{l}_3 + \mathbf{l}_4$, (c) normalized link vectors, (d) normalized trend vectors.

The answer is no, and the following identity provides the clue as to why this is true.

$$\sum_{i=1}^{K} \mathbf{v}_i = \sum_{i=1}^{K} |\mathbf{v}_i| \mathbf{n}_i$$

The left side of the equation is the summation of the vectors within the K-neighborhood, by which the trend vectors are computed. This is equivalent to the convolution between the vectors and a K-width window with all unity coefficients. The right hand side is the weighted sum of the vectors' orientation, which is equivalent to the convolution between the vectors' orientation and a K-width window with the coefficients adaptive to the length of the vectors. Thus, the summation of vectors $\sum_{i=1}^{K} \mathbf{v}_i$ is an adaptive version of the summation of orientation $\sum_{i=1}^{K} \mathbf{n}_i$. Assuming the same amount of error due to the factors 1 - 5 mentioned above for the centroid locations, a shorter vector generally has larger orientation error than a longer one does. In another words, shorter vectors are more subject to orientation variability; longer vectors carry more meaningful information about the stomach axis orientation.

The optimal width (K) of the K-neighborhood depends on the nature of the signal (stomach shape) and noise (jaggedness). Summation over a wider neighborhood filters out more noise, but at the price of degrading (smearing) the signal. Empirically, $K = 3$ was chosen in all the stomach data sets in this study.

4.2.5 Rearranging Wireframe Links

Recall from Section 4.2.3 that each contour was resampled into N points, and from Section 4.2.4 that there are M contours. Thus, there are total $N \cdot M$ points, p_{ij}, $i = 1, \cdots, N$ and $j = 1, \cdots, M$. Wireframe wires are the union of all the links formed by connecting corresponding points from adjacent contours, i.e. i'th wire $\triangleq \bigcup_{j=1}^{M-1} \overline{p_{ij} p_{i(j+1)}}$, $i = 1, \cdots, N$. Because of possible intersecting contours, the links in each wire may be out of sequence and need to be rearranged.

Basically, the method for link sorting is similar to the dot-product based bubble sort of the centroids in the previous section. The differences are that the role of the reference axes is replaced by the centroid trend vectors, and we are sorting the wireframe links one by one instead of the central wire. The pseudocode is as follows.

```
for k = 1 to N do begin
    for j = M to 2 do begin
        for i = 2 to j do begin
            if t_α · p_{k(i-1)}p_{ki} < 0 then exchange p_{k(i-1)} and p_{ki};
        end;
    end;
end;
```

Each pass of the outermost loop (index k) sorts one wireframe wire. The inner two loops are similar to the bubble sort in the previous section. The trend vector $\mathbf{t}_\alpha$ is the vector associated with the nearest sorted centroid to the midpoint between $p_{k(i-1)}$ and p_{ki}. In mathematical terms, α is defined as $\alpha \in \{1,\cdots,M\}$ and

$$\left| s_\alpha - \frac{p_{k(i-1)} + p_{ki}}{2} \right| \le \left| s_\beta - \frac{p_{k(i-1)} + p_{ki}}{2} \right|, \quad \forall \beta \in \{1,\cdots,M\}.$$

4.2.6 Volume Computation

Since all $N \cdot M$ points, p_{ij}, $i = 1,\cdots,N$ and $j = 1,\cdots,M$, have been sorted in the previous section, the surface wireframe can be readily constructed by connecting points which are adjacent in terms of indexes i and j. The wireframe consists of $N(M-1)$ quadrilaterals, $p_{ij}p_{i(j+1)}p_{(i+1)(j+1)}p_{(i+1)j}$, $i = 1,\cdots,N$, and $j = 1,\cdots,M-1$. To make planar tiles, each quadrilateral is split into two triangles $p_{ij}p_{i(j+1)}p_{(i+1)(j+1)}$ and $p_{ij}p_{(i+1)(j+1)}p_{(i+1)j}$, as shown in Figure 4.5.

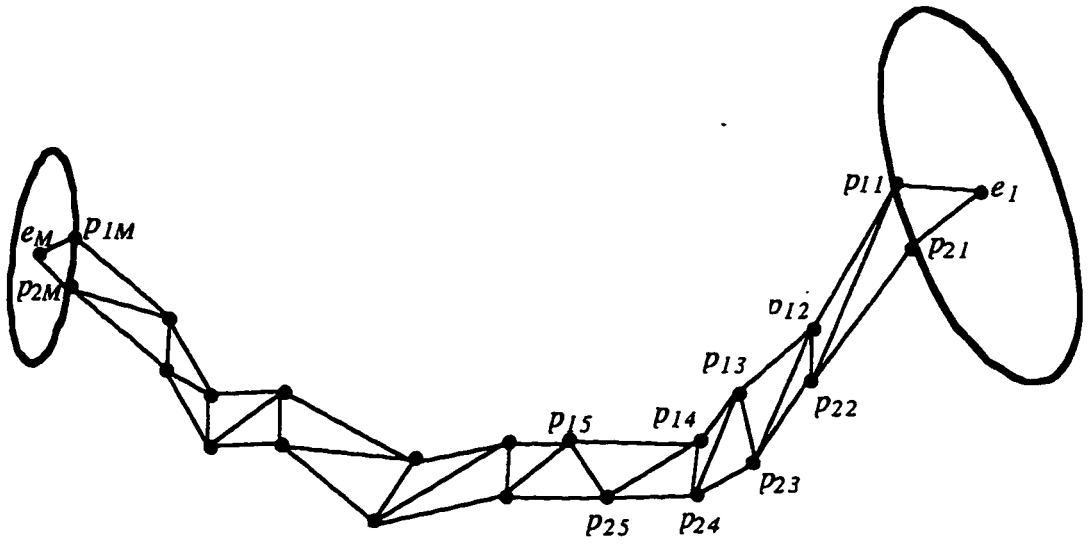

Figure 4.5 Triangle tiles from wireframe wires. Only the first two wires are shown.

The triangle tiles on both ends of the surface are built in a different way. First, the centroids, e_1 and e_M, of the first points and the last points from all the wireframe wires are computed as

$$e_1 = \frac{\sum_{i=1}^{N} p_{i1}}{N}, \quad \text{and} \quad e_M = \frac{\sum_{i=1}^{N} p_{iM}}{N}.$$

The moment based method for computing the centroid in Section 4.2.2 cannot be used here, because the end points on the wires are not co-planar when there are intersecting contours. However, the mean of the x, y, and z coordinates of the vertexes is still a reasonable approximation, because the wireframe points are even samples along each contour. With each centroid as the common vertex, there are total $2N$ triangle tiles on both ends, $e_1 p_{i1} p_{(i+1)1}$ and $e_M p_{(i+1)M} p_{iM}$, $i = 1, \cdots, N$. Note that the vertices of all the triangles are arranged in the same orientation scheme, so that the normal vectors of all the planar tiles point consistently either outwards or inwards. Figure 4.5 also shows the triangle tiles on both ends.

Because the entire surface has been reconstructed with triangle tiles, the Gauss theorem based method presented in Section 3.1, equation (3.5), can be applied to compute the volume. The results of testing the algorithm presented in this chapter are given in Chapter 7.

Chapter 5
Computing Stomach Volume with Volumetric Deformation Method

5.1 Overview

The dot-product method in Chapter 4 relies on the central wire to sort the wireframe links, and basically it requires that the surface, along the lengthwise direction, approximately follow the direction of the central wire. However, this may be not the case for a diseased stomach, which may have a quite different shape from a normal stomach [8]. This prompts us to develop an alternate method to deal with some possible pathological shapes in the future.

The worst scenario is to sort the wireframe links manually. A possible way to do this is to allow the user to examine the links by rotating and zooming the wireframe on a computer display. Through user interface widgets, such as slide bars, dials, or buttons, the user could highlight a specific wire and a specific link in the wire. If the link is out of sequence, the order of the two points of the link could be exchanged. Because every wire needs to be examined, this process would be very tedious and time consuming, and as a result, likely be prone to human error.

A typical clinical examination for gastric emptying requires several scans at fixed intervals after food ingestion. Because the size and shape of the stomach changes gradually from one scan to the next, one strategy is to manually sort the wireframes for the first stomach scan, and then deform it to approximate the wireframes of the subsequent scans. Thus, subsequent volumes of the stomach could be approximated by computing the volumes of deformed wireframes. The Gauss theorem based volume computation process described in Section 4.2.6 could be used.

The basic concept of the deformation method has been reviewed in Section 3.2. A template wireframe is pulled toward target data points by imaginary spring forces under the constraints of maintaining the integrity of the template. Thus, the deformed stomach is called the *template stomach*, and the approximated stomach is called the *target stomach*.

The algorithm was programmed with C language *, and integrated with Application Visualization System software package, version 5.01 (Advanced Visual Systems Inc., Waltham, Massachusetts, USA) running on a DEC Alpha 3000 - 300 workstation. The Application Visualization System was used mainly to provide the user interface, such as file browsers, slide bars, dials, buttons, and the displays of both 2D images and 3D geometry.

5.2 Background on Deformation

Deformation is the alteration of forms or shapes through the geometric transformation of spatial elements which can be pixels (2D image), voxels (3D image), or ideal points (2D or 3D). It is traditionally called image warping when the domain of interests is a 2D image. A geometric transformation is an operation that redefines the locations of spatial elements. It can be a forward transformation $\mathbf{F}() \equiv \langle f_1(), f_2() \rangle$, such as

$$\begin{aligned} x' &= f_1(x, y) \\ y' &= f_2(x, y) \end{aligned} \tag{5.1a}$$

or it can be a backward transformation $\mathbf{G}() \equiv \langle g_1(), g_2() \rangle$, such as

$$\begin{aligned} x &= g_1(x', y') \\ y &= g_2(x', y') \end{aligned} \tag{5.1b}$$

where (x, y) is the source coordinates of spatial elements, (x', y') is the corresponding destination coordinates, and the transformation functions $\mathbf{F}()$ and $\mathbf{G}()$ are inverse functions of each other. The conversion from one transformation to the other is usually not straightforward, unless the transformation is a linear (first-order polynomial) function which accounts for rigid (translation, rotation, and scale) and affine transformations.

---

* The source code can be obtained by contacting the author through email: jong@u.washington.edu.

One of the earliest applications of image warping was remote sensing, which involved aligning multiple images of the same area acquired from satellites at different times. Image warping was a required preprocessing step to correct for image distortions from different sensors and viewing geometries. The geometric transformations used in this type of image warping are usually second-order polynomials [84].

Instead of using image warping as a tool for correcting distortions, modern computer graphics applies various deformation methods to generate special visual effects for filmmaking. The geometric transformations related to this type of application usually emphasizes the speed of the algorithm and the interactive user interface rather than the precision of transformation. The monograph by Wolberg [85] has a complete treatment on this subject, and there are commercial software packages as well, e.g. Elastic Reality (ASDG Corporation, Madison, WI, USA) and Morph (Gryphon Software Corporation, San Diego, CA, USA).

Recently, the field of medical imaging has shown great interest in aligning data sets from different imaging modalities, such as X-ray CT, MRI, PET, ultrasound, or even histology to combine merits from different modalities [86-89]. There are also interests in aligning data sets from the same modality acquired at different stages of disease for inter- and intra-patient comparisons [90, 91]. Because the resolution and distortion are different in every imaging modality and the tissue often changes in size and shape with time, various deformation methods are playing important roles in this growing field. Due to the complexity of human tissue structure and image formation processes, it is very challenging to design a perfect geometric transformation. Usually, tissue is modeled as an elastic material, and splines are introduced in the geometric transformation. The work described in this chapter is a variation on deformation-based alignment methods for approximating the surface and computing the volume of stomach.

Our approach is based on the free-form deformation (FFD) method developed originally by Sederberg, et al. [92]. It describes the warping or displacement of points embedded in 3D space by using volumetric 3D splines. Many properties of FFD are more easily understood in a lower dimension, so I will first introduce the parametric forms of a line segment and Bezier curve in 2D space with the emphasis on using control points to reshape the line and curve.

A line segment with end points at $p_0(x_0, y_0)$ and $p_1(x_1, y_1)$, as shown in Figure 5.1(a), can be represented by the trajectory of a moving point $p(t)$ or $p(x, y)$:

$$p(t) = Q_0(t) \cdot p_0 + Q_1(t) \cdot p_1, \qquad 0 \le t \le 1$$
$$\text{where} \begin{cases} Q_0(t) = 1 - t \\ Q_1(t) = t \end{cases}$$

or

$$x = Q_0(t) \cdot x_0 + Q_1(t) \cdot x_1$$
$$y = Q_0(t) \cdot y_0 + Q_1(t) \cdot y_1.$$

The location of moving point $p(t)$ is the weighted sum of the locations of points p_0 and p_1. When $t = 0$ ($Q_0 = 1$, $Q_1 = 0$), $p(t)$ lies at p_0; when $t = 1$ ($Q_0 = 0$, $Q_1 = 1$), $p(t)$ lies at p_1. Since $0 \le t \le 1$ ($Q_0 \ge 0$, $Q_1 \ge 0$, and $Q_0 + Q_1 = 1$, as shown in Figure 5.1(b)), $p(t)$ always lies on the line segment between p_0 and p_1. Points p_0 and p_1 can be regarded as the control points of the line segment, because the trajectory of point $p(t)$ can be controlled by relocating p_0 and p_1.

A Bezier curve is a cubic polynomial curve segment defined by four control points, p_0, p_1, p_2, and p_3, as shown in Figure 5.1(c). The trajectory $p(t)$ is derived from the weighted sum of the four control points:

$$p(t) = \sum_{i=0}^{3} Q_i(t) \cdot p_i, \qquad 0 \le t \le 1$$
$$\text{where} \begin{cases} Q_0(t) = (1-t)^3 \\ Q_1(t) = 3t(1-t)^2 \\ Q_2(t) = 3t^2(1-t) \\ Q_3(t) = t^3 \end{cases}$$

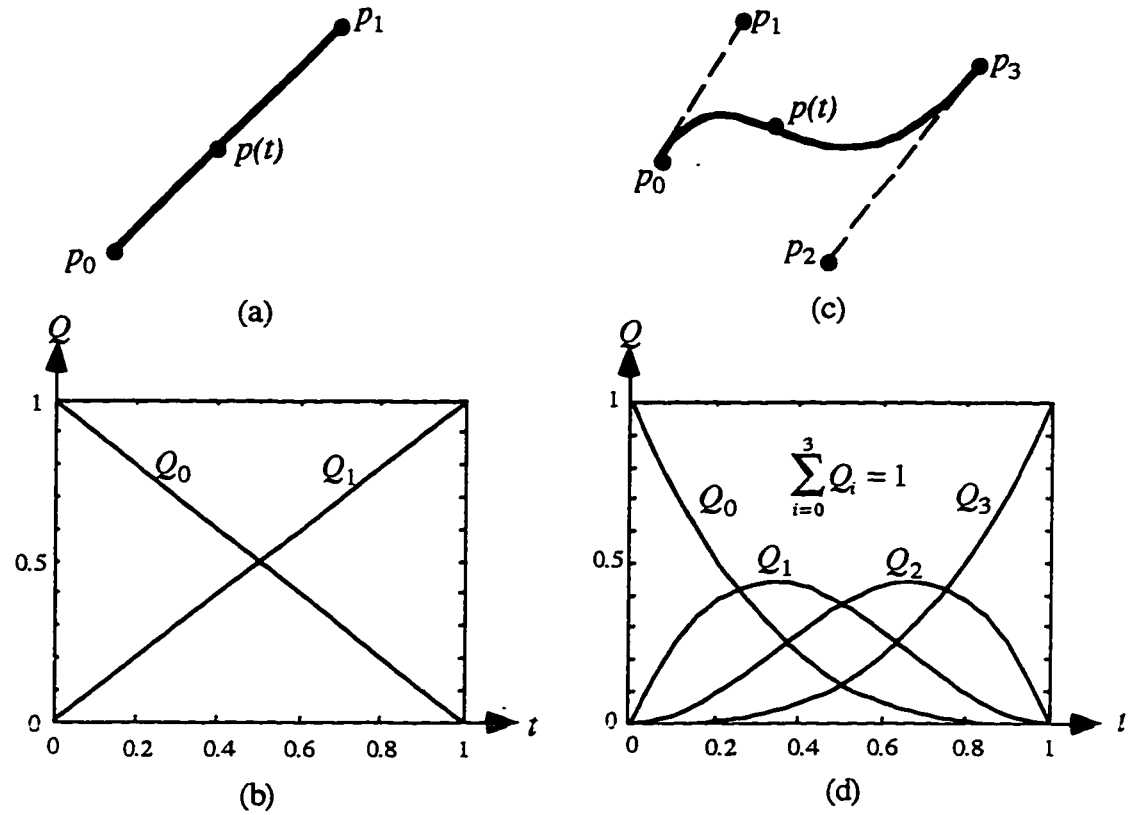

Figure 5.1 Parametric line and Bezier curve. (a) A line segment and its two control points, (b) The weighting functions for the line segment, (c) A Bezier curve segment and its four control points, (d) The weighting functions for the Bezier curve.

The weighting functions (also called blending functions), Q_0, Q_1, Q_2, and Q_3, are plotted in Figure 5.1(d). At $t = 0$, $Q_0 = 1$ and $Q_1 = Q_2 = Q_3 = 0$, so $p(t)$ lies at point p_0. At $t = 1$, $Q_3 = 1$ and $Q_0 = Q_1 = Q_2 = 0$, so $p(t)$ lies at point p_3. The curve does not pass through points p_1 and p_2 except when the control points are collinear. It can be proven [30] that

$$p'(0) = 3(p_1 - p_0)$$
$$p'(1) = 3(p_3 - p_2).$$

Thus, the vectors $\overline{p_0p_1}$ and $\overline{p_2p_3}$ specify the starting and ending tangent vectors of the Bezier curve segment. Figure 5.2 illustrates the deformation of a Bezier curve by moving its control points. Note that the sum of the four blending functions is everywhere unity and each weighting function is everywhere nonnegative for $0 \le t \le 1$, which means the curve segment is completely contained in the convex hull of the four control points. The convex hull for 2D curves is the convex polygon formed by the four control points. In general, the weighted average of n points falls within the convex hull of the n points, if the blending functions are nonnegative and sum to one [30].

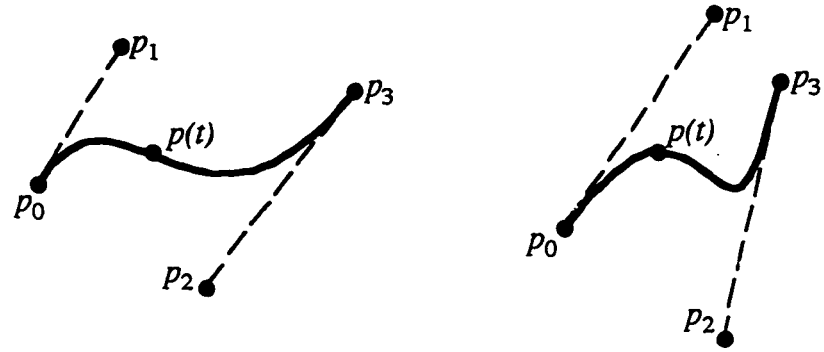

Figure 5.2 The Bezier curve in (a) is deformed to that in (b) by moving the control points, p_1, p_2, p_3, and p_4.

The Bernstein polynomials are the most commonly used blending functions, which have the form

$$Q_{n,i}(t) = \binom{n}{i} t^i (1-t)^{n-i}, \qquad 0 \le t \le 1$$

where $\binom{n}{i} = \frac{n!}{i!(n-i)!}$. The four blending functions used in Bezier curve are actually a special case of the Bernstein polynomials by setting $n = 3$ and $i = 0,1,2,3$. The Bernstein polynomials have the convex-hull property of $\sum_{i=0}^{n} Q_{n,i}(t) = 1$ and $0 \le Q_{n,i} \le 1$ for all i's [30]. Figure 5.3 plots the Bernstein polynomials for $n = 5$.

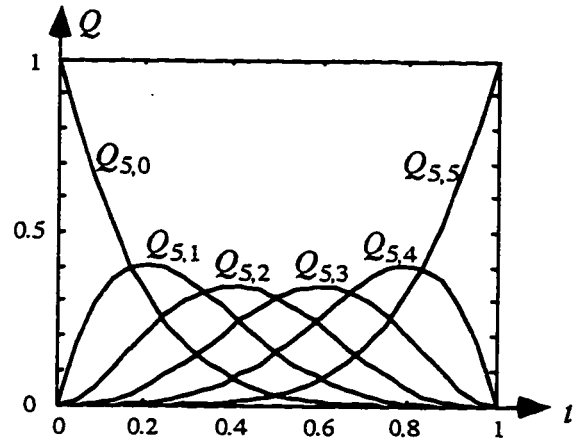

Figure 5.3 Bernstein polynomials for $n = 5$.

The Bezier curve has only one degree of freedom in the parameter space ($0 \le t \le 1$), so it can be regarded as 1D free-from deformation (FFD). A general 2D FFD based on the Bernstein polynomials can be defined as

$$p(s,t) = \sum_{i=0}^{n}\sum_{j=0}^{m} Q_{n,i}(s) \cdot Q_{m,j}(t) \cdot p_{ij}, \qquad 0 \le s \le 1, 0 \le t \le 1$$

$$\text{where} \begin{cases} Q_{n,i}(s) = \binom{n}{i} s^i (1-s)^{n-i} \\ Q_{m,j}(t) = \binom{m}{j} t^j (1-t)^{m-j} \end{cases} \tag{5.2}$$

The trajectory $p(s,t)$, $0 \le s,t \le 1$, is the weighted sum of $(n+1)\times(m+1)$ control points p_{ij}, $i = 0,\cdots n$ and $j = 0,\cdots,m$. The blending functions are the product of two Bernstein polynomials, one each in the s- and t-parameter spaces: $Q_{n,i}(s) \cdot Q_{m,j}(t)$.

Figure 5.4 plots four representative blending functions for $n = m = 3$. The convex-hull property still holds, because each blending function is between 0 and 1, and

$$\sum_{i=0}^{n}\sum_{j=0}^{m} Q_{n,i}(s)\cdot Q_{m,j}(t)$$

$$= \left(\sum_{i=0}^{n} Q_{n,i}(s)\right)\left(\sum_{j=0}^{m} Q_{m,j}(t)\right) \qquad (5.3)$$

$$= 1.$$

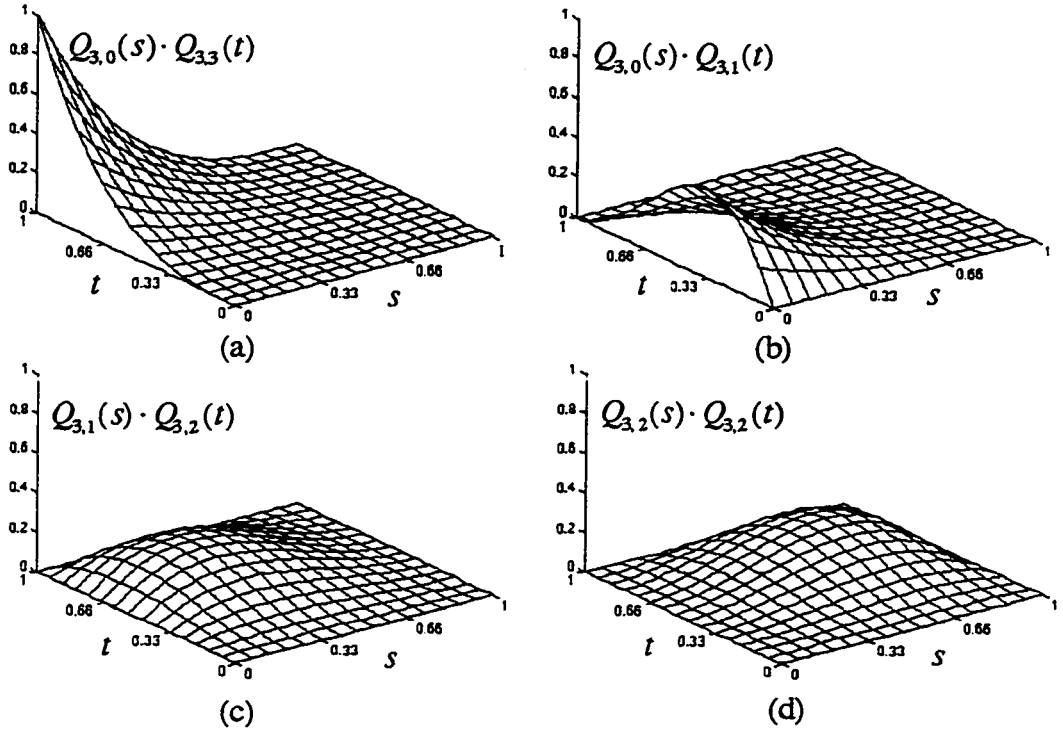

Figure 5.4 Four representative blending functions for the 2D FFD (4x4 grids).

The control points are initially placed at the intersections of regular and evenly spaced grid-lines to cover a rectangular region as shown in Figure 5.5(a). When the control points are arranged in this way, there is an interesting property of in-place mapping, i.e. each point within the rectangular region is mapped to itself. This can be proven as follows. From equation (5.2),

$$
\begin{aligned}
p(s,t) &= \sum_{i=0}^{n}\sum_{j=0}^{m} Q_{n,i}(s)\cdot Q_{m,j}(t)\cdot p_{ij} \\
&= \sum_{i=0}^{n}\sum_{j=0}^{m}\left[Q_{n,i}(s)\cdot Q_{m,j}(t)\right]\left(p_{00}+\frac{i}{n}\overline{p_{00}p_{n0}}+\frac{j}{m}\overline{p_{00}p_{0m}}\right) \\
&= \sum_{i=0}^{n}\sum_{j=0}^{m}\left[Q_{n,i}(s)\cdot Q_{m,j}(t)\right]p_{00}+\left(\sum_{j=0}^{m}Q_{m,j}(t)\right)\left(\sum_{i=0}^{n}\frac{i}{n}\left[Q_{n,i}(s)\right]\right)\overline{p_{00}p_{n0}} \\
&\qquad +\left(\sum_{i=0}^{n}Q_{n,i}(s)\right)\left(\sum_{j=0}^{m}\frac{j}{m}\left[Q_{m,j}(t)\right]\right)\overline{p_{00}p_{0m}} \\
&= p_{00}+\left(\sum_{i=0}^{n}\frac{i}{n}\left[Q_{n,i}(s)\right]\right)\overline{p_{00}p_{n0}}+\left(\sum_{j=0}^{m}\frac{j}{m}\left[Q_{m,j}(t)\right]\right)\overline{p_{00}p_{0m}} \\
&= p_{00}+s\,\overline{p_{00}p_{n0}}+t\,\overline{p_{00}p_{0m}}
\end{aligned}
\qquad (5.4)
$$

In the above derivation, the identity in equation (5.3) is used, and the last step can be induced from $n = m = 3, 4$, etc.* The four corners of the rectangular region are (0,0), (1,0), (0,1), and (1,1) in the (s,t) parametric space, and the control point p_{00} is regarded as the origin of the coordinates. The (s,t) parametric space is also called normalized coordinates, because all the point coordinates within the region are between 0 and 1. Assume the physical size of the rectangular region is $X \cdot Y$, and the physical coordinates of an arbitrary point is (x,y). The following formula converts the physical coordinates to the normalized coordinates.

$$s = \frac{x}{X} \quad \text{and} \quad t = \frac{y}{Y}.$$

The FFD is a forward transformation from the source coordinates to the destination coordinates as represented by equation (5.1a), which can be easily seen by rewriting equation (5.2) in the form of equation (5.1a) as follows.

---

* The case of $n = 3$ is shown here: $\sum_{i=0}^{3}\frac{i}{3}\left[Q_{3,i}(s)\right] = \sum_{i=0}^{3}\frac{i}{3}\left[\binom{3}{i}s^{i}(1-s)^{3-i}\right] = s.$

$$x' = f_1(x,y) = \sum_{i=0}^{n}\sum_{j=0}^{m} Q_{n,i}(\tfrac{x}{X}) \cdot Q_{m,j}(\tfrac{y}{Y}) \cdot x_{ij}$$
$$y' = f_2(x,y) = \sum_{i=0}^{n}\sum_{j=0}^{m} Q_{n,i}(\tfrac{x}{X}) \cdot Q_{m,j}(\tfrac{y}{Y}) \cdot y_{ij} \qquad (5.5)$$

where (x_{ij}, y_{ij}) are the physical coordinates of the control point p_{ij}. The parameters, $\frac{x}{X}$ and $\frac{y}{Y}$, of the Bernstein polynomials on the right side of equation (5.5) indicate that it is more convenient to use the normalized coordinates (s,t) as the source coordinates in the FFD. In contrast, the destination coordinates (x',y') of the FFD are in physical coordinates. Initially, (x',y') is in place with (x,y), which was proven in equation (5.4). This means that there is no deformation to the region, if the control points remain at the grid points, as shown in Figure 5.5(a). From equation (5.5), we can see that (x',y') changes with (x_{ij},y_{ij}). Thus, the region and the figure within the region can be deformed by moving the control points $p_{ij}(x_{ij},y_{ij})$, as shown in Figure 5.5(b).

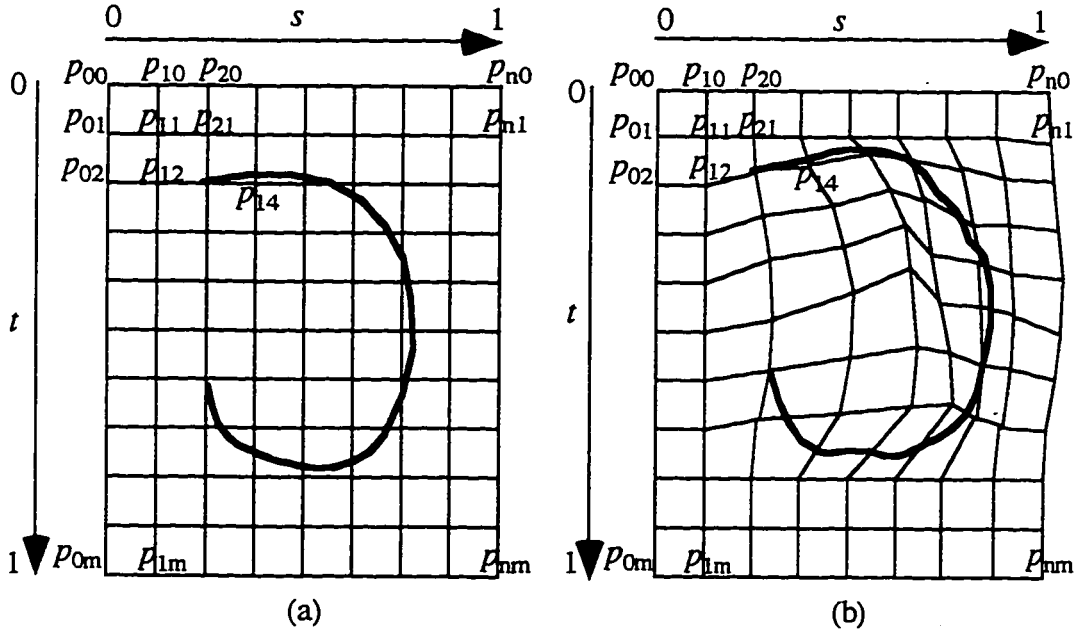

Figure 5.5 A plane can be deformed by relocating the spline control points $(p_{00},\cdots,p_{nm})$ which lie at the intersections of the grid system: (a) before deformation, (b) after deformation, the curve embedded on the plane is also deformed. Some control points in (b) remain at the same positions as in (a), others are moved to different positions, e.g. p_{14} moves northeast.

5.3 Formulation of Surface Matching

As stated in Section 5.1, our goal is to deform the template stomach surface to match the to-be-built surface of the target stomach for approximating its volume. Our approach is based on the FFD described in Section 5.2. Although Szeliski, et al. [79] has reported good results on aligning densely sampled surfaces (laser range data) with a similar approach, no one has applied this method to sparsely sampled data, such as our 3D stomach data from freehand ultrasound scans.

Three dimensional FFD can be formulated in a manner similar to the 2D FFD. The normalized source coordinates, physical source coordinates, and destination coordinates are extended to 3D: (s,t,u), (x,y,z), and (x',y',z'), respectively. The control points $p_{ijk}\,(x_{ijk}, y_{ijk}, z_{ijk})$ are initially placed in a uniform, orthogonal grid within a parallelepiped volume. The volume (and the template stomach within the volume) can then be deformed by moving the control points. The blending functions become the product of three Bernstein polynomials from each dimension. In mathematical terms, 3D FFD with $(n+1) \times (m+1) \times (l+1)$ control points is defined as:

$$p(s,t,u) = \sum_{i=0}^{n}\sum_{j=0}^{m}\sum_{k=0}^{l} Q_{n,i}(s)\cdot Q_{m,j}(t)\cdot Q_{l,k}(u)\cdot p_{ijk}, \qquad 0\le s,t,u\le 1$$

$$\text{where}\begin{cases} Q_{n,i}(s) = \binom{n}{i} s^i (1-s)^{n-i} \\ Q_{m,j}(t) = \binom{m}{j} t^j (1-t)^{m-j} \\ Q_{l,k}(u) = \binom{l}{k} u^k (1-u)^{l-k} \end{cases} \tag{5.6}$$

or

$$\begin{aligned} x' &= f_1(s,t,u) = \sum_{i=0}^{n}\sum_{j=0}^{m}\sum_{k=0}^{l} Q_{n,i}(s)\cdot Q_{m,j}(t)\cdot Q_{l,k}(u)\cdot x_{ijk} \\ y' &= f_2(s,t,u) = \sum_{i=0}^{n}\sum_{j=0}^{m}\sum_{k=0}^{l} Q_{n,i}(s)\cdot Q_{m,j}(t)\cdot Q_{l,k}(u)\cdot y_{ijk} \\ z' &= f_3(s,t,u) = \sum_{i=0}^{n}\sum_{j=0}^{m}\sum_{k=0}^{l} Q_{n,i}(s)\cdot Q_{m,j}(t)\cdot Q_{l,k}(u)\cdot z_{ijk}. \end{aligned} \tag{5.7}$$

The source coordinates of equation (5.7) are in normalized coordinates, and the destination coordinates are in physical coordinates.

It is more convenient to define two shorthand notations **p** and **F**() as follows.

$$\mathbf{p} \equiv \left\{ p_{ijkx}, p_{ijky}, p_{ijkz} \,|\, i = 0,\cdots,n; j = 0,\cdots,m; k = 0,\cdots,l \right\}$$

$\mathbf{F}() \equiv \langle f_1(), f_2(), f_3() \rangle$, where f_1, f_2, and f_3 are defined in equation (5.7).

Assume there are a total of N sampling points in (s,t,u) coordinates on the template stomach surface, $q_i(s_i,t_i,u_i)$, $i = 1,\cdots,N$, and the corresponding positions of these N points in (x',y',z') coordinates after the deformation are $r_i(x_i',y_i',z_i') \equiv \mathbf{F}(q_i;\mathbf{p})$. The object is to find the optimum transformation $\mathbf{F}(;\mathbf{p})$, such that the transformed points r_i all lie as close as possible to the surface of the target stomach. Because the target surface is not yet defined, we use a point-to-point Euclidean distance, and define d_i as the distance between point r_i and the nearest point of the target stomach, i.e.

$$d_i(\mathbf{p}) \equiv \min_{j=1}^{N'} \left\| r_i - g_j \right\| = \min_{j=1}^{N'} \left\| \mathbf{F}(q_i;\mathbf{p}) - g_j \right\| \tag{5.8}$$

where g_j, $j = 1,\cdots,N'$, are all the sampled points on the target surface. There are total N distance terms from each transformed point to the target points, so the problem can be posed as a minimization of the cost function

$$C(\mathbf{p}) = \sum_{h=1}^{N} \left[\frac{d_h(\mathbf{p})}{\sigma_h} \right]^2 + \alpha \cdot R(\mathbf{p}) \tag{5.9}$$

where the subscript index h (instead of i) is used for the clarity and consistency in the future reference, σ_h is a weighting factor for each transformed point, $R(\mathbf{p})$ is a regularization term [93] (or internal energy term as reviewed in Section 3.2) which corresponds to a prior knowledge of the shape of the target surface, and α is the associated weighting factor. The sum of the squared distances between adjacent FFD control points is used as the regularization term, i.e.

$$R(\mathbf{p}) = \sum_{k=0}^{l}\sum_{j=0}^{m}\sum_{i=0}^{n-1}\left\|p_{(i+1)jk} - p_{ijk}\right\|^2 + \sum_{k=0}^{l}\sum_{i=0}^{n}\sum_{j=0}^{m-1}\left\|p_{i(j+1)k} - p_{ijk}\right\|^2 + \sum_{i=0}^{n}\sum_{j=0}^{m}\sum_{k=0}^{l-1}\left\|p_{ij(k+1)} - p_{ijk}\right\|^2. \tag{5.10}$$

Compare Figure 5.5 (a) and (b); $R(\mathbf{p})$ is larger after the deformation. Thus, the regularization term tends to resist deformation during the minimization of the cost function $C(\mathbf{p})$ in equation (5.9). It will be clear later that $R(\mathbf{p})$ is important in stabilizing the algorithm.

The cost function $C(\mathbf{p})$ can be minimized iteratively, which is detailed in the next section. The parameters $\mathbf{p}$ change in every iteration, as do the transformed points $r_i(x_i', y_i', z_i')$ which are equal to $\mathbf{F}(q_i;\mathbf{p})$. Thus, the distance between the transformed points and target points, $d_i(\mathbf{p})$, $i = 1, \cdots, N$, must be computed in every iteration, which is computationally very costly. Since the target points are fixed in space, this problem is overcome by using a pre-computed distance map of the target points. A distance map is a look-up table which takes a transformed point's 3D coordinates (x', y', z') as its entry, and returns the nearest distance to the target points. Assume the distance map $D[x', y', z']$ covers the 3D region $([X_{min}, X_{max}], [Y_{min}, Y_{max}], [Z_{min}, Z_{max}])$, and there are $(N_X + 1)(N_Y + 1)(N_Z + 1)$ lattice of entry points in this region. This means the output from the distance map is quantized in every X_{unit}, Y_{unit}, and Z_{unit} distance, where

$$X_{unit} = \frac{X_{max} - X_{min}}{N_X}, \qquad Y_{unit} = \frac{Y_{max} - Y_{min}}{N_Y}, \qquad Z_{unit} = \frac{Z_{max} - Z_{min}}{N_Z}.$$

Thus the distance is:

$$D[x', y', z'] = \min_{j=1}^{N'}\left\|\left(\left\lfloor\frac{x' - X_{min}}{X_{unit}}\right\rfloor \cdot X_{unit}, \left\lfloor\frac{y' - Y_{min}}{Y_{unit}}\right\rfloor \cdot Y_{unit}, \left\lfloor\frac{z' - Z_{min}}{Z_{unit}}\right\rfloor \cdot Z_{unit}\right) - g_j\right\| \tag{5.11}$$

where $\lfloor\ \rfloor$ is the floor function which generates the largest integer smaller than its parameter (e.g. $\lfloor 2.3 \rfloor = 2$), and g_j and N' are defined in equation (5.8).

Occasionally, extensive patient movement may occur between different data sets being acquired. This requires a global transformation to roughly align the template stomach with the target stomach before applying FFD. We use an affine transformation which preserves parallelism and can be parameterized with 12 degrees of freedom (translation, rotation, scaling, and shearing in each dimension) [30],

$$\begin{bmatrix} x' \\ y' \\ z' \end{bmatrix} = \begin{bmatrix} p_{00} & p_{01} & p_{02} & p_{03} \\ p_{10} & p_{11} & p_{12} & p_{13} \\ p_{20} & p_{21} & p_{22} & p_{23} \end{bmatrix} \begin{bmatrix} 1 \\ x \\ y \\ z \end{bmatrix}$$

or

$$\begin{aligned} x' &= f_1(x,y,z) = p_{00} + p_{01}x + p_{02}y + p_{03}z \\ y' &= f_2(x,y,z) = p_{10} + p_{11}x + p_{12}y + p_{13}z \\ z' &= f_3(x,y,z) = p_{20} + p_{21}x + p_{22}y + p_{23}z \end{aligned} \tag{5.12}$$

where (x, y, z) are the source coordinates and (x', y', z') are the destination coordinates. If we define $\mathbf{p} \equiv \{p_{00}, p_{01}, \cdots, p_{23}\}$, and $d_h(\mathbf{p})$ as the minimum distance from affine-transformed point h to the target points, a cost function similar to equation (5.9) can also be formulated as follows.

$$C(\mathbf{p}) = \sum_{h=1}^{N} \left[\frac{d_h(\mathbf{p})}{\sigma_h} \right]^2. \tag{5.13}$$

5.4 Least Square Minimization

The cost functions $C(\mathbf{p})$ in both equations (5.9) and (5.13) can be iteratively minimized by a standard nonlinear least squares technique called the Levenberg-Marquardt method [94, 95]. When $C(\mathbf{p})$ is sufficiently close to the minimum, the small neighborhood usually can be approximated by the quadratic model (also known as Newton's method) which is obtained from a truncated Taylor series expansion of $C(\mathbf{p})$ about $\mathbf{p}^{(k)}$:

$$C(\mathbf{p}^{(k)} + \delta\mathbf{p}) \approx C(\mathbf{p}^{(k)}) + \mathbf{g}^{(k)^T}\delta\mathbf{p} + \tfrac{1}{2}\delta\mathbf{p}^T\mathbf{G}^{(k)}\delta\mathbf{p} \tag{5.14}$$

where $\mathbf{p}^{(k)}$ is the resulting parameters for iteration k; $\delta\mathbf{p}$ is the increment leading to $\mathbf{p}^{(k+1)}$, i.e. $\mathbf{p}^{(k+1)} = \mathbf{p}^{(k)} + \delta\mathbf{p}^{(k)}$; $\mathbf{g}^{(k)}$ is the gradient vector (first derivative vector) at $\mathbf{p}^{(k)}$, i.e. $\mathbf{g}^{(k)} \equiv \nabla C(\mathbf{p}^{(k)})$; and $\mathbf{G}^{(k)}$ is the Hessian matrix (second derivative matrix) at $\mathbf{p}^{(k)}$, i.e. $\mathbf{G}^{(k)} \equiv \nabla^2 C(\mathbf{p}^{(k)})$. To find $\delta\mathbf{p}^{(k)}$ which minimizes the cost function, we can take the derivative of equation (5.14) with respect to $\delta\mathbf{p}$ and set the derivative equal to zero. This gives

$$\mathbf{G}^{(k)}\delta\mathbf{p} = -\mathbf{g}^{(k)} \tag{5.15}$$

which means $\mathbf{g}^{(k)}$ and $\mathbf{G}^{(k)}$ need to be available at any location, and $\delta\mathbf{p}$ can be obtained by solving a linear system of equations where $\mathbf{G}$ is an $n \times n$ matrix, $\mathbf{g}$ is an $n \times 1$ vector, and n is the number of parameters in $\mathbf{p}$.

When $\mathbf{p}^{(k)}$ is far from the minimum, the quadratic model may be a poor local approximation to the shape of the function. In this case, we can take a step down the gradient using the steepest descent method:

$$\delta\mathbf{p} = \text{constant} \cdot (-\mathbf{g}^{(k)})$$

or

$$\mathbf{I}\,\delta\mathbf{p} = \text{constant} \cdot (-\mathbf{g}^{(k)}) \tag{5.16}$$

where $\mathbf{I}$ is the identity matrix.

The Levenberg-Marquardt method is a blending of the quadratic model and the steepest descent method. If we simply combine equations (5.15) and (5.16), we have

$$(\mathbf{G}^{(k)} + \lambda\mathbf{I})\delta\mathbf{p} = -\mathbf{g}^{(k)} \tag{5.17}$$

where λ is a weighting factor. When $\lambda >> 1$, the steepest descent method dominates; when $\lambda << 1$, the quadratic model dominates. The Levenberg-Marquardt method replaces the diagonal elements (1's) in the identity matrix $\mathbf{I}$ with the diagonal elements of the Hessian matrix $\mathbf{G}$, i.e.

$$(\mathbf{G}^{(k)} + \lambda \cdot \mathrm{diag}(\mathbf{G}^{(k)}))\delta\mathbf{p} = -\mathbf{g}^{(k)}. \tag{5.18}$$

The minimization procedure of the Levenberg-Marquardt method is as follows [94]:

1. Given an initial guess of $\mathbf{p}$, compute $C(\mathbf{p})$.
2. Pick a modest value for λ, e.g. $\lambda = 0.001$.
3. Solve the linear equations (5.18) for $\delta\mathbf{p}$ and evaluate $C(\mathbf{p}+\delta\mathbf{p})$.
4. If $C(\mathbf{p}+\delta\mathbf{p}) \geq C(\mathbf{p})$, increase λ by a factor of 10 and go back to step 3.
5. If $C(\mathbf{p}+\delta\mathbf{p}) < C(\mathbf{p})$, decrease λ by a factor of 10, update the trial solution $\mathbf{p} \leftarrow \mathbf{p}+\delta\mathbf{p}$, and go back to step 3.

We stop the above iteration between step 3, 4, and 5 when $C(\mathbf{p})$ does not decrease by more than 1% for 5 iterations or when the preset maximum number of iterations is reached (e.g. 10 iterations). The linear equations (5.18) is solved by Gauss-Jordan elimination [94, 96], selected for its stability and simplicity.

In each iteration, the first and second derivatives of the cost function are required to assemble linear equation (5.18). Thus, we will focus on deriving the derivatives of $C(\mathbf{p})$ in equations (5.9) and (5.13) for the rest of this section.

For FFD, the first derivative of $C(\mathbf{p})$ in equation (5.9) with respect to the x-coordinate of control point p_{ijk} is

$$\frac{\partial C(\mathbf{p})}{\partial x_{ijk}} = 2\sum_{h=1}^{N}\left[\frac{d_h(\mathbf{p})}{\sigma_h^2}\frac{\partial d_h(\mathbf{p})}{\partial x_{ijk}}\right] + \alpha \cdot \frac{\partial R(\mathbf{p})}{\partial x_{ijk}}. \tag{5.19}$$

The derivatives $\frac{\partial C}{\partial y_{ijk}}$ and $\frac{\partial C}{\partial z_{ijk}}$ are similar to the above equation (replace x with y or z, respectively). Recall from equation (5.8) that $d_h(\mathbf{p})$ is the minimum distance from the transformed point $r_h(x'_h, y'_h, z'_h)$ to the target points. This distance is approximated by the precomputed distance map D given in equation (5.11). Thus,

$$d_h(\mathbf{p}) \approx D[x'_h, y'_h, z'_h]. \tag{5.20}$$

The partial derivative $\frac{\partial d_h(\mathbf{p})}{\partial x_{ijk}}$ can not be computed directly. However, it can be factored using the chain-rule of derivative:

$$\frac{\partial d_h(\mathbf{p})}{\partial x_{ijk}} = \frac{\partial d_h(\mathbf{p})}{\partial x'_h}\frac{\partial x'_h}{\partial x_{ijk}}. \tag{5.21}$$

The first factor $\frac{\partial d_h(\mathbf{p})}{\partial x'_h}$ in equation (5.21) can be evaluated through the finite difference of the distance map:

$$\frac{\partial d_h(\mathbf{p})}{\partial x'_h} \approx \tfrac{1}{2}\left\{D[x'_h+1, y'_h, z'_h] - D[x'_h-1, y'_h, z'_h]\right\}. \tag{5.22}$$

The second factor $\frac{\partial x'_h}{\partial x_{ijk}}$ in equation (5.21) is obtained by taking the derivative of equation (5.7) with respect to x_{ijk}:

$$\frac{\partial x'_h}{\partial x_{ijk}} = Q_{n,i}(s)\cdot Q_{m,j}(t)\cdot Q_{l,k}(u). \tag{5.23}$$

The derivative of the regularization term $\frac{\partial R(\mathbf{p})}{\partial x_{ijk}}$ in equation (5.19) is obtained by taking the derivative of equation (5.10) with respect to x_{ijk}:

$$\frac{\partial R(\mathbf{p})}{\partial x_{ijk}} = \begin{cases} 2(x_{ijk} - x_{(i+1)jk}), & i=0 \\ 2(x_{ijk} - x_{(i-1)jk}), & i=n \\ 2(2x_{ijk} - x_{(i+1)jk} - x_{(i-1)jk}), & \text{otherwise} \end{cases}$$

$$+\begin{cases} 2(x_{ijk} - x_{i(j+1)k}), & j=0 \\ 2(x_{ijk} - x_{i(j-1)k}), & j=m \\ 2(2x_{ijk} - x_{i(j+1)k} - x_{i(j-1)k}), & \text{otherwise} \end{cases}$$

$$+\begin{cases} 2(x_{ijk} - x_{ij(k+1)}), & k = 0 \\ 2(x_{ijk} - x_{ij(k-1)}), & k = l \\ 2(2x_{ijk} - x_{ij(k+1)} - x_{ij(k-1)}), & \text{otherwise.} \end{cases} \tag{5.24}$$

Finally, the first derivative of $C(\mathbf{p})$ in equation (5.19) can be evaluated by combining equations (5.20) to (5.24).

There are six second partial derivatives, $\frac{\partial^2 C}{\partial x \partial x}, \frac{\partial^2 C}{\partial y \partial y}, \frac{\partial^2 C}{\partial z \partial z}, \frac{\partial^2 C}{\partial x \partial y}, \frac{\partial^2 C}{\partial y \partial z}, \frac{\partial^2 C}{\partial z \partial x}$, and their formats are the same, so we will derive $\frac{\partial^2 C}{\partial x \partial y}$ as an example.

$$\begin{aligned} \frac{\partial^2 C(\mathbf{p})}{\partial x_{ijk} \partial y_{uvw}} &= 2\sum_{h=1}^{N} \frac{1}{\sigma_h^2} \left[\frac{\partial d_h(\mathbf{p})}{\partial x_{ijk}} \frac{\partial d_h(\mathbf{p})}{\partial y_{uvw}} + d_h(\mathbf{p}) \frac{\partial^2 d_h(\mathbf{p})}{\partial x_{ijk} \cdot \partial y_{uvw}} \right] + \alpha \cdot \frac{\partial^2 R(\mathbf{p})}{\partial x_{ijk} \partial y_{uvw}} \\ &\approx 2\sum_{h=1}^{N} \frac{1}{\sigma_h^2} \left[\frac{\partial d_h(\mathbf{p})}{\partial x_{ijk}} \frac{\partial d_h(\mathbf{p})}{\partial y_{uvw}} \right] + \alpha \cdot \frac{\partial^2 R(\mathbf{p})}{\partial x_{ijk} \partial y_{uvw}} \end{aligned} \tag{5.25}$$

where $0 \le i,u \le n$; $0 \le j,v \le m$; $0 \le k,w \le l$; and recall from equation (5.7) that there are $(n+1)(m+1)(l+1)$ control points. The two first derivatives $\frac{\partial d_h(\mathbf{p})}{\partial x_{ijk}}$ and $\frac{\partial d_h(\mathbf{p})}{\partial y_{uvw}}$ can be evaluated using the chain-rule procedure, similar to equations (5.21), (5.22) and (5.23). The second derivative of the regularization term $\frac{\partial^2 R(\mathbf{p})}{\partial x_{ijk} \partial y_{uvw}}$ in equation (5.25) is obtained by taking the derivative of equation (5.24) with respect to y_{uvw}, so

$$\frac{\partial^2 R(\mathbf{p})}{\partial x_{ijk} \partial y_{uvw}} = \frac{\partial^2 R(\mathbf{p})}{\partial y_{ijk} \partial z_{uvw}} = \frac{\partial^2 R(\mathbf{p})}{\partial z_{ijk} \partial x_{uvw}} = 0. \tag{5.26}$$

The second derivatives of the regularization term with respect to the same coordinates are as follows.

$$\frac{\partial^2 R(\mathbf{p})}{\partial x_{ijk}\,\partial x_{uvw}} = \frac{\partial^2 R(\mathbf{p})}{\partial y_{ijk}\,\partial y_{uvw}} = \frac{\partial^2 R(\mathbf{p})}{\partial z_{ijk}\,\partial z_{uvw}} = \begin{cases} 2, & i=0 \text{ or } i=n,\ u=i,\ v=j,\ w=k \\ -2, & u=i+1 \text{ or } u=i-1,\ v=j,\ w=k \\ 4, & 0<i<n,\ u=i,\ v=j,\ w=k \\ 0, & \text{otherwise} \end{cases}$$

$$+ \begin{cases} 2, & j=0 \text{ or } j=m,\ u=i,\ v=j,\ w=k \\ -2, & u=i,\ v=j+1 \text{ or } v=j-1,\ w=k \\ 4, & 0<j<m,\ u=i,\ v=j,\ w=k \\ 0, & \text{otherwise} \end{cases}$$

$$+ \begin{cases} 2, & k=0 \text{ or } k=l,\ u=i,\ v=j,\ w=k \\ -2, & u=i,\ v=j,\ w=k+1 \text{ or } w=k-1 \\ 4, & 0<k<l,\ u=i,\ v=j,\ w=k \\ 0, & \text{otherwise.} \end{cases} \qquad (5.27)$$

Thus, the second derivative of $C(\mathbf{p})$ in equation (5.25) can be evaluated by combining equations (5.21), (5.22), (5.23), (5.26), and (5.27). The gradient vector $\mathbf{g}$ and Hessian matrix $\mathbf{G}$ in equation (5.18) are assembled from equations (5.19) and (5.25).

For an affine transformation, the first derivative of $C(\mathbf{p})$ in equation (5.13) is similar to equation (5.19):

$$\frac{\partial C(\mathbf{p})}{\partial p_{ij}} = 2\sum_{h=1}^{N}\left[\frac{d_h(\mathbf{p})}{\sigma_h^2}\frac{\partial d_h(\mathbf{p})}{\partial p_{ij}}\right]. \qquad (5.28)$$

The second derivative is

$$\frac{\partial^2 C(\mathbf{p})}{\partial p_{ij}\partial p_{uv}} \approx 2\sum_{h=1}^{N}\frac{1}{\sigma_h^2}\left[\frac{\partial d_h(\mathbf{p})}{\partial p_{ij}}\frac{\partial d_h(\mathbf{p})}{\partial p_{uv}}\right]. \qquad (5.29)$$

The minimum distance $d_h(\mathbf{p})$ in equation (5.28) can be obtained from the distance map as stated in equation (5.20). The derivative $\frac{\partial d_h}{\partial p_{ij}}$ or $\frac{\partial d_h}{\partial p_{uv}}$ in equations (5.28) and (5.29) can be factored by the chain-rule as follows.

$$\frac{\partial d_k}{\partial p_{0j}} = \frac{\partial d_k}{\partial x'}\frac{\partial x'}{\partial p_{0j}}, \quad \frac{\partial d_k}{\partial p_{1j}} = \frac{\partial d_k}{\partial y'}\frac{\partial y'}{\partial p_{1j}}, \quad \frac{\partial d_k}{\partial p_{2j}} = \frac{\partial d_k}{\partial z'}\frac{\partial z'}{\partial p_{2j}} \tag{5.30}$$

where $\frac{\partial d_k}{\partial x'}$, $\frac{\partial d_k}{\partial y'}$, and $\frac{\partial d_k}{\partial z'}$ can be evaluated through the finite difference of the distance map as shown in equation (5.22), and

$$\frac{\partial x'}{\partial p_{ij}} = \frac{\partial y'}{\partial p_{ij}} = \frac{\partial z'}{\partial p_{ij}} = \begin{cases} 1, & \text{if } j=0 \\ x, & \text{if } j=1 \\ y, & \text{if } j=2 \\ z, & \text{if } j=3 \end{cases} \tag{5.31}$$

For an affine transformation, the gradient vector **g** and Hessian matrix **G** in equation (5.18) are assembled from equations (5.28) and (5.29).

Results of testing the algorithm presented in this chapter are given in Chapter 7.

Chapter 6
Experimental Setup

6.1 Subjects

Sixteen healthy male volunteers among the staff of the University of Washington were recruited to participate in the experiment. The data from two subjects could not be analyzed due to derangement of the position and orientation measurement (POM) data. The included 14 individuals were of median age 35 years (range 26-54 years), weighed 74 ± 8 kg (mean ± SD), and their heights were 178 ± 6 cm. To study intra-individual variability, one healthy male, age 34, weight 72 Kg, height 178 cm was examined on six consecutive weekdays. Informed consent of the subjects was obtained for non-invasive imaging, as approved by the institutional human studies review board.

6.2 Equipment

The 3D ultrasound system consists of a commercial ultrasound scanner (HDI 3000, Advanced Technology Laboratories, Bothell, WA, USA) and a pulsed flux magnetic field position and orientation measurement (POM) system (Miniature Bird Model, Ascension Technology Corp., Burlington, VT, USA). The scanhead used in this study was a 5-3 MHz hand-held phased array HDI scanhead. The POM transmitter was placed behind the examination chair which was made of plastic material. The POM receiver (sensor) was securely attached on the ultrasound scanhead. The scanner and the POM system were interfaced to an image workstation (Image Vue, Nova Microsonics, Mahawa, NJ, USA) for simultaneously digitizing the ultrasound image and recording its corresponding POM sensor position and orientation (the two R-matrices in equation 2.1). All the data were transferred via Ethernet to a UNIX workstation (DEC Alpha 3000 -300) for manual outlining and volume computation. Figure 6.1 shows the configuration of the whole system.

The geometric relationship between the image plane and the POM receiver coordinates (the S-matrix in equation 2.1) cannot be measured directly, because the origin of the receiver coordinates is sealed within the device and not indicated by any external landmarks. The calibration procedure established by Detmer, et al. [56, 57, 97] was followed to simultaneously obtain the parameters in the S-matrix and the 3D ultrasound

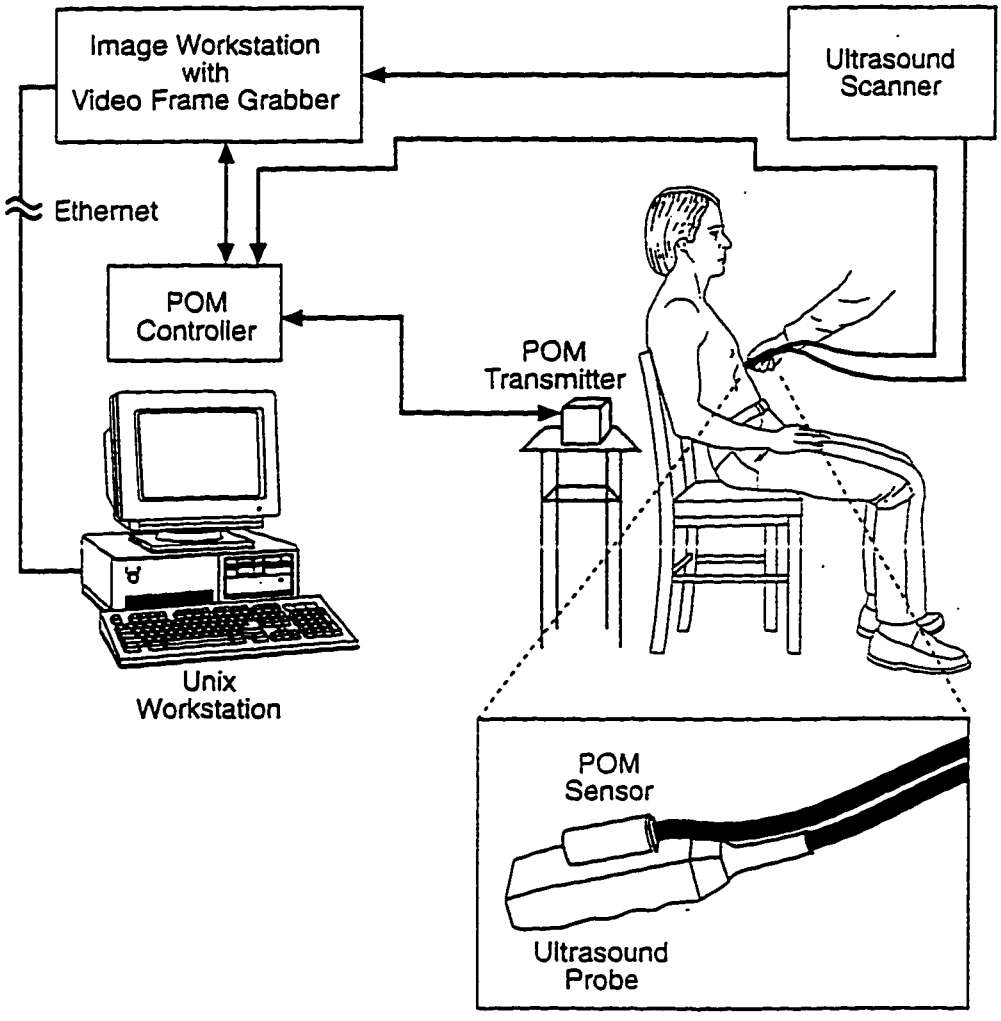

Figure 6.1 The configuration of the 3D ultrasound system based on magnetic position and orientation measurement (POM).

system's precision. A fixed point in a water tank was imaged multiple times from different orientations and distances. With an initial guess of the *S*-matrix $\mathbf{S}^{(0)}$, equation (2.1) was applied to obtain the point's virtual 3D position with respect to the transmitter. The 3D position of the point from every image should be the same in an ideal situation. However, due to the initially inaccurate *S*-matrix and the limited resolution of the ultrasound and POM system, the 3D point positions are scattered within a region. The mean position $\mathbf{p}^{(0)}$ of this region is temporarily regarded as the best estimate of the true 3D position for the fixed point. Then, $\mathbf{p}^{(0)}$ is used to estimate the new *S*-matrix $\mathbf{S}^{(1)}$ which renders (by equation 2.1) a new set of virtual 3D positions with least total squared distance to $\mathbf{p}^{(0)}$. A new mean position $\mathbf{p}^{(1)}$ is then computed from the new set of virtual 3D positions. The position $\mathbf{p}^{(1)}$ is again used to estimate $\mathbf{S}^{(2)}$. This iterative process continues until the total squared distance of all the image points to the mean position converges to a minimum value. The standard deviation of the final 3D point positions gives the RMS error of locating a point target with ultrasound images. This was determined to be 1.71 mm over the system's normal operating range of 50 cm at the time of this study.

6.3 *In-Vitro* Validation

A pig stomach was obtained from a slaughterhouse, thoroughly washed to remove food remnants and debris, and fixed in 20% formalin. The gastric lumen was primed with 1,200 ml of tap water for the first scanning. The stomach was scanned by stepwise acquisition of 2D images starting at the proximal end of the stomach. Subsequently, 100 ml of tap water was added incrementally before the next acquisition took place. The last scanned volume was 1,900 ml.

6.4 Test Meal

A liquid meal of commercial meat broth (Toro clear meat soup, Rieber & Son A/S, Bergen, Norway) containing 1.8 g protein, 0.9 g bovine fat, and 1.1 g carbohydrate (20 Kcal) was ingested by each subject over a period of four minutes. The broth was prewarmed and then cooled to 37° C to reduce the number of air bubbles after ingestion to improve image quality [98].

6.5 Experimental Protocol

All participants in the experiment ingested the broth meal between 8:30 and 10:00 a.m. after an overnight fast. As shown in Figure 6.1, the subjects were scanned while sitting in a plastic chair, leaning slightly backwards at an angle of approximately 120 degrees between the thighs and the spine. The electromagnetic transmitter was positioned close to the back of the volunteer to minimize the distance to the receiver mounted on the scanhead during the examination. On average, this distance was approximately 30 cm. Time zero was defined at start of broth ingestion, and scanning was performed just prior to ingestion, and 5, 10, 15, 20, 25, and 35 minutes post-ingestion. All ultrasound examinations were performed by the same physician (Dr. Odd H. Gilja) [98].

6.6 Data Acquisition

Two investigators were needed to perform the procedure, one to run the image workstation and the other to scan the volunteer. The ultrasound scanner was programmed to the same settings before each examination: Color Map 6, Dynamic Range 45 dB, Persistence medium, and Frame Rate medium. The depth of scanning was adjusted to fit each individual's habitus, averaging 17.6 cm. The angle of the sector image was 80 degrees in all examinations.

The sonographer needed approximately 30 seconds per examination just after the meal to find the optimal starting position for imaging the stomach. Sagittal sections of the stomach were recorded along its entire length, starting in the proximal part where the transducer was positioned by the left subcostal margin and tilted cranially. After stepwise scanning of the proximal stomach from left to the right, the transducer was moved and held to insonicate normally to the skin surface. Then, the distal stomach was scanned stepwise moving distally to the gastroduodenal junction. When gastric contractions were observed, acquisition was paused until the contraction passed. If respiratory movement influenced the observed size of the gastric lumen, images were acquired at points in the respiratory cycle that obtained maximal volumes.

After having digitized one sonogram, the workstation required 5 seconds before the next image could be captured, due to the time required to transfer the image to hard disk. On average, the time spent to scan the total gastric volume was 2 minutes, and 8 ± 2

(fasting) to 17 ± 2 (5 min.) 2D scans were acquired for each examination. All data were analyzed off-line on the Unix workstation. The manual outlining of the stomach boundary was performed by the same physician (Dr. Odd H. Gilja) [98].

Chapter 7
Results

7.1 Dot-product Method

Two examples of wireframe reconstructions of the stomach are shown on the left and right columns of Figure 7.1, respectively. Figures (a) and (b) are the contours of the stomach from manually outlining the stomach boundary on each 2D ultrasound image. Figures (c) and (d) show the wireframes reconstructed by simply linking corresponding points between the adjacent contours in the image acquisition sequence. The center part of the stomach, which contains intersecting contours, has longitudinal zigzag wires, which are corrected in Figures (e) and (f) using the dot-product sorting method described in Chapter 4. The volume of the stomach can be computed by the Gauss theorem based method described in Sections 3.1 and 4.2.6. It takes about one second to perform dot-product sorting, and one second to compute the volume in the UNIX workstation.

The accuracy of the volume computation was first validated with the *in-vitro* pig stomach described in Section 6.6. One example of the reconstructions of the pig stomach in contours, wireframe, and surface rendering is shown in Figure 7.2. The reconstructed volumes agree well with the true volumes in water displacement, as shown in Figure 7.3(a) ($r = 0.999$, SEE = 11.76 ml, and $Y = -5.062 + 1.008 * X$) and Figure 7.3(b) (mean difference = 6.6 ml, standard deviation = 11.0 ml, and all the differences were within the mean $\pm$ two standard deviations over the range of 1200 - 1900 ml). The mean absolute difference between the estimated and true volumes was 0.7%, and the standard deviation was 0.4%.

One sequence of reconstructions of a healthy volunteer's stomach at different time points are shown in contours, wireframes, and surface rendering in Figure 7.4, 7.5, and 7.6, respectively. The gastric emptying of one healthy volunteer over six weekdays is plotted in Figure 7.7(a), and the gastric emptying of 13 healthy volunteers is plotted in Figure 7.7(b). Their corresponding coefficients of variation (= standard deviation / mean) are plotted in Figure 7.7(c). The inter-individual variability is higher than the intra-individual variability, and, in general, both the variabilities increase with emptying time. The average intra-individual gastric emptying from 5 min. to 35 min. is expressed

by Y = 439.996 - 7.887 * X (r = 0.991, SEE = 12.72 ml), and the average inter-individual gastric emptying is expressed by Y = 462.23 - 10.968 * X (r = 0.986, SEE = 22.65 ml). We define the half emptying time $t_{\frac{1}{2}}$ as the half of the vertical intercept (at time 0) divided by the slope, where the vertical intercept and slope come from the linear regression of gastric emptying from 5 min. to 35 min. The average intra-individual $t_{\frac{1}{2}}$ was 29.7 ± 8.1 min., and the average inter-individual $t_{\frac{1}{2}}$ was 21.9 ± 4.5 min.

7.2 Deformation Method

Two examples of alignment between stomachs of different times using the deformation method described in Chapter 5 are shown in Figure 7.8. Since the volume of the proximal stomach is easy to compute and may even become empty in some subjects in latter runs of the experiment, the deformation method was only applied on the distal stomach. Both template stomachs (blue wireframe) in Figure (a) and (b) were acquired after five minutes of meal ingestion, and the target stomachs (red contours) were acquired after 10 minutes. The template stomachs have been reconstructed with the dot-product method, and are deformed to align with the target stomachs in Figure (c) and (d). The volume of the target stomach can be approximated by the volume of the deformed template stomach with the Gauss theorem based method.

The number of FFD control points used was either 4x4x4 or 5x5x5. The default value for the weighting factor α for the regularization term in equation (5.9) was 0.001. The quality of alignment was evaluated by visual inspection of the wireframe and contours, such as those in Figure 7.8, on the computer display. If the alignment was less than satisfactory, the investigator was able to adjust the parameters and perform another alignment. The default value $\alpha = 0.001$ worked well for about 80% of the cases. The regularization term contributes the stiffness in the deformation process. Thus, a smaller α allows higher flexibility for the template stomach. If the template stomach and target stomach have quite different shapes, a smaller α (e.g. 0.0001) should be used. In general, regularization is necessary for stabilizing the algorithm, which is demonstrated in Figure 7.9. Figure (a) shows the original template and target stomachs, Figure (b) shows an alignment without regularization ($\alpha = 0$), and Figure (c) shows an regularized alignment ($\alpha = 0.001$). Each iteration of least square minimization (Levenberg-

Marquardt method) took about 3 seconds and 25 seconds for the 4x4x4 and 5x5x5 FFD, respectively. The maximum number of iterations was set to 10, and the algorithm usually converged within six iterations. The global alignment by affine transformation was much more efficient (less than 1 second per iteration). However, affine alignment was rarely used, because we seldom experienced large patient movement between scans in our experiments.

The deformation method was applied on all the stomachs with intersected contours, and the results are compared with the dot-product method in Figure 7.10. The two methods show excellent agreement ($r = 0.989$, $SEE = 6.086$, and $Y = 3.197 + 0.951 * X$). Compared with the dot-product method, the deformation method under-estimated the volumes by an average of 4.7 ml over the range of 80 - 228 ml, and the limits of agreement ranged from -17.3 ml to 7.9 ml. The mean absolute difference between these two methods was 4.1%, and the standard deviation was 2.8%.

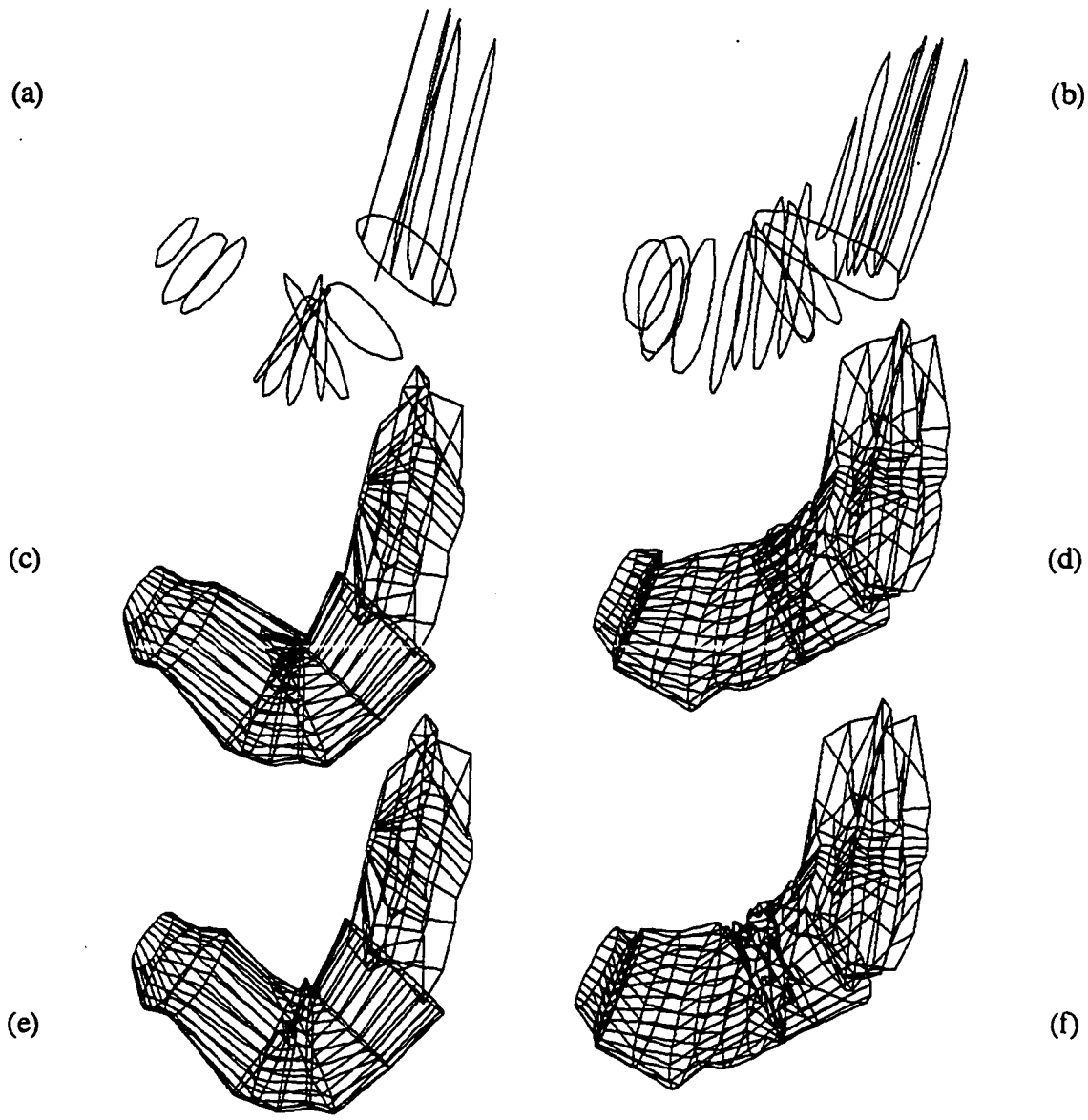

Figure 7.1 Wireframe reconstructions of the stomach using the dot-product sorting method described in Chapter 4. (a)(b) contours; (c)(d) wireframes before sorting; (e)(f) wireframes after sorting. The data in (a), (c), and (e) are from one stomach; and (b), (d), and (f) from another stomach.

(a)

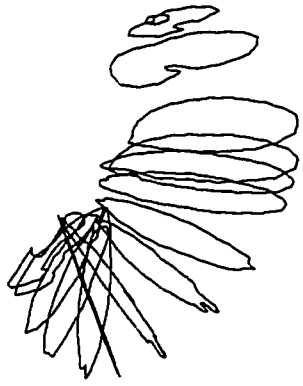

(b)

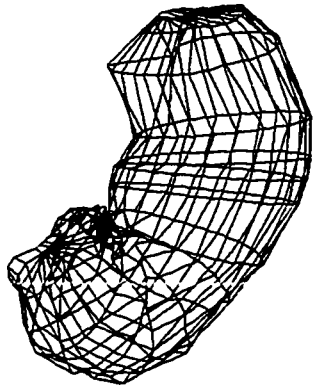

(c)

Figure 7.2 The reconstructions of the *in-vitro* pig stomach in (a) contours, (b) wireframe, and (c) surface rendering.

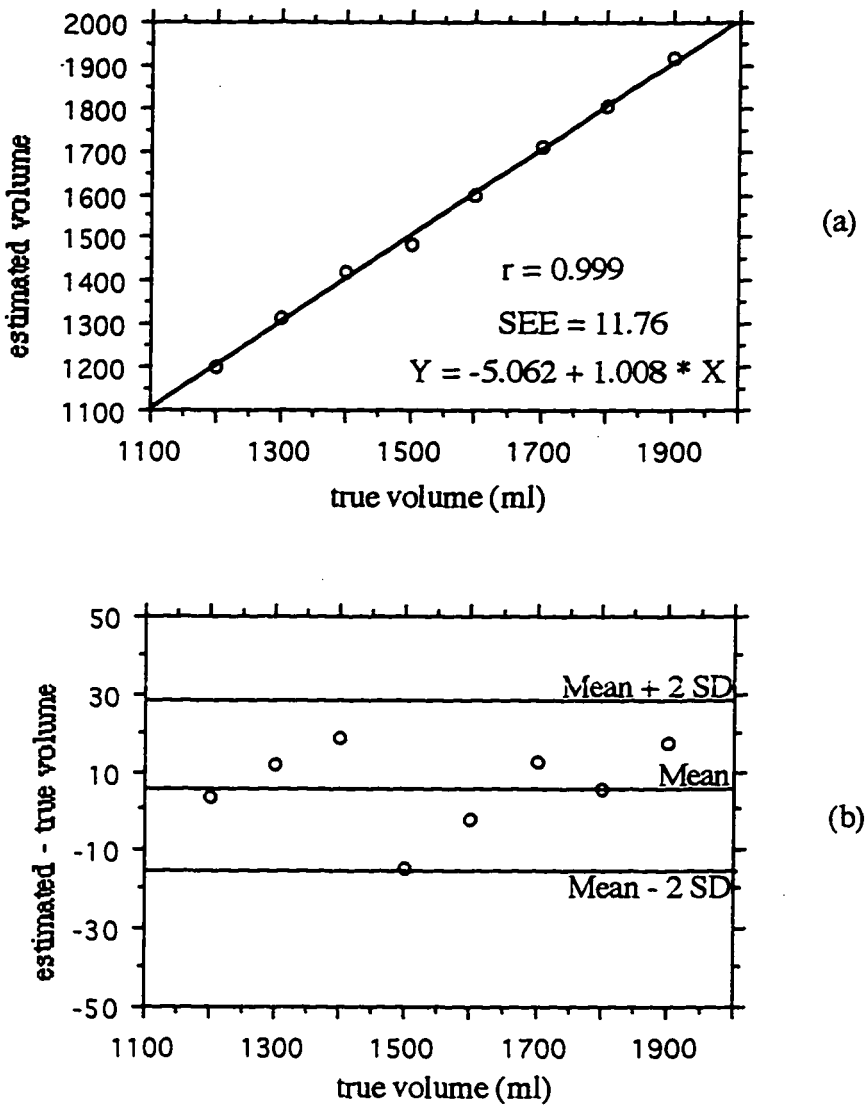

Figure 7.3 *In-vitro* validation of volume computation using a pig stomach. (a) linear regression plot of estimated volume against true volume (water displacement); (b) Bland-Altman plot of the difference between the estimated and true volume against the true volume.

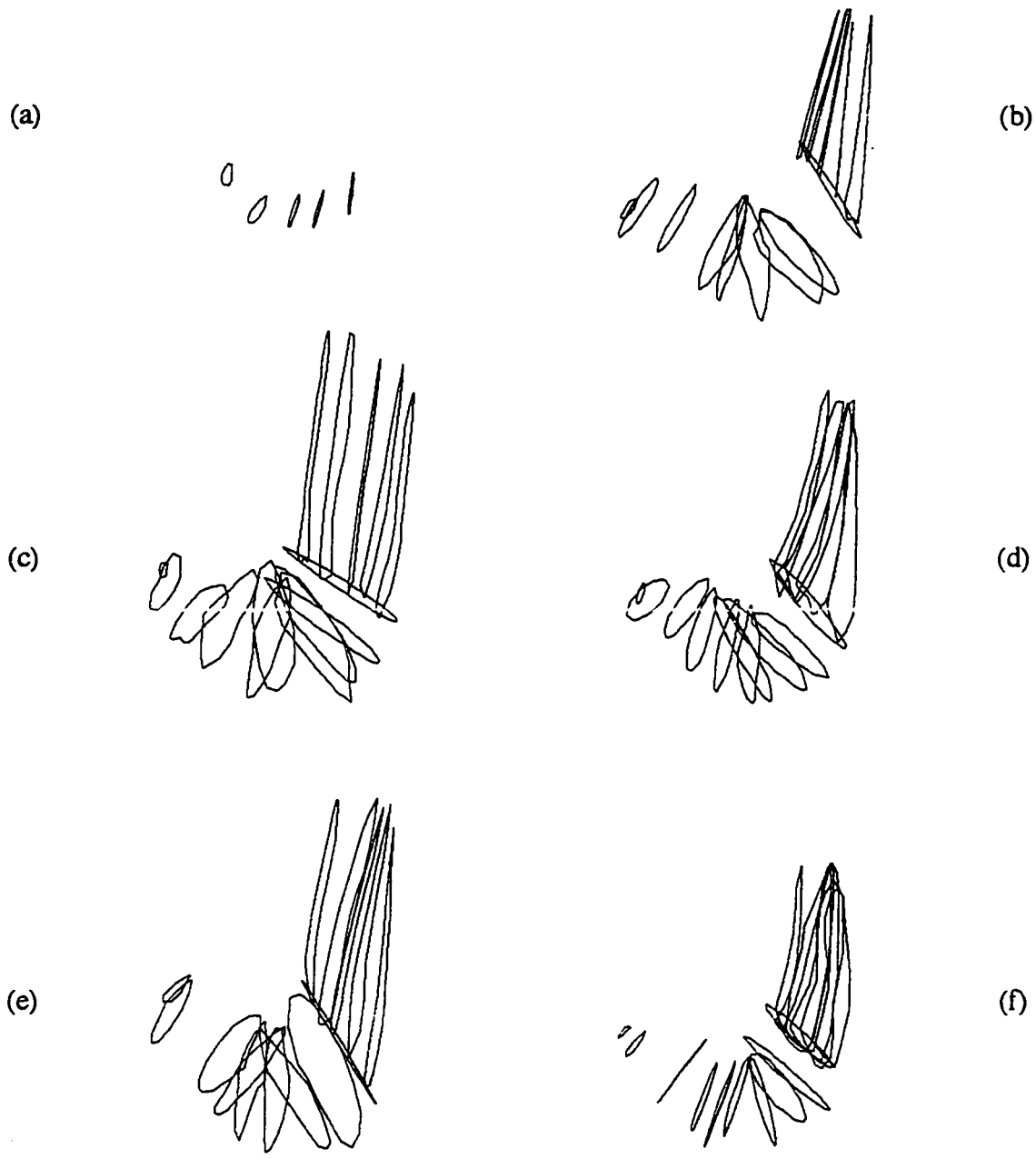

Figure 7.4 The contours of a healthy volunteer's stomach: (a) prior to broth ingestion, and (b) 5 min., (c) 10 min., (d) 15 min., (e) 20 min., and (f) 25 min. post-ingestion.

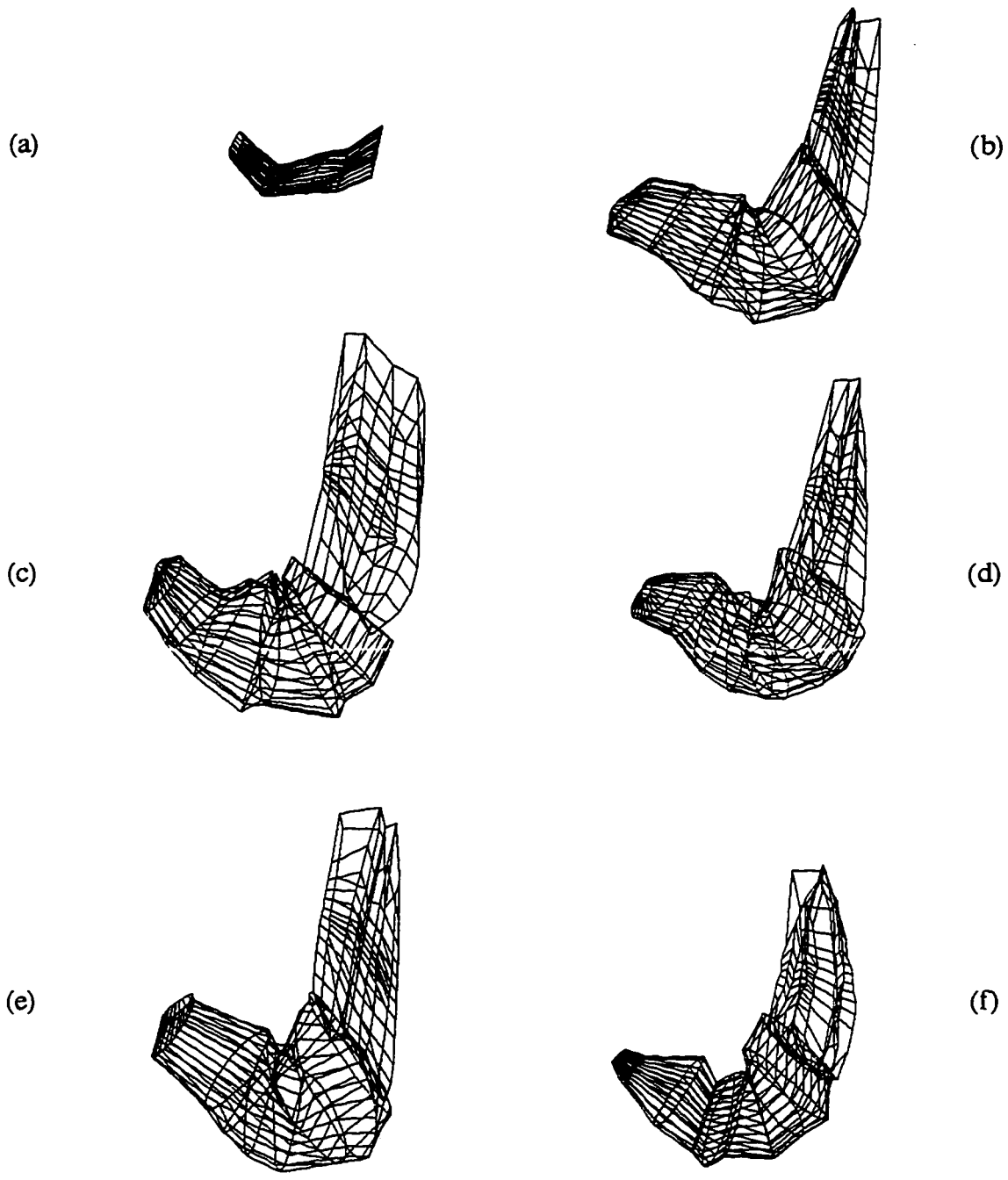

Figure 7.5 The wireframes of a healthy volunteer's stomach: (a) prior to broth ingestion, and (b) 5 min., (c) 10 min., (d) 15 min., (e) 20 min., and (f) 25 min. post-ingestion.

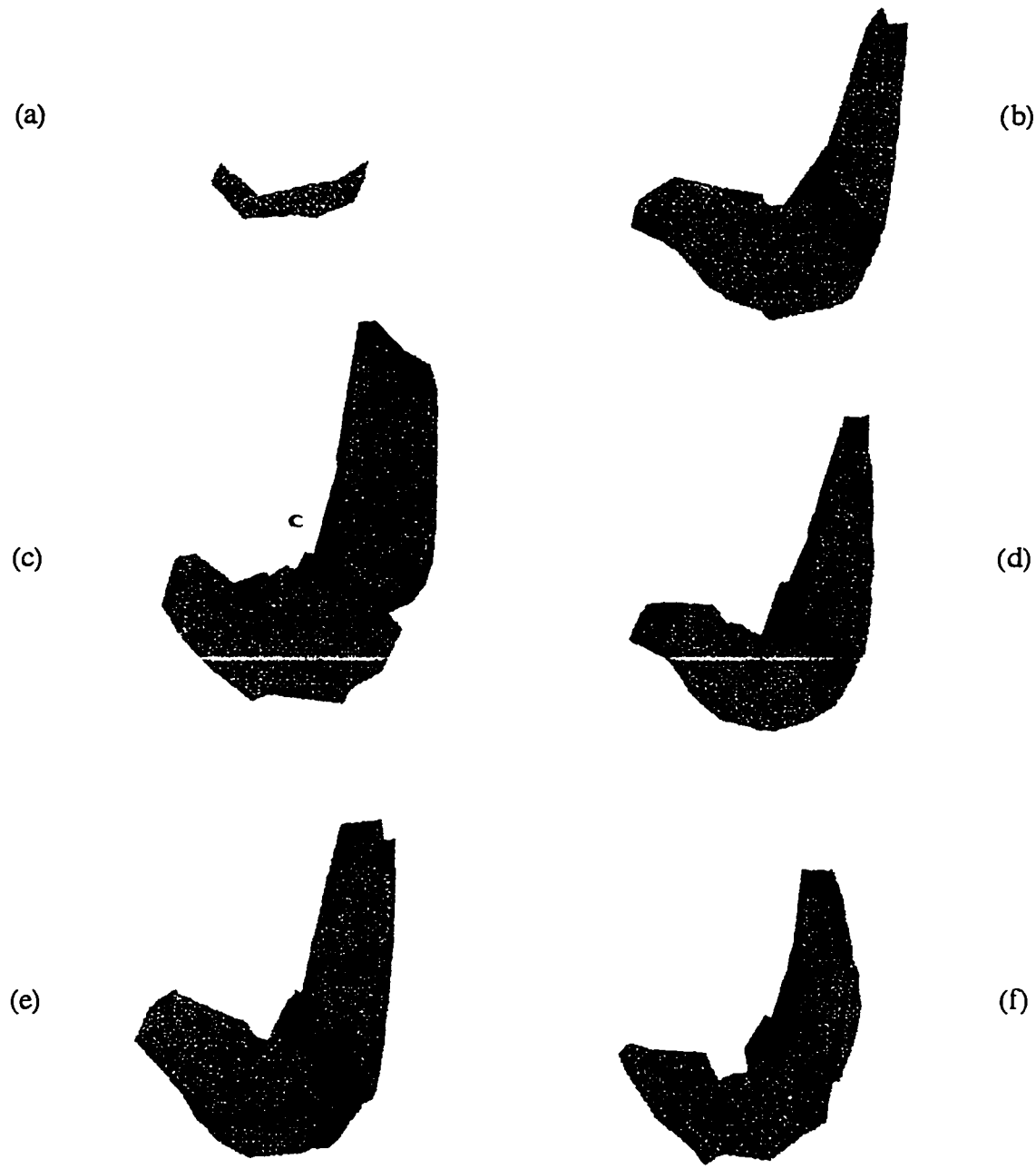

Figure 7.6 The surface rendering of a healthy volunteer's stomach: (a) prior to broth ingestion, and (b) 5 min., (c) 10 min., (d) 15 min., (e) 20 min., and (f) 25 min. post-ingestion.

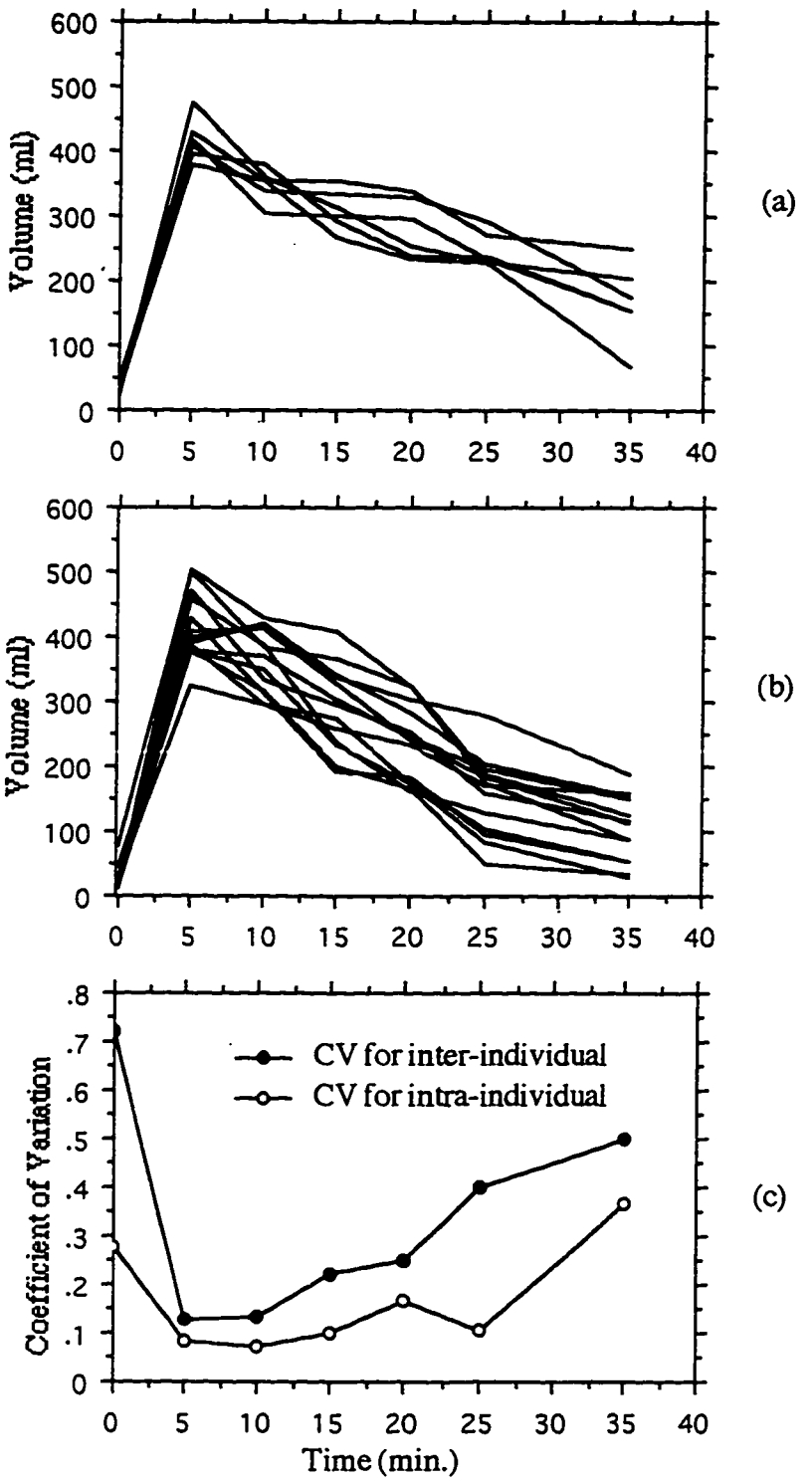

Figure 7.7 Gastric emptying for (a) one volunteer over 6 days (intra-individual), (b) 13 volunteers (inter-individual), and (c) the coefficients of variation for both intra- and inter-individual emptying.

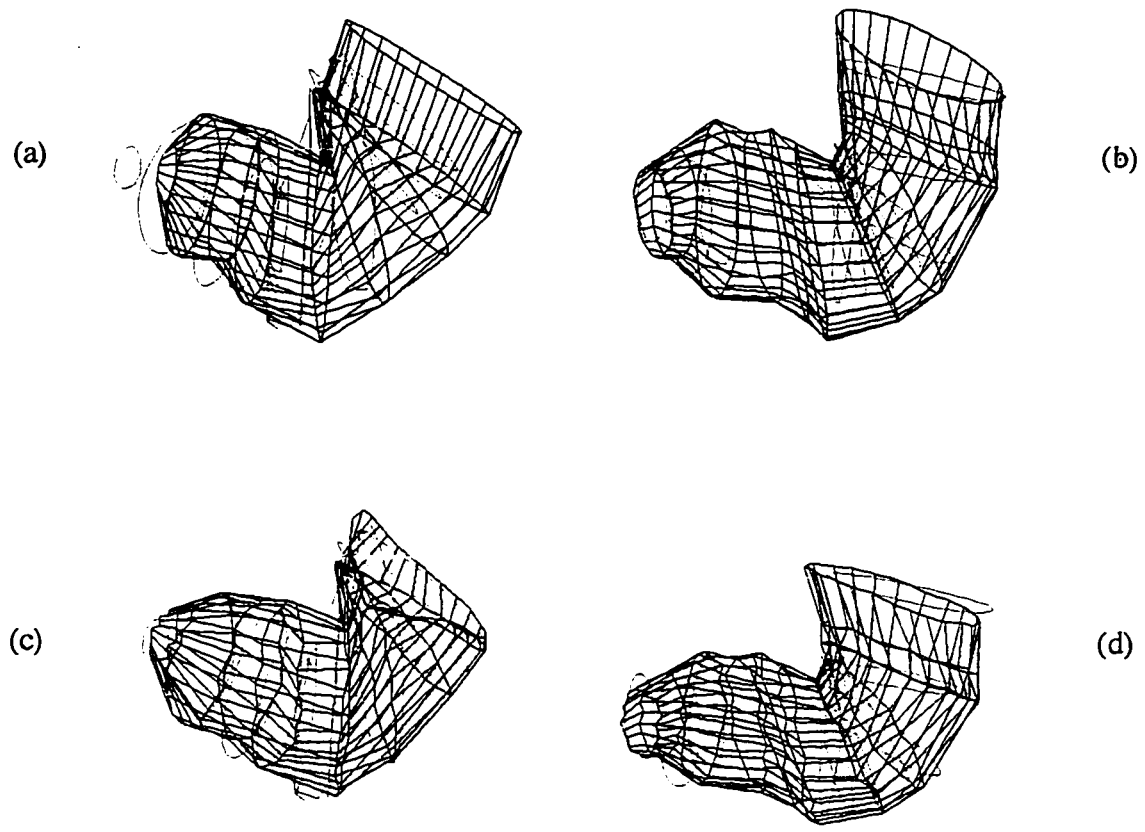

Figure 7.8 Wireframe reconstructions of the stomach with the deformation method described in Chapter 5. The template stomach (blue) is deformed to align with the target stomach (red). (a)(b) before deformation, (c)(d) after deformation. (a) and (c) is one stomach; and (b) and (d) is another stomach.

(a)

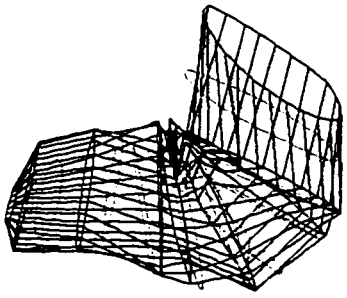

(b)

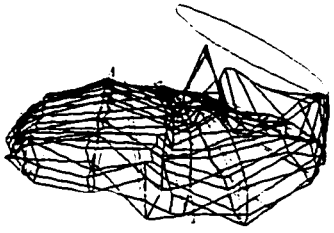

(c)

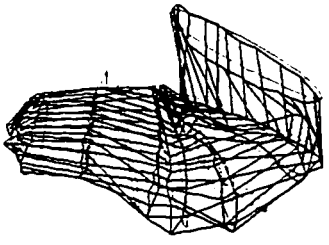

Figure 7.9 An example demonstrating the effect of regularization in the alignment between the template stomach (blue) and target stomach (red). (a) before deformation; (b) after deformation without regularization; (c) after deformation with regularization.

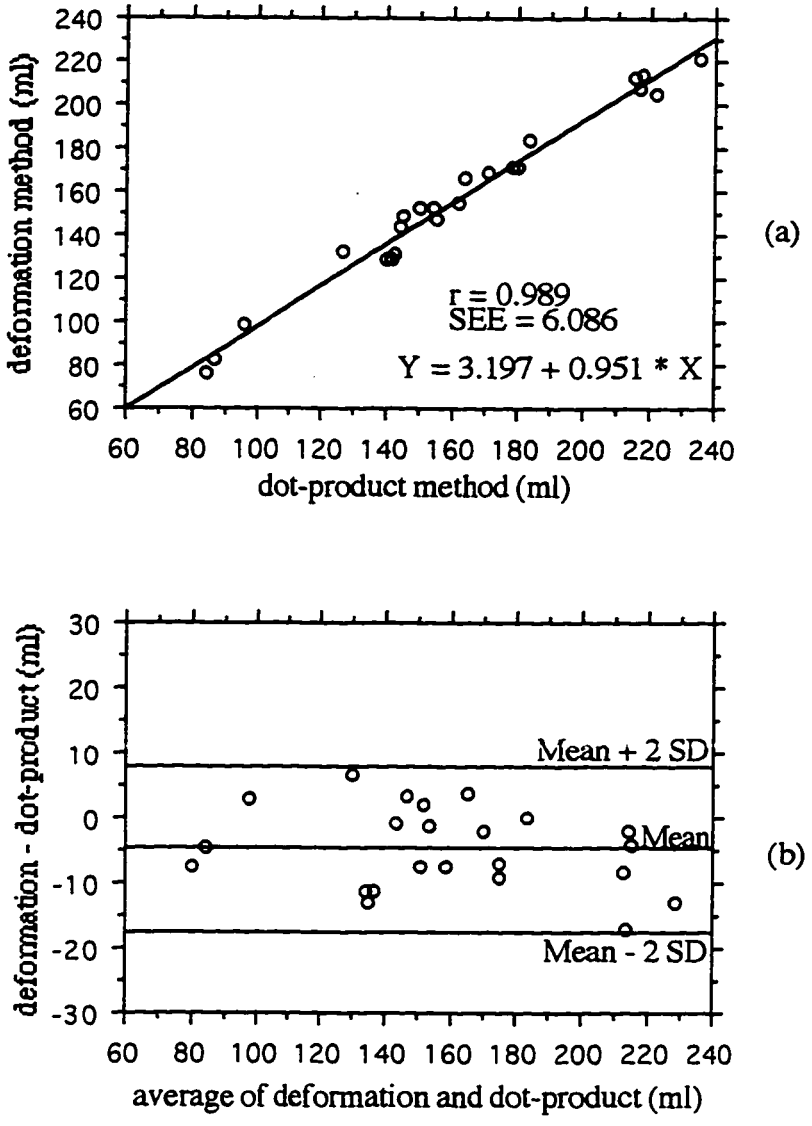

Figure 7.10 Plots showing the agreement between the deformation method and the dot-product method. (a) linear regression, and (b) Bland-Altman plot.

Chapter 8
Discussion and Conclusion

8.1 Gastric Emptying with Freehand 3D Ultrasound

The electromagnetic based 3D ultrasound system for acquisition of 3D data proved to be applicable for imaging the stomach. The conventional freehand scanning technique ensures good acoustic contact for each 2D image and the best suitable acoustic windows over the entire organ (in contrast to motor driven 3D ultrasound [28, 29]). Neither the scanhead sensor mount plus wiring nor the transmitter mount interfered with the normal scanning procedure. The problem of computing the stomach volume from intersecting contours has been solved with the two methods presented in this study.

I have demonstrated a non-invasive and radiation-free method which enables the calculation of gastric emptying rates of a broth meal in healthy subjects. Although the present 3D ultrasound system displayed high accuracy *in vitro*, we cannot immediately extrapolate these results to *in-vivo* conditions. Nevertheless, I believe that the results obtained *in vivo* are of acceptable accuracy. First, the mean intercept of the emptying curves of 13 healthy controls was 462.23 ml. Taking into account a mean fasting volume of 25.9 ml, a meal size of 500 ml, and some emptying of the meal during the consumption period [3], the intercept seems to be at a plausible level. Second, the broth in use was also utilized in a study where gastric emptying was monitored in healthy controls by radionuclide methods [99]. In that study, a mean half emptying time of 22.9 $\pm$ 12.1 min. was found using scintigraphy, which is extremely close to the value of 21.9 $\pm$ 4.5 min. found in this study. It is well known from scintigraphic studies that gastric emptying data can display substantial variability, both intra- and inter-individually. Compared to previous radionuclide methodological studies, the variability of the ultrasonic measurements found in our study seems comparable [100, 101].

This study was subject to the same limitations of ultrasound scanning that are generally observed in other studies. The method is fairly operator dependent and may be influenced by the presence of air pockets within the fundus, which dramatically reduce image quality. This problem was addressed in previous studies using the same broth meal, both in healthy controls [20] and in patients with functional dyspepsia [102]. These studies demonstrated that air in the gastric fundus was not a critical factor for

ultrasonic imaging using this meal, and no subjects had to be excluded for this reason. Similarly, in the present study, gas pockets in the fundus did not impair visualization of the proximal stomach to such an extent that data could not be analyzed.

Compared with ordinary ultrasound equipment, this 3D system based on magnetic scanhead tracking is susceptible to metallic influence and to interference from ambient magnetic fields. Therefore, it is of major importance that the laboratory environment is evaluated carefully in order to avoid spatial distortion of the data. The distance from the ultrasound scanner to the sensor on the scanhead should preferably be a minimum of 60 cm, and the bed or chair must be made of material that does not influence magnetic fields. Despite our efforts to remove watches, belts, and coins from both the operators and the participants, two of the data sets were distorted, probably due to magnetic interference from nearby experiments in the laboratory.

Our data analysis system was separated from the data acquisition system, and the stomach boundary outlining and volume computation were done after the examination. In the future, we plan to integrate both analysis and acquisition systems into a single platform in order to gain timely feedback of the acquired data. This will allow us to check the integrity of the data during the examination and identify possible sources of interference from metallic influence and ambient magnetic fields.

An acquisition time of two minutes was used for scanning the entire stomach in this study because the image workstation's design required that it stored each captured image to hard disk before the next acquisition. By utilizing image acquisition systems that enable storing of data in Random Access Memory (RAM) during scanning, the acquisition of a total gastric volume could easily be reduced to less than 30 seconds. The long scanning time experienced in this study may have caused a small intragastric volume to empty through the pylorus or possibly to change compartments during the scanning procedure. Conversely, the slow pace of data capture gave the operator time to carefully select images of high quality and to avoid capturing gastric contractions in the data set, thus minimizing potential errors in volume calculation.

In this study, the outlining of the stomach boundary was aided by a 3D view of all previously outlined contours which provided a real-time updated overview for improving the outlining consistency between images and avoiding overlap between the

proximal and distal compartments of the stomach. All outlining was performed manually, which was tedious and time-consuming. It may be worthwhile to explore an automatic or semi-automatic boundary detection method, such as a radial matched filter [103] or active contour model [72]. Most of the cross-sections of the distal stomach have shapes similar to an ellipse, so that ellipse fitting [104] of the automatically detected boundary points could be used to guide the boundary detection algorithms.

8.2 Volume Computation Methods

The major problem with freehand 3D ultrasound is the complex spatial relationship between images. Despite our effort to acquire nearly parallel cross-sections of the stomach, the contours still often intersected one another. Both volume computation methods developed in this study demonstrated the ability to reconstruct the wireframe from the intersected contours and compute the stomach volume with high accuracy.

The mean absolute error (0.7%) for the dot-product sorting method tested on the *in-vitro* pig stomach was considerably lower than the mean absolute error (5%) for the longitudinal sectioning method tested on *in-vitro* hearts reported by Moritz, McCabe, and Martin, et al. [34, 60, 61] (reviewed in Section 3.1). Our higher accuracy may result mainly from the improvement of the central axis formation, although the larger sized organ and different wall structure may influence the results. The central axis is the center for the interpolation for all contours. A contour will be misinterpolated if the axis is not inside the contour. In their method, a linear axis was formed by fitting all points with linear least squares, which is prone to error [60]. Thus, a tilt of the axis is very likely to result in misinterpolation, especially on the contours near both ends of the organ. In my dot-product sorting method, the protocol of stepwise scanning was utilized, and the central axis was replaced with a piecewise line called a central wire which was formed by properly linking the centroids of all contours. This eliminated the possibility of misinterpolation for each contour. Besides the improvement of the central axis formation, the stability of the innovative dot-product sorting algorithm also contributed to the high accuracy.

The default parameter value ($\alpha = 0.001$) for the deformation method usually worked well (80% of the cases in this study). The concept of using regularization to control the

stiffness of the deformation is easily appreciated after some training. When the default parameter value is not desirable, a reasonable alignment can usually be achieved with one or two additional trials. There are generally about 12 contours in the distal stomach, and 4x4x4 control points provided enough flexibility for the deformation in this study. Occasionally, when there are more contours in a particular scanning protocol, a higher density of control points, such as 5x5x5, may result in better alignment by providing more flexibility for the deformation. However, it takes longer for the alignment when using a higher density of control points (3 sec/iteration for 4x4x4 versus 25 sec/iteration for 5x5x5). About 80% of the computation time is spent on solving the $3M$ linear equations with $3M$ unknowns in equation (5.18), where M is the number of the FFD control points. My current research focused on the feasibility of the method as opposed to the efficiency of the algorithm. In the future, the deformation method could be accelerated by using a faster computer, using other more efficient linear equation solvers [94, 96], or optimizing the program at the assembly language level.

One prerequisite for the deformation method is that the template stomach must be reasonably close in shape to the target stomach, because the initial guess for the least square minimization needs to be reasonably close to the true minimum (global minimum). If the template stomach is too different from the target stomach, the alignment may fail, i.e. the solution of the least square minimization will get trapped in an undesired local minimum. Currently, I pre-build a template stomach (usually, the 5-min. stomach) for each individual due to the large inter-individual variation in stomach shapes. In the future, it may be possible to statistically classify the shapes of the stomach (such as fishhook, steer horn, and elongated stomach [8]), and set up a standard template stomach for each class.

The gastric emptying is a typical application which keeps track of an organ's volume change with time. Many other medical applications also share this attribute. For example, the volume change of the heart ventricles between diastole and systole gives the cardiac output. Another example is following potential kidney shrinkage in follow-up examinations after renal vascular surgery or transplant. Both the dot-product method and deformation method are also applicable to general volume computation problems in other applications involving freehand 3D ultrasound. The deformation method is actually a volumetric warping, so it also yields auxiliary information about the motion of

the 3D space surrounding the template surface. This suggests that not only can the deformation method be used to align wireframes and contours, but can also be used to align 3D medical images between different modalities, such as X-ray CT, MRI, PET, 3D ultrasound, or even histology tissue samples. Every imaging modality has a different resolution and undergoes different spatial distortions in the image formation process. The inter-modality alignment performed on certain easily identifiable landmark structures could be used to estimate the alignment for the complete 3D image data set.

The stomach volumes of healthy volunteers computed by the dot-product method and the deformation method are well correlated ($r = 0.989$). The two methods are based on different principles: the dot-product method requires that the surface in the lengthwise direction should approximately follow the direction of the central wire, while the deformation method relies on the resemblance between the template stomach and the target stomach. The dot-product method may not work well with some diseased stomachs, which have more concavities and exhibit irregular shapes [8]. The deformation method may be a good backup method in these instances. Although the deformation method is less accurate than the dot-product sorting method in computing the volumes of normal stomachs, it has the potential for handling more complicated intersecting contours. Minor interactive editing during the iterative deformation (energy minimization) process can avoid undesirable local minimums and improve the alignment. However, it is not straightforward to use current computer viewing/pointing devices to edit 3D objects. The deformation method is very likely to be the method of choice for volume computation with the advent of more convenient 3D viewing/pointing devices and faster computers.

References

[1] J. N. Hunt and W. R. Spurrell, "The pattern of emptying of the human stomach," *J Physiology*, vol. 113, pp. 157-169, 1951.

[2] J. N. Hunt and I. McDonald, "Influence of volume on gastric emptying," *J Physiology*, vol. 126, pp. 459-474, 1954.

[3] I. A. Donovan and L. K. Harding, "Gastric Emptying," in *Nuclear Gastroenterology*, P. J. A. Robinson, Ed.: Churchill Levingstone, 1986.

[4] L. P. Duan, Z. T. Zheng, and Y. N. Li, "A study of gastric emptying in non-ulcer dyspepsia using a new ultrasonographic method," *Scand J Gastoenterol*, vol. 28, pp. 355-360, 1993.

[5] D. L. Dumitrascu, S. Cotul, S. Tamas, and D. Dumitrascu, "Delayed gastric emptying in RX-negative dyspepsia," *Physiologie*, vol. 25, pp. 43-46, 1988.

[6] T. Yoshizato, T. Koyanagi, S. Nagata, T. Takashima, S. Fukushima, and H. Nakano, "Three-dimensional ultrasound image of the fetal stomach: congenital duodenal obstruction in utero," *Early Human Development*, vol. 41, pp. 39-47, 1995.

[7] J. W. Hole, Jr., *Human Anatomy and Physiology*, 6th ed: Wm. C. Brown Publishers, 1993.

[8] F. H. Netter, *Digestive System, Part I: Upper Digestive Tract*, vol. 3. Summit, N.J.: CIBA Pharmaceutical Company, 1959.

[9] O. H. Gilja, Personal Communication, 1995.

[10] J. D. George, "New clinical method for measuring the rate of gastric emptying: the double sampling test meal," *Gut*, vol. 9, 1968.

[11] N. W. Read, M. N. Al Janabi, T. E. Bates, and B. D. C., "Effect of Gastrointestinal intubation on the passage of a solid meal through the stomach and small intestine in humans," *Gastroenterology*, vol. 84, pp. 1568-1572, 1983.

[12] S. A. Muller Lissner and G. Schattenmann, "Effect of a transpyloric tube on gastric emptying and duodenogastric reflex in the dog," *Digestion*, vol. 28, pp. 176, 1983.

[13] D. E. Larson, *Mayo Clinic Family Health Book*: William Morrow and Company, Inc., 1990.

[14] G. H. Griffith, G. M. Owen, S. Kirkman, and R. Shields, "Measurement of Rate of Gastric Emptying Using Chromium-51," presented at The Lancet, 1966.

[15] D. N. Bateman and T. A. Whittingham, "Measurement of Gastric Emptying by Real-time Ultrasound," *Gut*, vol. 23, pp. 524-527, 1982.

[16] L. Bolondi, M. Bortolotti, and V. Santi, "Measurement of gastric emptying time by real-time ultrasonography," *Gastroenterology*, vol. 89, pp. 752, 1985.

[17] S. Holt, J. Cervantes, A. Wilkinson, and J. H. Wallace, "Measurement of Gastric Emptying Rate in Humans by Real-time Ultrasound," *Gastroenterology*, vol. 90, pp. 918-923, 1986.

[18] R. Ricci, I. Bontempo, E. Corazziari, A. La Bella, and A. Torsoli, "Real Time Ultrasonography of the Gastric Antrum," *Gut*, vol. 34, pp. 173-176, 1993.

[19] K. Hveem, T. Hausken, and A. Berstad, "Ultrasonographic Assessment of Fasting Liquid Content in the Human Stomach," *Scand. J. Gastroenterol*, vol. 29, pp. 786-789, 1994.

[20] O. H. Gilja, T. Hausken, S. Odegaard, and A. Berstad, "Monitoring postprandial size of the proximal stomach by ultrasonography," *J Ultrasond Med*, vol. 14, pp. 81-89, 1995.

[21] H. Chan, "Noninvasive bladder volume measurement," *J. Neurosci. Nurs.*, vol. 25, pp. 309, 1993.

[22] J. W. Wyatt, S. Meerbaum, M. L. Heng, P. Gueret, J. D. Hestenes, and E. Corday, "Cross-sectional Echocardiography III, Analysis of Asymmetric Left Ventricles," *Amer. Heart J.*, vol. 100, pp. 821-828, 1980.

[23] C. J. Griffiths, A. Murray, and P. D. Ramsden, "Accuracy and Repeatability of Bladder Volume Measurement Using Ultrasonic Imaging," *J. Urol.*, vol. 136, pp. 808-812, 1986.

[24] L. Jiang, M. D. Handschumacher, M. G. Hibberd, S. C. Siu, M. E. King, A. E. Weyman, and R. A. Levine, "Three-Dimensional Echocardiographic Reconstruction

of Right Ventricular Volume: In Vitro Comparison with Two-Dimensional Methods," *J. of American Society of Echocardiography*, vol. 7, pp. 150-156, 1994.

[25] P. M. Sapin, K. M. Schroder, A. S. Gopal, M. D. Smith, A. N. DeMaria, and D. L. King, "Comparison of Two- and Three-Dimensional Echocardiography with Cineventriculography for Measurement of Left Ventricular Volume in Patients," *J. of American College of Cardiology*, vol. 24, pp. 1054-1063, 1994.

[26] M. L. Nessly, G. Bashein, P. R. Detmer, M. M. Graham, R. Kao, and R. W. Martin, "Left ventricular ejection fraction: single-plane and multiplanar transesophageal echocardiography versus equilibrium gated-pool scintigraphy," *J. Cardiothoracic and Vascular Anesthesia*, vol. 5, pp. 40-45, 1991.

[27] M. Riccabona, T. R. Nelson, D. H. Pretorius, and T. E. Davidson, "In Vivo Three-Dimensional Sonographic Measurement of Organ Volume: Validation in the Urinary Bladder," *J. Ultrasound Med*, vol. 15, pp. 627-632, 1996.

[28] O. H. Gilja, N. Thune, and K. Natre, "In vitro evaluation of three-dimensional ultrasonography in volume estimation of abdominal organs," *Ultrasound in Med. & Biol.*, vol. 20, pp. 157-165, 1994.

[29] O. H. Gilja, T. Hausken, S. Odegaard, and A. Berstad, "Three-Dimensional Ultrasonography of the Gastric Antrum in Patients with Functional Dyspepsia," *Gastraenterology*, vol. 108, pp. A106, 1995.

[30] J. D. Foley, A. van Dam, S. K. Feiner, and J. F. Hughes, *Computer Graphics - Principles and Practice*: Addison-Wesley, 1991.

[31] T. T. Elvins, "A Survey of Algorithms for Volume Visualization," *Computer Graphics*, vol. 26, pp. 194-201, 1992.

[32] X. Li, J. Jong, R. Martin, P. Detmer, M. Legget, G. Bashein, D. Leotta, F. Sheehan, E. Bolson, and C. Otto, "Volumetric Reconstruction and Visualization in Three Dimensional Echocardiography: In Vitro Investigation," presented at IEEE International Ultrasonics Symposium, Seattle, WA, 1995.

[33] P. Lacroute and M. Levoy, "Fast Volume Rendering Using a Shear-Warp Factorization of the Viewing Transformation," presented at Computer Graphics Proceedings (SIGGRAPH 94), Orlando, FL, 1994.

[34] W. E. Moritz, A. S. Pearlman, and D. H. McCabe, "An ultrasonic technique for imaging the ventricle in three dimensions and calculating its volume," *IEEE Trans on Biomedical Eng*, vol. 30, pp. 482-491, 1983.

[35] D. A. Christensen, *Ultrasonic Bioinstrumentation.* New York: John Wiley & Sons, 1988.

[36] P. R. Detmer, "Automated endocardial border identification in ultrasound transesophageal echocardiograms using a matched filter," in *Bioengineering*. Seattle: University of Washington, 1990.

[37] L. E. Kinsler, A. R. Frey, A. B. Coppens, and J. V. Sanders, *Fundamentals of Acoustics*, 3 ed. New York: John Wiley & Sons, 1982.

[38] P. N. T. Wells, *Biomedical Ultrasonics*. New York: Academic Press, 1977.

[39] A. Macovski, *Medical Imaging Systems*. Engelwood Cliffs: Prentice Hall, 1983.

[40] P. N. T. Wells, "Medical Ultrasonics," in *IEEE Spectrum*, 1984, pp. 44-51.

[41] O. T. von Ramm, H. E. Pavy, and S. W. Smith, "High Speed Ultrasound Volumetric Imaging System Part 1: Transducer Design and Beam Steering," *IEEE Trans. Ultras., Ferro. and Freq. Control*, vol. UFFC-38, pp. 100-108, 1991.

[42] S. W. Smith, H. E. Pavy, and O. T. von Ramm, "High Speed Ultrasound Volumetric Imaging System Part 2: Parallel Processing and Display," *IEEE Trans. Ultras., Ferro. and Freq. Control*, vol. UFFC-38, pp. 109-115, 1991.

[43] H. A. McCann, K. Chandrasekaran, E. A. Hoffman, L. J. Sinak, T. M. Kinter, and J. F. Greenleaf, "A Method for Three-Dimensional Ultrasonic Imaging of the Heart In Vivo," *Dynamic Cardiovascular Imaging*, vol. 1, pp. 97-109, 1987.

[44] R. W. Martin, G. Bashein, R. Zimmer, and J. Sutherland, "An Endoscopic Micromanipulator for Multiplanar Transesophageal Imaging," *Ultrasound in Medicine and Biology*, vol. 12, pp. 965-975, 1986.

[45] A. Ghosh, N. Nanda, and G. Maurer, "Three-dimensional reconstruction of echocardiographic images using the rotation method," *Ultrasound in Med. & Biol.*, vol. 8, pp. 655-661, 1982.

[46] D. H. Pretorius, T. R. Nelson, and J. S. Jaffe, "3-Dimensional sonographic analysis based on color flow doppler and gray scale image data," *J Ultrasound Med*, vol. 11, pp. 225-232, 1992.

[47] E. A. Geiser, L. G. Christie, Jr., and D. A. Conetta, "A mechanical arm for spatial registration of two-dimensional echocardiographic sections," *Catheterization and Cardiovascular Diagnosis*, vol. 8, pp. 89-101, 1982.

[48] K. R. Stickels and L. S. Wann, "An Analysis of Three-Dimensional Reconstructive Echocardiography," *Ultrasound in Med. & Biol.*, vol. 10, pp. 575-580, 1984.

[49] D. L. Dekker, R. L. Piziali, and E. Dong, Jr., "A System for Ultrasonically Imaging the Human Heart in Three Dimensions," *Computers and Biomedical Research*, vol. 7, pp. 544-553, 1974.

[50] J. F. Brinkley, S. K. Muramatsu, W. D. McCallum, and R. L. Popp, "In vitro evaluation of an ultrasonic three-dimensional imaging and volume system," *Ultrason Imaging*, vol. 4, pp. 126-139, 1982.

[51] M. D. Handschumacher, J. P. Lethor, S. C. Siu, D. Mele, M. Rivera, M. H. Picard, A. E. Weyman, and R. A. Levine, "A New Integrated System for Three-Dimensional Echocardiographic Reconstruction: Development and Validation for Ventricular Volume with Application in Human Subjects," *J. American College of Cardiology*, vol. 21, pp. 743-753, 1993.

[52] A. S. Gopal, A. M. Keller, R. Rigling, D. L. King, Jr., and D. L. King, "Left Ventricular Volume and Endocardial Surface Area by Three-Dimensional Echocardiography: Comparison with Two-Dimensional Echocardiography and Nuclear

Magnetic Resonance Imaging in Normal Subjects," *J. American College of Cardiology*, vol. 22, pp. 258-270, 1993.

[53] T. C. Hodges, P. R. Detmer, D. H. Burns, K. W. Beach, and D. E. Strandness, Jr., "Ultrasonic three-dimensional reconstruction: in vitro and in vivo volume and area measurement," *Ultrasound Med Biol*, vol. 20, pp. 719-729, 1994.

[54] T. R. Nelson, D. H. Pretorius, and M. Sklansky, "Three-dimensional echocardiographic evaluation of fetal heart anatomy and function: acquisition, analysis, and display," *J Ultrasound Med*, vol. 15, pp. 1-9, 1996.

[55] W. E. Moritz, P. L. Shreve, and L. E. Mace, "Analysis of an ultrasonic spatial locating system," *IEEE Trans Instrum Meas*, vol. 25, pp. 43-50, 1976.

[56] P. R. Detmer, G. Bashein, and T. C. Hodges, "3D ultrasonic image feature localization based on magnetic scanhead tracking: in vitro calibration and validation," *Ultrasound Med Biol*, vol. 20, pp. 923-936, 1995.

[57] D. Leotta, P. Detmer, O. Gilja, J. Jong, R. Martin, J. Primozich, K. Beach, and D. Strandness, "Three-Dimensional Ultrasound Imaging Using Multiple Magnetic Tracking Systems and Miniature Magnetic Sensors," presented at IEEE International Ultrasonics Symposium, Seattle, WA, 1995.

[58] L. W. Johnson and R. D. Riess, *Numerical Analysis*, 2 ed: Addison-Wesley, 1982.

[59] J. P. Fisher, C. A. Wolfberg, J. S. Mikan, F. J. Keirnan, D. B. Fram, R. G. McKay, and L. D. Gillam, "Intracardiac Ultrasound Determination of Left Ventricular Volumes: In Vitro and In Vivo Validation," *J. of American College of Cardiology*, vol. 24, pp. 247-253, 1994.

[60] D. H. McCabe, "The determination of the volume of a closed surface described by nonparallel cross sections," in *Electrical Engineering Department*. Seattle: University of Washington, 1981.

[61] R. W. Martin, G. Bashein, P. R. Detmer, and W. E. Moritz, "Ventricular volume measurement from a multiplanar transesophageal ultrasonic imaging system: an in vitro study," *IEEE Trans on Biomedical Eng*, vol. 37, pp. 442-449, 1990.

[62] L. Bers, *Calculus*: Holt, Rinehart and Winston, Inc., 1969.

[63] R. N. Goldman, "Area of planar polygons and volume of polyhedra," in *Graphics Gems II*, J. Arvo, Ed.: AP Professional, 1991.

[64] L. W. Chang, C. H.W., and H. J.R., "Reconstruction of 3D medical images: a nonlinear interpolation technique for reconstruction of 3D medical images," *CVGIP: Graphical Models and Image Processing*, vol. 53, pp. 382-391, 1991.

[65] H. N. Christiansen and T. W. Sederberg, "Conversion of Complex Contour Line Definitions into Polygonal Element Mosaics," *Computer Graphics*, vol. 12, pp. 187-192, 1978.

[66] D. Meyers and S. Skinner, "Surfaces form contours," *ACM Trans on Graphics*, vol. 11, pp. 228-258, 1992.

[67] A. B. Ekoule, F. C. Peyrin, and C. L. Odet, "A triangulation algorithm from arbitrary shaped multiple planar contours," *ACM Trans on Graphics*, vol. 10, pp. 182-199, 1991.

[68] H. Akima, "A method of bivariate interpolation and smooth surface fitting for irregularly distributed data points," *ACM Trans on Math Software*, vol. 4, pp. 148-159, 1978.

[69] R. Szeliski, "Fast surface interpolation using hierarchical basis functions," *IEEE Trans on PAMI*, vol. 12, pp. 513-528, 1990.

[70] V. V. Savchenko, A. A. Pasko, O. G. Okunev, and T. L. Kunii, "Function representation of solids reconstructed from scattered surface points and contours," *Computer Graphics Forum*, vol. 14, pp. 181-188, 1995.

[71] A. Matheny and D. Goldgof, "The use of three- and four-dimensional surface harmonics for rigid and nonrigid shape recovery and representation," *IEEE Trans on PAMI*, vol. 17, pp. 967-981, 1995.

[72] M. Kass, A. Witkin, and D. Terzopoulos, "Snakes: active contour models," *International J of Computer Vision*, pp. 321-331, 1988.

[73] D. Terzopoulos and D. Metaxas, "Dynamic 3D models with local and golbal deformations: deformable superquadrics," *IEEE Trans on PAMI*, vol. 13, pp. 703-714, 1991.

[74] B. C. Vemuri and R. Malladi, "Constructing intrinsic parameters with active models for invariant surface reconstruction," *IEEE Trans on PAMI*, vol. 15, pp. 668-681, 1993.

[75] G. Coppini, R. Poli, and G. Valli, "Recovery of the 3-D Shape of the Left Ventricle from Echocardiographic Images," *IEEE Transactions on Medical Imaging*, vol. 14, pp. 301-317, 1995.

[76] T. DeRose, H. Hoppe, T. Duchamp, J. A. McDonald, and W. Stuetzle, "Fitting of surfaces to scattered data," presented at Curves and Surfaces in Computer Vision and Graphics III, 1992.

[77] W.-C. Huang and D. B. Goldgof, "Adaptive-Size Meshes for Rigid and Nonrigid Shape Analysis and Synthesis," *IEEE Transactions on Pattern Analysis and Machine Intelligence*, vol. 15, pp. 611-616, 1993.

[78] J. V. Miller, D. E. Breen, and W. E. Lorensen, "Geometrically deformed models: a method for extracting closed geometric medels from volume data," *Computer Graphics (SIGGRAPH '91)*, vol. 25, pp. 217-226, 1991.

[79] R. Szeliski and S. Lavallee, "Matching 3-D anatomical surfaces with non-rigid deformations using octree-splines," presented at IEEE Workshop on Biomedical Image Analysis, Seattle, 1994.

[80] J. Park, D. Metaxas, and L. Axel, "Volumetric Deformable Models with - Parameter Functions: A New Approach to the 3D Motion Analysis of the LV from MRI-SPAMM," presented at Fifth International Conference on Computer Vision, 1995.

[81] R. Sedgewick, *Algorithms in C++*: Addison-Wesley, 1992.

[82] G. Bashein and P. R. Detmer, "Centroid of a Polygon," in *Graphics Gems IV*, P. S. Heckbert, Ed.: Academic Press, 1994.

[83] A. V. Oppenheim and R. W. Schafer, *Digital Signal Processing*: Prentice Hall, 1975.

[84] R. M. Haralick, "Automatic Remote Sensor Image Processing," in *Topics in Applied Physics, Vol. 11: Digital Picture Analysis*, A. Rosenfeld, Ed.: Springer-Verlag, 1976, pp. 5-63.

[85] G. Wolberg, *Digital Image Warping*: IEEE Computer Society Press, 1990.

[86] K. A. Spector, "Registration of CT, MR, and Thallium SPECT Images of the Head Using the Principal Axes Transformation," in *Bioengineering*. Seattle: University of Washington, 1995, pp. 120.

[87] H. Jiang, R. A. Robb, and K. S. Holton, "A New Approach to 3-D Registration of Multimodality Medical Images by Surface Matching," *SPIE Visualization in Biomedical Computing*, vol. 1808, pp. 196-213, 1992.

[88] T. Schormann, A. Dabringhaus, and K. Zilles, "Statistics of Deformations in Histology and Application to Improved Alignment with MRI," *IEEE Transactions on Medical Imaging*, vol. 14, pp. 25-35, 1995.

[89] G. Gamble, B. Beaumont, H. Smith, J. Zorn, G. Sanders, M. Merrilees, S. MacMahon, and N. Sharpe, "B-mode ultrasound images of the carotid artery wall: correlation of ultrasound with histological measurement," *Atherosclerosis*, vol. 102, pp. 163-173, 1993.

[90] J. T. Salonen and R. Salonen, "Ultrasound B-Mode Imaging in Observational Studies of Atherosclerotic Progression," *Circulation*, vol. 87(suppl II), pp. II56-65, 1993.

[91] D. A. Healy, A. W. Clowes, R. R. Zierler, S. C. Nicholls, R. Bergelin, J. F. Primozich, and D. E. Strandness, Jr., "Immediate and long-term results of carotid endarterectomy," *Stroke*, vol. 20, pp. 1138-1142, 1989.

[92] T. W. Sederberg and S. R. Parry, "Free-form deformation of solid geometric models," *Computer Graphics (SIGGRAPH '86)*, vol. 20, pp. 151-160, 1986.

[93] A. N. Tikhonov and V. Y. Arsenin, *Solutions of Ill-Posed Problems*. Washington, DC: Winston, 1977.

[94] W. H. Press, S. A. Teukolsky, W. T. Vetterling, and B. P. Flannery, *Numerical Recipes in C*, 2nd ed: Cambridge University Press, 1992.

[95] R. Fletcher, *Practical Methods of Optimization*, 2nd ed. New York: John Wiley & Sons, 1987.

[96] G. W. Stewart, *Introduction to Matrix Computation*. New York: Academic Press, 1973.

[97] D. F. Leotta, P. R. Detmer, and R. W. Martin, "Performance of a miniature magnetic position sensor for three-dimensional ultrasound imaging," *submitted to Ultraound in Medicine and Biology*, 1996.

[98] O. H. Gilja, P. R. Detmer, J. M. Jong, D. Leotta, X. N. Li, K. W. Beach, R. W. Martin, and D. E. Strandness, Jr., "Intragastric Distribution and Gastric Emptying Assessed by Three-Dimensional Ultrasonography," *submitted to Gastroenterology*, 1996.

[99] K. Hveem, K. Jones, B. E. Chatterton, and M. Horowitz, "Scintigraphic and ultrasonographic measurement of the antral area - relationship to appetite," *Gut*, vol. In press, 1996.

[100] C. M. Brophy, J. G. Moore, P. E. Christian, M. J. Egger, and A. T. Taylor, "Variability of gastric emptying measurements in man employing standardized radiolabeled meals," *Dig. Dis. Sci.*, vol. 31, pp. 799-806, 1986.

[101] O. Lawaetz and H. Dige Petersen, "Gastric emptying of liquid meals - A study in 88 normal persons," *Ann Chir Gynaecol*, vol. 78, pp. 267-76, 1989.

[102] O. H. Gilja, T. Hausken, I. Wilhelmsen, and A. Berstad, "Impaired accommodation of the proximal stomach to a soup meal in functional dyspepsia," *Dig. Dis. Sci.*, vol. In press, 1996.

[103] P. R. Detmer, G. Bashein, and R. W. Martin, "Matched filter identification of left-ventricular endocardial borders in transesophageal echocardiograms," *IEEE Trans. on Medical Imaging*, vol. 9, pp. 396-404, 1990.

[104] R. M. Haralick and L. G. Shapiro, *Computer and Robot Vision*. Reading, MA: Addison-Wesley, 1992.

VITA

Jing-Ming Jong was born in Taipei, Taiwan. He was awarded a B.S. degree in Control Engineering from Chiao-Tung University, Hsinchu, Taiwan, in 1983. He earned a M.S. degree in Electrical Engineering from Utah State University, Logan, Utah, in 1989. He completed the Ph.D. degree in Electrical Engineering, for which this dissertation was written, at the University of Washington, Seattle, Washington, in 1997.

From 1983 to 1985, he served two years of military service as a second lieutenant communication officer in Integrated Communications and Command, Ministry of Defense, Taiwan. From 1985 to 1987, he worked at Sinotek Corp., Taipei, Taiwan, as a hardware and firmware engineer. From 1990 to 1993, he was a teaching/research assistant in Electrical Engineering Department, University of Washington. From 1994 to 1997, he was a research assistant/engineer in Surgery Department, University of Washington. His research interests include computer architecture and parallel processing, image processing and computer graphics, and medical 3D ultrasound.